Drone-Assisted Wireless Communications

Ali Mohammad Ali Hayajneh

Submitted in accordance with the requirements for the degree of

Doctor of Philosophy

School of Electronic and Electrical Engineering

University of Leeds

(May 2019)

Declaration

The candidate confirms that the work submitted is his own, except where work which has formed part of jointly authored publications has been included. The contribution of the candidate and the other authors to this work has been explicitly indicated below. The candidate confirms that the work submitted is his own and that appropriate credit has been given within the thesis where reference has been made to the work of others.

The work in Chapter 3 has appeared in the following publication.

1. Hayajneh, A.M., Zaidi, S.A.R., McLernon, D.C. and Ghogho, M., 2016, December. Optimal dimensioning and performance analysis of drone-based wireless communications. In Globecom Workshops (GC Wkshps), 2016 IEEE (pp. 1-6).

The work in Chapter 4 has appeared in the following publication.

2. Hayajneh, A.M., Zaidi, S.A.R., McLernon, D.C. and Ghogho, M., 2016, June. Drone empowered small cellular disaster recovery networks for resilient smart cities. In Sensing, Communication and Networking (SECON Workshops), 2016 IEEE International Conference on (pp. 1-6).

The work in Chapter 5 has appeared in the following publication.

3. A. M. Hayajneh, S. A. R. Zaidi, D. C. McLernon and M. Ghogho, "Performance analysis of UAV enabled disaster recovery network: A stochastic geometric framework based on matern cluster processes," IET 3rd International Conference on Intelligent Signal Processing (ISP 2017), London, 2017, pp. 1-6.

4. A. M. Hayajneh, S. A. R. Zaidi, D. C. McLernon, M. Di Renzo and M. Ghogho, "Performance Analysis of UAV Enabled Disaster Recovery Networks: A Stochastic Geometric Framework Based on Cluster Processes," in IEEE Access, vol. 6, pp. 26215-26230, 2018.

The work in Chapter 6 has appeared in the following publication.

5. A. M. Hayajneh, S. A. R. Zaidi, D. C. Mclernon, M. Z. Win, A. Imran and M. Ghogho, "Optimal Coverage and Rate in Downlink Cellular Networks: A SIR Meta-Distribution Based Approach," 2018 IEEE Global Communications Conference (GLOBECOM), Abu Dhabi, United Arab Emirates, 2018, pp. 1-7.

The work in Chapter 7 has been accepted for the following publication.

6. A. M. Hayajneh, S. A. R. Zaidi, M. Hafeez, D. C. Mclernon and M. Z. Win, "Coverage Analysis of Drone-Assisted Backscatter Communication for IoT Sensor Network", 1st International Workshop on Wireless sensors and Drones in Internet of Things (Wi-DroIT) 2019, Santorini Island, Greece.

This is to assert that the candidate has contributed solely to the technical part and writing of the papers (1)-(6) under the guidance of his co-authors.

To my parents, Mohammad Hayajneh & Noha Al-Omari.
To my lovely wife Razan Al-Wedyan.

ACKNOWLEDGEMENTS

First and foremost I would like to thank Allah Almighty whose benevolence and endless mercy made all my achievements possible.

I would like to express my deepest appreciation for all the support and technical guidance that I have received from Dr Des McLernon. Thank-you for all the knowledge you transferred to me and the confidence you put in me. Thank-you for your endless kindness, caring, time spent listening to me (even out of work) and for your smile that encouraged me always to give my best effort. I always go home full of energy, on the day after seeing you. I could not have imagined having a better friend, advisor and mentor for my PhD study.

My gratitude, appreciation and admiration go to Dr Syed Ali Zaidi for his support and guidance. Thank you for all the knowledge and constructive conversations that we went through. Thanks for your patience and welcome every day which encouraged me to widen my research from various perspectives.

Finally, thanks to Professor Mounir Ghogho for his support since before my arrival to Leeds. Thank-you for you kindness and high morality that guides me to be like you.

Thanks also to the Hashemite University for their financial support and funding without which, none of this work would have been possible.

My sincere appreciation goes: to my family who always encouraged and motivated me to reach this point in my life; to my father who taught me the alphabet; to my mother who made me a mathematician when she taught me to count to one hundred; to my wife for her support, care, constant reassurance and steadfast belief. Thank-you for your endless patience and companionship; to my brothers and sisters for their belief and support; to my family friends for the nights we spent laughing which lightened the pressure and stress of the endless research and study for this PhD.

Finally, I would like to thank all my former and present colleagues who made my time at Leeds university such a pleasure. They are too many to name individually, but they know who they are. Thank-you so much!

Abstract

In order to address the increased demand for any-time/any-where wireless connectivity, both academic and industrial researchers are actively engaged in the design of the fifth generation (5G) wireless communication networks. In contrast to the traditional bottom-up or horizontal design approaches, 5G wireless networks are being co-created with various stakeholders to address connectivity requirements across various verticals (i.e., employing a top-to-bottom approach). From a communication networks perspective, this requires obliviousness under various failures. In the context of cellular networks, base station (BS) failures can be caused either due to a natural or synthetic phenomenon. Natural phenomena such as earthquake or flooding can result in either destruction of communication hardware or disruption of energy supply to BSs. In such cases, there is a dire need for a mechanism through which capacity short-fall can be met in a rapid manner. Drone empowered small cellular networks, or so-called "flying cellular networks", present an attractive solution as they can be swiftly deployed for provisioning public safety (PS) networks.

While drone empowered self-organising networks (SONs) and drone small cell networks (DSCNs) have received some attention in the recent past, the design space of such networks has not been extensively traversed. So, the purpose of this thesis is to study the optimal deployment of drone empowered networks in different scenarios and for different applications (i.e., in cellular post-disaster scenarios and briefly in assisting backscatter internet of things (IoT)). To this end, we borrow the well-known tools from stochastic geometry to study the performance of multiple network deployments, as stochastic geometry provides a very powerful theoretical framework that accommodates network scalability and different spatial distributions. We will then investigate the design space of flying wireless networks and we will also explore the co-existence properties of an overlaid DSCN with the operational part of the existing networks. We define and study the design parameters such as optimal altitude and number of drone BSs, etc., as a function of destroyed BSs, propagation conditions, etc. Next, due to capacity and back-hauling limitations on drone small cells (DSCs), we assume that each coverage hole requires a multitude of DSCs to meet the shortfall coverage at a desired quality-of-service (QoS). Hence, we consider the clustered deployment of DSCs around the site of the destroyed BS. Accordingly, joint consideration of partially operating BSs and deployed DSCs yields a unique topology for such PS networks. Hence, we propose a clustering mechanism that extends the traditional Matérn and Thomas cluster processes to a more general case where cluster size is dependent upon the size of the coverage hole. As a result, it is demonstrated that by intelligently selecting operational network parameters such as drone

altitude, density, number, transmit power and the spatial distribution of the deployment, ground user coverage can be significantly enhanced.

As another contribution of this thesis, we also present a detailed analysis of the coverage and spectral efficiency of a downlink cellular network. Rather than relying on the first-order statistics of received signal-to-interference-ratio (SIR) such as coverage probability, we focus on characterizing its meta-distribution. As a result, our new design framework reveals that the traditional results which advocate lowering of BS heights or even optimal selection of BS height do not yield consistent service experience across users. Finally, for drone-assisted IoT sensor networks, we develop a comprehensive framework to characterize the performance of a drone-assisted backscatter communication-based IoT sensor network. A statistical framework is developed to quantify the coverage probability that explicitly accommodates a dyadic backscatter channel which experiences deeper fades than that of the one-way Rayleigh channel. We practically implement the proposed system using software defined radio (SDR) and a custom-designed sensor node (SN) tag. The measurements of parameters such as noise figure, tag reflection coefficient etc., are used to parametrize the developed framework.

Contents

List of Figures

List of Tables

Notations

A_{dB}, B_{dB}	Antenna gain
$\Gamma(z)$	gamma function
Φ	Point process
$\Phi(\mathcal{B})$	The counting measure of a point process
$\mathbb{1}(.)$	Bernoulli random variable
λ	The density of a point process
$\Lambda(.)$	The intensity measure of a point process
$\mathbb{R}^2$	Real numbers in the two dimensional space
$\mathcal{B} \in \mathbb{R}^2$	Closed Borel subset
$\mathcal{B}(0, R)$	Closed Borel set of radius R
$\mathbb{R}$	Set of real numbers
$\mathbb{E}_X[g(X)]$	The expectation of a function $g(X)$ of a random variable X
$\mathbf{x}$	Small bold-faced letter defines a vector
$\|\mathbf{x}\|$	Euclidean norm of $\mathbf{x}$
$\mathbf{x_i} \in \mathbf{\Phi}$	The position of the i-th point belonging to Φ
$\mathbf{x_0}$	The origin in $\mathbb{R}^2$
$\text{Exp}(1/\mu)$	Represents an exponential random variable with mean μ
β	The SIR/SNR threshold
α	The path loss exponent
$L(x)$	Path loss function
N_c	Number of channels in the network
N_s	Number of sensors
$\Pr\{X\}$	Probability of the even X
$\zeta_{LoS}, \zeta_{NLoS}$	Excess path-loss
f_{MHz}	Carrier frequency
ϕ_{mb}	Antenna beam width
W	Channel bandwidth
σ_T	Thomas cluster variance

σ_M	Matérn cluster radius
$\mathcal{L}_Z(s)$	Laplace transform (LT) of any random variable Z
$\setminus$	Exclusion of a subset from a superset
$x\|y$	Event x condition on event y
$f_X(x)$	The probability density function (PDF) for a random variable X
$F_X(x)$	The cumulative density function (CDF) for a random variable X
C_d	The generalized Lebesgue measure of the unit-ball
$\|.\|$	The Lebesgue measure
$v_d(\mathcal{B})$	The void probability of the process $\mathcal{B}$

Abbreviations

3G	Third generation
3GPP	3rd Generation Partnership Project
4G	Fourth generation
5G	Fifth generation
A2G	Air-to-ground
ABER	Average bit error rate
ABG	Alpha beta gamma
AeNB	Aerial e-nodeb
AP	Access point
ASE	Area spectral efficiency
ASK	Amplitude shift keying
AWGN	Additive white Gaussian noise
BER	Bit error rate
BPP	Binomial point process
BS	Base station
BSC	Base station controller
C2A	Cellular-to-air
CAGR	Compound annual growth rate
CAPEX	Capital expenditure
CCDF	Complementary cumulative density function
CDF	Cumulative density function
D2D	Device to device
DBS	Drone base station
DDN	Drone distributed network
DFR	Drone flying reader
DMF	Drone management framework
DMU	Drone mobile user
DSCNs	Drone small cell networks
DSCs	Drone small cells
EE	Energy efficiency

FSO	Free space optics
G2A	Ground-to-air
GPSK	Quadrature phase shift keying
HAP	High altitude platform
HBS	Helikite base station
HPPP	Homogenous Poisson point process
IHPPP	Inhomogeneous Poisson point process
IoT	Internet of things
LAP	Low altitude platform
LoS	Line of sight
LT	Laplace transform
LTE	Long term evolution
M2M	Machine to machine
Mbps	Mega bit per second
MBS	Macro base station
MCP	Matern point process
MCU	Microcontroller unit
MMU	Micro mobile user
MPSK	M-ary Phase Shift Keying
MU	Mobile user
NDVI	Normalized differential vegetation index
NFV	Network functions virtualization
NLoS	Non line of sight
NPD	Purchase diary panel
OFDMA	Orthogonal frequency division multiple access
OPEX	Operational expenditure
PCP	Poisson point process
PDF	Probability density function
PGFL	Probability generating functional
PMR	Professional mobile radio
PP	Point process
PPP	Poisson point process
PS	Public safety

QoS	Quality of service
RF	Radio frequency
SCC	Spatial coverage capacity
SDN	Software defined network
SDR	Software defined radio
SIR	Signal to interference ratio
SN	Sensor node
SNR	Signal to noise ratio
SONs	Self-organizing networks
SRC	Spatial rate capacity
SWIPT	Simultaneous wireless power and information transfer
TCP	Thomas point process
TDMA	Time division multiple access
TETRA	Trans-European trunked radio
UAVs	Unmanned aerial vehicles
UMa	Urban macro
UMi	Urban micro
WSN	Wireless sensor node

Chapter 1

Introduction

Contents

In this chapter, the motivation, the background and the organisation behind this thesis are presented. We first present the development of wireless communication networks. Then, we show the importance, challenges and use of drones in the post-disaster recovery networks. Finally, we highlight the organization and contribution of this thesis.

1.1 Motivation

Over the last few years, we have witnessed a perpetual increase in traffic and high data-rates demand in cellular networks. This very high traffic comes as a result of the technological leap in ubiquitous devices' connectivity that goes back to the convergence of the hand-held, portable devices, and smartphones as fully sophisticated computers. This development in device capabilities and the data-hungry applications has resulted in approaching the capacity frontier of the networks. From voice, video calling, social networking, web browsing

to real-time sensing and real-time tracking, we all appear unable to live disconnected. With more than 550 million 5G subscriptions and 4.6 billion LTE subscriptions, by 2022, there will be 8.9 billion mobile subscriptions, 8 billion mobile broadband subscriptions and 6.1 billion unique mobile subscribers with almost 90% of smartphone subscriptions on 3G and 4G [1, 2]. According to EE telecommunication company predictions, there will be an average of 50 connected devices in every smart-home in the UK by 2023 [3]. One of the key enablers for smart cities and the internet of things (IoTs) is the resilient and high-speed outdoor connectivity. In fact, the cellular network is the primary source of the outdoor internet connectivity and has been witnessing tremendous breakthroughs.

In the context of cellular networks, we can notice the speed of development over the last 30 years starting from only the voice-call services in the first-generation (1G) to the nowadays promising gigabits/sec data comms expected in the coming fifth generation (5G) communication networks. Coupled with the change of applications and demands of the wireless network, the existing 4G cellular network will not be able to cope with the increasing demand on the mobile network. The high air latency, limited data rates of not more than 100 Mbps are all encouraging towards the development of a more high-speed and resilient network. Even with the advanced developments in LTE license assisted access (LTE/LAA) which is capable of achieving 500+ Mbit/s, this figure is not sufficient to cover the demand for increasing rate. As shown in Figure 1.1, a compound annual growth rate (CAGR) of around 45% is predicted with 95% of mobile data traffic coming from smartphones by 2023 [1]. In order to address the increased demand for any-time/any-where wireless connectivity, both academic and industrial researchers are actively engaged in the design of 5G wireless communication networks. They actu-

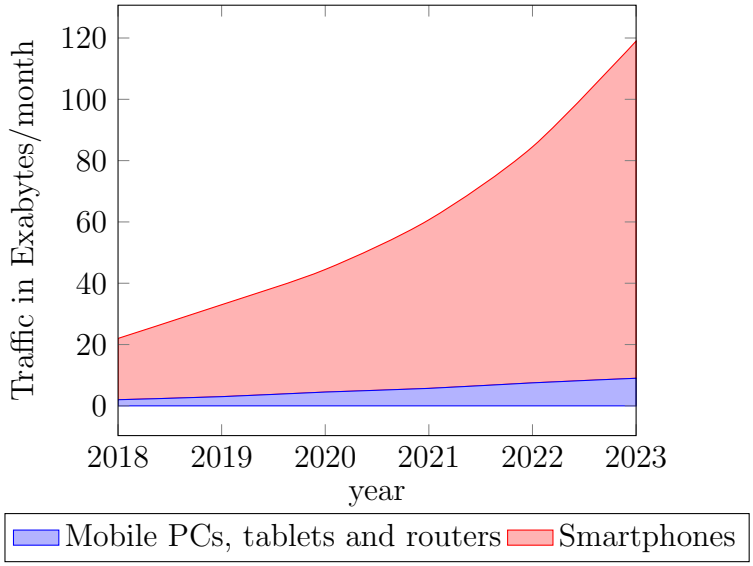

FIGURE 1.1: Mobile data traffic expectations [1].

ally aim for capabilities of 20 Gbit/s peak data rates, 500km/hr maximum speed for hand-off and QoS requirements, $10^6/km^2$ connection density [4]. In contrast to the traditional (i.e., bottom-up or horizontal) design, 5G wireless networks are being co-created with various stakeholders to address connectivity requirements across multiple verticals (i.e., employing a top-to-bottom approach). For better wireless channel utilisation, heterogeneous networks (HetNets) (i.e., networks with different sizes of cells and different tiers) have emerged as a promising solution to increase the area spectral efficiency by the densification of the network. The fundamental idea behind densification is to bring the network closer to the user by reducing the cell size while increasing the density of deployment. Most of these concepts, verticals and changes in the network design philosophy belong to the grand vision of smart connected cities empowered via ubiquitous on-demand connectivity.

While (as previously described) throughput gains harnessed through densification come at the cost of increased: (i) capital expenditure (CAPEX) with regards to network management and (ii) operational expenditure (OPEX)

with regards to dense deployment of small base stations (BSs). Consequently, for the scenarios where dynamic coverage is required in an on-demand fashion, fixed deployment is not an attractive option and this motivates the subject matter of this thesis.

Focusing on smart cities, one of the key features of smart connected cities is resilience by design. For example, smart cities should be able to provide enhanced public safety (PS) and early warning systems. From a communication networks perspective, this requires obliviousness under various failures. In the context of cellular networks, BSs failures can be caused either due to a natural or synthetic phenomenon. Natural phenomenon such as earthquake or flooding can result in either destruction of communication hardware or disruption of energy supply to BSs. Man-made destruction can be either due to a certain sub-system failure or alternatively due to vandalism. In such cases, there is a dire need for a mechanism through which capacity short-fall can be met in a rapid manner. While many disaster management protocols and technologies have been tested and used, time and resiliency are always the key assets to stagger. Drones, or the so called unmanned aerial vehicles (UAVs), have most of the agility and robustness properties and are more likely safe for humans as they can reach points that could be considered unsafe for a human to reach. Drones are emerging as a feasible technology for many scenarios in pre/post-disaster management, sensing and providing a temporary replacement for the destroyed cellular infrastructure.

According to recent figures from the retail research firm and national purchase diary panel (NPD) group, sales of drones have more than tripled over the last year. With the lower adaptation barrier, drone/UAVs[1] have attracted significant interest for various applications in the context of smart

[1]From now on, we use drone to describe drones and any type of UAVs.

city solutions. PS communication networks are one such application. Rapid on-demand deployment of drones furnished with cellular radio platforms is ideal for realizing disaster recovery networks, especially in both rural and urban areas. In cellular communication, drone empowered small cellular networks (DSCNs), or so-called "flying cellular networks" present an attractive solution for resilient smart cities and PS networks as they can be swiftly deployed for provisioning PS networks. The ability to self-organize either in stand-alone or via remote configuration in an on-demand manner makes the flying cellular network a key enabler for resilient communication networks. In this thesis, we will study and highlight the harness of drones in cellular communication networks. Our study will comprise the history of drone-based cellular networks (DCN), optimal dimensioning of the network geometry and some performance metrics to study the efficient utilization of such networks in terms of coverage and quality of service (QoS) metrics. We will also move into a higher-order statistical performance analysis of the traditional cellular network which is different from the traditional research literature.

1.2 Drone/UAV Assisted Communication Networks

As previously mentioned, swiftness in deployment for provisioning PS networks, the ability to self-organize, either in stand-alone or via remote configuration are all making the flying cellular network a promising key enabler for resilient communication networks. DSCNs present an attractive alternative and complementary deployment option. Since DSCNs are mostly operator deployed, both: (i) interoperability amongst DSCNs nodes; and (ii) compatibility with operational cellular infrastructure can be ensured. Moreover, propagation

conditions are much more favourable and can be further optimized by exploiting controlled mobility of drones [5–7]. Consequently, it is envisioned that both device to device (D2D) communication and DSCNs will complement the legacy private/professional mobile radio (PMR) (e.g., trans-European trunked radio (TETRA) and project 25 (P25)) for enabling next generation PS networks [8–10]. The aforementioned features and others receive attention and exploitation from standardization bodies such as 3rd Generation Partnership Project (3GPP) where applications such as PS and general emergency services are currently being explored. In addition, a practical use of drones for provisioning wireless connectivity has been implemented and tested using balloons in project LOON by Google (note that unmanned drones have also been used by Facebook to provide access to the internet). In the LOON project, Google has integrated 4G technologies into balloons travelling in the stratosphere (i.e., 18-50 km balloon altitude, twice as high as commercial plans) while Facebook provided WiFi access points at heights up to 30 km. Google also tested drone empowered millimetre-wave (mm-wave) small cells in a currently ongoing project Skybender. In all, drones as a kind of the general term "autonomous vehicles" are making a breakthrough in achieving the desired features for smart cities for PS communication network [6, 11–16].

Looking at the flying based assisted cellular networks, we realize that there are a lot of opportunities and challenges [14, 17]. However, by looking to flying BSs, we see potential features such as (but not limited to): (i) the resilient self-reconfiguration, (ii) low latency with high throughput, (iii) lower operational/capital expenditures OPEX/CAPEX if compared with densification solutions for the traditional cellular networks and (iv) the extra degrees of freedom with the top to bottom design. The study and orientation towards the utilization of drones in communications as a temporal recovery network has

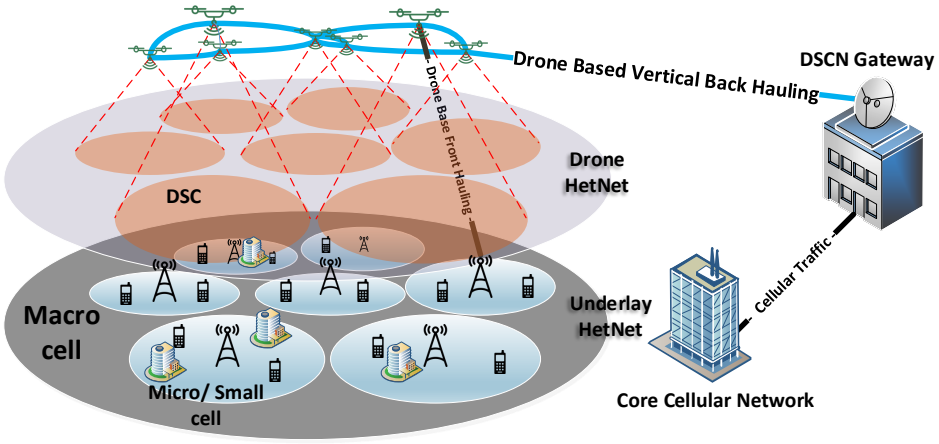

FIGURE 1.2: Grand vision of DSCNs with front/back-hauling for heterogeneous networks recovery.

thrived in many research papers. Hence, there are exaggerated expectations that the use of drones can achieve a breakthrough in various aspects particularly in PS networks [13–21]. Next, we introduce the possible opportunities alongside the related challenges in deployment of such networks.

1.2.1 Drone Opportunities, Design Challenges and Current Work Limitations

In this subsection, we present the potential opportunities, advantages and possible applications for drones in assisting general wireless communication systems. Also, we show the design challenges that are related to the utilization of drones in wireless communication.

Opportunities and Possible Applications

1. *Drones as flying cellular BSs and in public safety*: In post-disaster scenarios or some temporal public crowded venues, as shown in Figure 1.2, drones can be utilized to off-load the cellular data traffic and increase the delivered capacity and QoS. In the scenarios of post-disasters, such as earthquakes and floods, some network infrastructure could be damaged with no possible quick way to recover due to some geographical constraints and disconnection in the public transport networks. As the flying BS can move resiliently and very quickly, they can be used to deliver wireless and broadband communication to peoples and rescue services. Some of the research efforts focus on integrating the flying cells for PS communications in the frame of D2D communications. For example, the authors in [15] attempted to find an optimal location for the relaying drone in D2D communication by applying an efficient algorithm and seeking to maximize the data rate of the link. However, taking into account that the up-link and down-link propagation characteristics are different for drone communications, we expect that the design for drone recovery networks will be different than the traditional cellular network. In the same context, the authors in [11] provided a new framework for the use of drones in assisting the underlaid D2D where the geometry of the network consists of both down-link and D2D users, and the drone is employed to serve both types of the users. In their study, they found the optimal location and number of drones required to achieve the pre-defined outage threshold and capacity. In the context of temporal cellular assisting, drone flying BSs eliminate the need for a fixed expensive terrestrial infrastructure which leads to savings in the

OPEX/CAPEX.

The key feature of flying objects and the vertical design of such temporal networks is the desirable channel characteristics for the air to ground (A2G) link. Flying drones provide better line of sight (LoS) link characteristics, and thus the quality of the network can be enhanced by wireless front-hauling and back-hauling. However, increasing the LoS link probability can increase the co-channel interference between different locations of the network and hence an optimal localization and interference management for the drones on the sky is required [22]. In the next subsection, we present some of the challenges related to the global vision of drones cellular networks.

2. *Smart cities and IoT communications*: With the proliferation of smart connected, sensing devices and the massive IoT applications as key enablers of the future smart cities, there is a dire need for a more flexible platform to deliver IoT services and communication. IoT applications vary between plant dissemination, localisation, smart agriculture (see Figure 1.3)[2], advanced alarming systems and healthcare applications [23–25]. All of these applications, in essence, require an energy efficient, low latency and high data rate communication link [24]. These are all considered as challenges for IoT communication. Also, most of the IoT devices are battery limited. Hence, short distance communication with enhanced link characteristics (i.e., LoS communication link) is required. Accordingly, new ways of IoT communication needs to be deployed.

   In this context, drones can play an essential role in delivering the en-

[2]This will be the topic of chapter 7, where we will address the performance analysis of drone assisted IoT in the context of backscatter wireless communications.

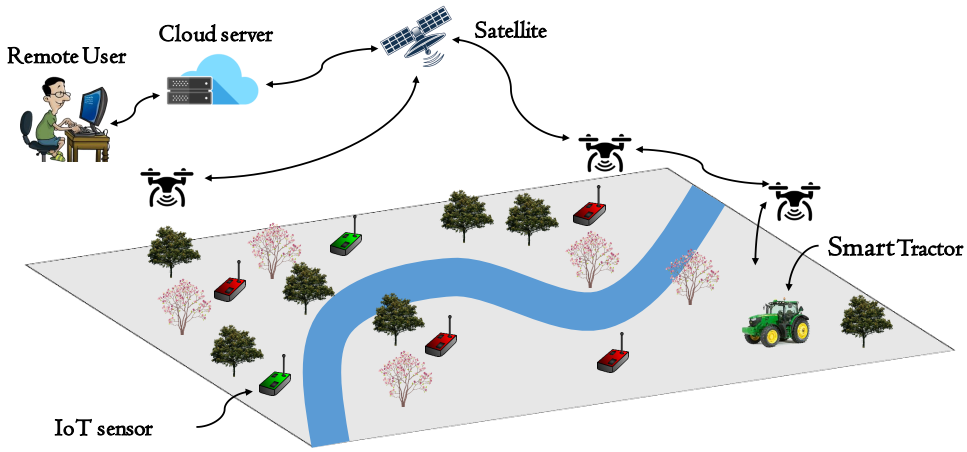

FIGURE 1.3: Drone-assisted smart IoT agriculture.

abling features of IoT. In some areas, such as rural areas, mountains, deserts and forests, where a traditional cellular or broadband network is weak or impossible to deliver with a limited IoT device batteries where a long distance communication link is a power-inefficient solution, drones can be deployed as flying internet platform to provide a temporary internet connection [26,27]. Due to the agile and flexible nature of drones, they can provide short distance and on-time communication which can save IoT devices batteries. Many of the IoT network features, such as chaotic deployment and dynamic changes in locations, require more resilient, dynamic management communication platforms. Here, drones can act as promising enablers for a self-organised network and as key enablers for smart cities. Obviously, drones can efficiently and dynamical be utilized to improve IoT communication. In this thesis, we will preform a statistical performance analysis for drone assisted backscatter communication for IoT sensor network. In this application, drones secure a proximity between the system components (i.e., sensor node tag and the drone gathering the nodes data) for optimal deployment and

coverage (see chapter 7 for details).

3. *Cell extending and front-hauling*: In the scenario where the only need is to off-load a single cell for an immediate area off-loading, drones can serve to relay all the communication requests to the nearest available cell. Here, the flying drone is only required to be deployed in an incremental adaptive cooperative fashion. That is, the relaying is taking place on an in demand fashion and depends on the status of the network and the overall metrics of performance. For example, the authors in [14] introduced a half-flying half-terrestrial helikite base station (HBS) in a way that an aerial e-nodeB (AeNB) is connected to the earth gateway via a fibre optic link (i.e., fibre front-hauling). However, this approach is only suitable for special event off-loading since the use of AeNB types of equipment is not guaranteed due to reachability issues. In extending the cell coverage, the authors in [13,28] exploited the drones to relay signals for broadband and LTE to extend the coverage and off-load traffic to the surrounding free cells via flying relays in an ad-hoc fashion. In this scenario, we need to guarantee that the surrounding cells are not fully-loaded or destructed in a post-disaster scenario. Drones can also contribute to scenarios of hot-spot venues such as football games and other applications to overcome the sudden capacity short-fall by deploying a temporal flying BS instead of a fixed cellular infrastructure. In cell extending, a terrible pain at the neighbour cells sharing the same channels are expected [22, 29]. That is, extending the cell coverage comes with the increase of co-channel interference and hence a degradation on the overall performance and throughput at the expense of the achieved capacity due to the overloading. In fact, this can be controlled and optimized by employing a sophisticated management framework to control

and manage the co-working network components [17]. Consequently, we recognise that we need a platform predicate, sophisticated network architecture and management controllers to attain the agility of smart cities.

Design challenges and current work limitations

Despite the obvious promising opportunities of drones in assisting wireless communications, researches in the field are still trying to define and overcome the embedded challenges from different perspectives. Next, we highlight some of these challenges and critical issues:

1. *Channel models*: To identify the system and link parameters for better network design, many papers conducted practical test-bed experiments to model the large-scale A2G and ground-to-air (G2A) path-loss models. The path-loss defines the amount of signal that is received from the associated transmitter and at the same time the amount of interference from the co-channel interferers. The first practical model was introduced in [30, 31]. In these papers, the authors provide early statistical models for A2G channels in an urban environment. They constrained the path-loss model to an A2G link (downlink) channel with elevation angles greater than 10 degrees. They present the path-loss models for the LoS and non-line of sight (NLoS) communication links for frequencies from 200 MHz to 2.4 GHz. However, their model does not cover all city models since they only introduced the model for urban environments. The importance of their research is that they show that the G2A and A2G are much more favourable to be utilized as relays for cell extending due to the better LoS characteristics of the links. Furthermore, the

authors in [32] presented a new path-loss model with the consideration of shadowing and presented a statistical model for the distribution of the LoS and NLoS probabilities. However, they considered only some types of urban environment and only for high altitude platforms (HAP). The authors in [33] influenced by [30–32] presented a semi-practical, semi-statistical model for the path-loss model. In their paper, they presented a model to cover many city types (i.e., dense urban, suburban and high-rise). In contrast to the previous studies, they did not take into account the effect of shadowing, but they introduced a statistical model with simple formulas[3].

Despite some attempts in the literature, there are not enough G2A path-loss models. In [34], the authors show a cellular-to-air (C2A) path-loss model. In their paper, the authors introduced a path-loss model for the link between a cellular BS and a flying BS in a way suitable for front-hauling or relaying scenarios. In [35], the authors try to provide a coverage performance analysis for the uplink channel. However, they only use a general power-law, path-loss model. This type of path-loss models is not sufficient to optimally design the uplink communication link for drone-assisted wireless communication systems since they do not incorporate the effect of the drone height into the analysis. In [36], the authors used the same path-loss model for A2G in [33] to model the communication link for the G2A link which may be considered not precise and may give a misleading performance analysis. Hence, a clear view of the large-scale path-loss model needs to be refined and revisited. From a performance analysis perspective, the available path-loss models in the literature give in most of the cases a non-tractable mathematical

[3]A more comprehensive literature review about path-loss modelling for UAV to ground channels can be found in [7].

analysis in terms of calculating the performance metrics and aggregating the effect of interference in communication networks. Throughout this thesis, we focus on the A2G downlink analysis of the drone cellular networks, and the G2A link analysis is out of the scope of the thesis.

2. *Optimal dimensioning, interference management and performance analysis*: In the context of the large-scale drone recovery networks management, many papers were conducted to build an efficient placement for the network flying BSs [19, 22, 37, 38]. First, the authors in [19], based on the results of [6], present a 3D optimization problem for drone small cells (DSCs) with the aim to maximize the number of users to be covered by such DSCs using a numerical search algorithm to satisfy the defined QoS measures. The paper focuses on drone empowered future cellular networks for post disaster recovery and PS. Nevertheless, the effect of cross network interference (i.e., interference between operational cellular infrastructure and DSCs in a post-disaster scenario) has not been addressed. Furthermore, the authors in [38] using a facility location problem, introduced a step parametrization for the scenario where many flying stations are in operation. The aim of their study is to maximize the power utilization by optimally defining the coverage area boundaries and the optimal location for the drones in the altitude and separation distance dimensions. In their paper, they only discussed the scenario of two operating drones and the optimization problem is only valid for this configuration.

   In fact, a generalization based on the random spatio-temporal distribution of the flying BSs and users is required. Also, a good generalization on the resulting distribution on the post-disaster scenario is needed to accurately model the entire system. In addition, the authors in [22]

discuss a more comprehensive scenario to build an interference management framework of the recovery networks. They studied the scenario in which a number of UAVs are deployed and a percentage of the macro base stations (MBSs) are destroyed. In the paper, they showed that the flying BS deployment can improve the throughput coverage in the post-disaster scenario and the 5th percentile spectral efficiency of the network. However, they did not find the optimal design parameters such as the optimal number of drones and the optimal altitude of the recovery network. Also, they did not take into account the interference between the co-channel drone base stations (DBSs).

Relying on the results of link budget and path-loss model, the DSCNs can be designed and optimized in the same way as in the heterogeneous networks (i.e., the same performance metrics with different dimensions and degrees of freedom)[4]. However, the differences are in the capabilities of the DBSs in terms of capacity and airtime, etc. To this end, many studies were conducted to measure the performance enhancement metrics and to identify the design and implementation of optimal conditions and elements of the operation. Here, researchers tried to find the optimal drone altitude which secures the maximum coverage for single and two small circular cells. For instance, the authors in [6,12,38] provided a solution for the optimization problem between two DSCs. The solution of the problem aims for considering the maximal overage and minimal interference between the serving DBSs. They provided an algorithm at which the cell boundaries and centre changes with the distribution of the users, which intuitively maximizes the coverage probability and

[4]Due to the similarity of large-scale performance analysis between flying networks and cellular networks, we will devote chapter 6 to introduce higher statical performance analysis of the traditional cellular network with the aim to increase fairness across all users in the context of meta distribution analysis.

minimizes the required transmit power from the DBSs. However, the authors did not investigate the effect of multi-path fading channels and did not address the effect of the directivity model of the antennas on the entire system performance. Hence, an investigation into consideration of multi-path fading, spatial distribution of DBSs, and the antenna gain patterns is required. Relying on the aforementioned drone-based recovery network literature and the lack of a comprehensive frameworks to define the network design aspects and parameters, we aim in this thesis to show a more comprehensive performance analysis frameworks based on stochastic geometry analysis. We will try to introduce a more comprehensive parametrization framework to predict the coverage performance of the deployed drone BSs in different network geometries.

3. *Trajectory optimization, energy efficiency and optimal placement:* Despite the favourable channel conditions and self-organizing capabilities that drones can provide, energy constraints of the drone batteries and path-planning for optimal utilization of power is still under study. Energy constraints affect the air time, placement of drones and also affect the throughput of the deployed of the drone wireless communication. In the energy efficiency context for cellular networks recovery, the authors in [39] studied the energy efficiency for constrained and unconstrained fixed-wing UAVs as a function of the UAV's flying speed, direction and acceleration and tried to minimize the consumed energy and maximize the total throughput for horizontal and circular moving drones communicating with ground users. In [40], the authors introduced a multi UAV enabled wireless communication system with the aim of maximizing the minimum throughput for ground users under a joint UAV's trajectory, power control, users association and scheduling. The authors in [41] ad-

dressed a communication system optimization problem to maximize the air time for a hovering drone serving as a cellular flying BS to minimize the drone hovering stop time to serve a ground mobile user (MU). The cell partitioning algorithm in [41] shows that significantly higher fairness among the ground cellular users can be achieved when compared to the traditional Voronoi tessellation.

In the context of path-planning, specifically for IoT applications, there is a dire need to maximize the air time of drones by minimizing the total path length that the drone has to travel. For example, the authors in [42, 43] implemented a drone communication system with high-level architecture for the design of a collaborative aerial system for monitoring, sensing and search capabilities. Similar work to [42, 43] is presented in [44]. The authors in [44] investigated the harness of a swarm of drones as a mobile data gathering platforms for ground distributed sensor nodes. They aim to maximize the total drone path duration (i.e., travel distance) with the collision, energy autonomy and good route fairness in mind. They formalized the optimization problem as a multiple travelling salesman problem with the aim to maximize the received packet rate fairness. Also, the optimal allocation of resources in the UAV assisted communication system is application dependent and can vary between the types of UAVs. In particular, UAVs can be categorized into five main types of platforms: (i) drones, (ii) aircrafts, (iii) helikites, (iv) airships and (v) balloons [14]. Here, the expected challenges will depend on the platform that is chosen to design the drone wireless communication network. For example, drones, aircrafts and airships can guarantee a wide area range with heavier payloads and optimal selection with better antenna placement. On the other hand, aircraft guarantee the extreme

airtime whereas drones can not. However, drones ensure the single person deployment with a wide range of size dependent costs and instant deployment [13, 15, 18, 45].

To summarize, energy efficiency, optimal placement and trajectory planning requires a careful and comprehensive framework for optimal utilization of drones in wireless communication systems. In this thesis, we will show only the placement of drones in the context of 3D spatial placement utilizing stochastic geometry analysis tools.

4. *Network back-hauling/front-hauling:* Drones are employed to serve in scenarios where a temporary short-time off-loading is required to improve the average area spectral efficiency and the total capacity of the network. This requires high data-rate and reliable links for the desired off-loading. In contrast to the traditional cellular network deployment, especially for macro-cells deployment where the back-haul is achieved via optical fibre links, drones especially in multi-tier networks as flying BSs, require a wireless back-haul/front-haul. The resiliency and hovering instability of drones, as they may move around, raises some back-hauling challenges. Millimetre-wave (mmWave) can be considered as one of the key drivers for back-hauling in the DSCNs. The main enabling features in mmWaves are: (i) the large bandwidth available which gives higher data rates for the off-loading desired needs, (ii) higher resolution, (iii) small component sizes that fit efficiently on an energy-aware applications and (iv) low interference due to the short wavelength and reflection characteristics [46]. Similarly, the exploitation of free-space optics (FSOs) is a promising solution [16]. What makes the FSOs promising are: (i) higher data rates can be achieved, (ii) no need for spectrum licensing and frequency coordination between users and (iii) immunity to radio

frequency interference [47]. Despite the well known drawbacks, the authors in [16] showed that GBits data rates can be achieved using drones to implement the network Vertical back-haul/front-haul. Consider also drone front-hauling, when cellular BSs have no direct link to the base station controller (BSC). In this situation, the drone is deployed to link the BS to the core network [46]. In this thesis, we assume that the back-haul link is always secured and hence we analyse the performance of the downlink communication while the back-hauling is out of the scope of the thesis.

5. *Architecture and control*: While the use of drones is flourishing and emerging in many applications, the design of the network is target dependant. Accordingly, there is a concern about the key technology drivers to be adopted to achieve connectivity and reliability amongst the DSCN elements. First, a global information monitoring about the drone cellular BSs should be accessible in real-time. This requires an active comprehensive framework which gathers data from multiple cells at the same time. A general drone-cell management framework (DMF) is presented in [17, 48]. The use of software defined networks (SDNs) is proposed. The network can forward a global vision information about the network elements and paths in the forwarding information base (FIB) fashion. Consequently, the SDN based controller can resiliently remove and add paths to the drone distribution network (DDN). Also, we need to diminish the OPEX of the entire network. To this end, the network functions virtualization (NFV) is proposed to reduce the use of standard switches, storage devices, and security firewalls, etc. That is, on demand cloud resources with big data controllers can also be exploited. Even with the promising features for a centralized DMF, the framework comes with

TABLE 1.1: Categories of current literature on drone communication.

Research field	Related work
Channel models	[7, 30–33]
Performance analysis	[6, 12, 19, 22, 37, 38]
Network back-hauling/front-hauling	[16, 46, 47, 49]
Architecture and Control	[17, 48]
Optimal placement and energy efficiency	[13, 15, 18, 39–45, 50]

the same embedded challenges of the SDNs and NFVs (i.e., scalability, efficiency in FIB, and communicating with different virtual network entities). Consequently, a scalable, resilient and comprehensive operation framework has to be adopted with the features overcoming the embedded challenges in every network component of the operation.

To summarize the current literature on drone assisted wireless communications, we break down the relevant literature as in Table 1.1[5].

1.3 Thesis Outline and Contributions

In this thesis we aim to study several performance aspects for employing drones in achieving resilient smart-cities in future cellular networks. Generally, we focus on the implementation and modelling for an optimal parametrization framework of the DSCNs for recovery networks in a post-disaster and network off-loading scenario. Also, to build the grand vision, we focus on the interference management of the DSCNs.

[5]Table 1.1 and the literature review we made in this section shows only some of the work in the field and only tries to highlight the relevant challenges in drone-assisted communication systems. However, more extensions will be presented in the next chapters.

As shown in Figure 1.4 the contribution of this thesis can be broken down into four main categories:

1. *Optimal dimensioning and performance analysis of drone-based wireless communications:* Unlike the traditional cellular cell, DSCs is constrained by different channel conditions and different path-loss models. Also, the vertical coverage will force us to deal with different configurations (e.g., antenna main beam-width, vertical and horizontal tilting angle) for the directional antennas to be used. Here, we define and introduce the optimal key parameters which play the main role in optimal utilization of the drone small cells. To this end, we aim to study the effect of altering the drone altitude and antenna gain patterns on the overall performance for the deployed small cells. In this context, we prove the existence of drone optimal altitude based on the selected cell configurations. We will construct the study based on a general Rayleigh fading channel and the dual-slope path-loss model. We also show some performance metrics that prove the existence of the desired optimal dimensioning for the geometry deployment. In particular, we will focus on three deployment geometries: (i) single flying cell deployment for general wireless communication, (ii) finite number of drones serving in post-disasters scenarios for cellular network recovery overlaying a partially destroyed cellular network and (iii) drone enabled recovery networks in cluster based fashion where the drones are distributed in clusters and user centric spatial distributions.

2. *Interference management for drone-based recovery networks:* In an analogous fashion to the heterogeneous network implementation, the deployment of drone-based networks requires a simple and critical resource management in order to achieve the best utilization of the total network

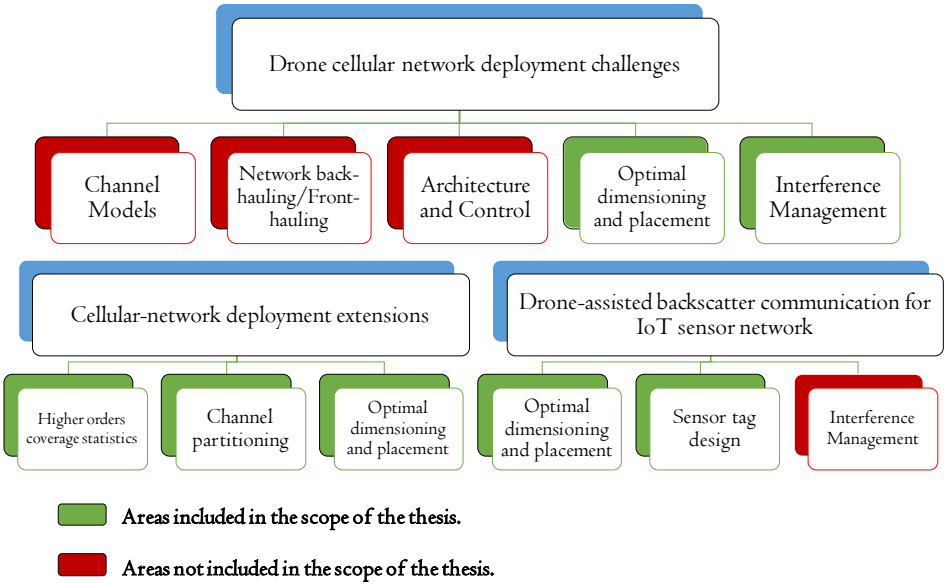

FIGURE 1.4: Challenges for large-scale deployment and scope of the thesis.

capacity. Here, we will show a stochastic spatial modelling of the DSCN overlaying the conventional cellular network. We will try to build a comprehensive analytical models to characterize the aggregate interference in the proposed network model as a key performance indicator in terms of the coverage probability and area spectral efficiency. To this end, we will show an optimal comprehensive framework based on stochastic geometry tools for an optimal design and configuration of the DSCN. We will show that, design of DSCNs is subjected to some conditions defining the entire frame of the networks. For instance, the network average altitude and the number of drone base stations comprising the whole network are key parameters. In more realistic spatial distributions, we will extend the network model to study the interference in user-centric network spatial distributions. Finally, we will discuss the network configuration frontier that defines the feasibility of DSCNs and the exploitation in future cellular networks.

3. *Higher ordered statistics for optimal coverage analysis of a downlink cellular network*: As we described before, drone communication networks can be analysed in a similar way to the traditional cellular network. However, the difference is in the channel models and the vertical bottom-up design. In literature, stochastic geometry has been widely used for performance analysis of heterogeneous cellular networks. One of the main concepts that has been introduced in the performance analysis of cellular networks using stochastic geometry tools is that increasing the BSs density does not affect the first-order statistics of the SIR (i.e., coverage and coverage rate). In other words, the densification of the cellular network with more BSs results in the same coverage probability but increases the area spectral efficiency (ASE). By studying the optimal dimensioning of DSCNs, we will show that this fact is not valid and there is always an optimal BS density in every deployment of the network. With the similarities in the large-scale deployment between the DSCNs and the traditional cellular networks (e.g., LoS and NLoS link characteristics), we predict the same concept to apply.

   In the cellular networks context, we will try to answer the question which has intrigued the network designers for years: How are coverage and throughput related to the deployment density?. To answer this question, the performance of large-scale cellular networks must be quantified in terms of underlying design parameters such as BS density and height, path-loss exponents, transmit power employed by BSs and available channel resources, etc. Hence, we will re-address the cellular network design from new aspects and we will show that by analysing higher-order statistics of the SIR and using realistic channel characterisation models will change the fundamental concept of the network densification and

hence new parameters of network design should be taken into account. In particular, we provide a new interference management framework in the context of cellular networks with the aim of increasing the users' fairness across the entire network.

4. *Coverage analysis of drone-assisted backscatter communication for IoT sensor network:* For more insight on the enabling technologies of smart cities, we will perform a comprehensive analysis on the use of drones in assisting the powerless backscatter communication for IoT applications. On this regard, we will show a system level design coupled with statistical coverage analysis in order to define the optimal points of operation in a finite field of backscatter nodes. The framework that we will present is implicitly incorporates realistic propagation dynamics of communication between the flying drone and the backscatter sensor nodes by employing the large-scale path-loss model which accommodates both LoS and NLoS link states and employing the small-scale fading model which captures the dyadic nature of backscatter communication (i.e., forward propagation A2G and G2A may experience non-zero correlation).

The rest of the thesis will comprise 6 chapters as follows:

- **Chapter 2**: In this chapter, we will introduce a quick theoretical background over the substantial mathematical and statistical tools that we will use in the rest of the thesis. In particular, we will focus on presenting models from stochastic geometry. We focus on presenting the theoretical characteristics of general point processes (PP) and the relevant distance distributions related to the chosen spatial distributions. We also highlight some of the large-scale path-loss models that we will use throughout the thesis.

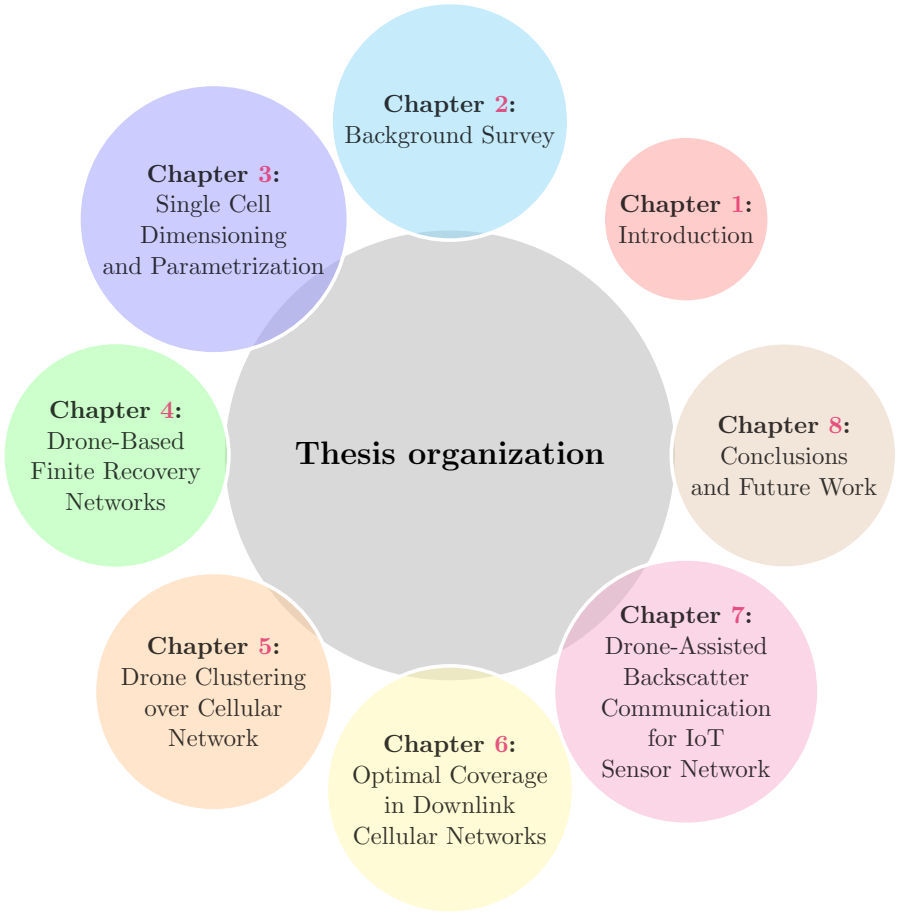

FIGURE 1.5: Thesis organization.

- **Chapter 3**: In this chapter, we present an optimal dimensioning for a single DCS. We study an isolated cell which can be utilized for both cellular communications or any general type of wireless communications. Assuming a circular shaped cell with a simple uniform distribution of users inside the coverage area, we aim to answer the question: "Given a certain cell diameter, uniform user distribution, certain antenna gain pattern and certain drone altitude, what are the optimal cell parameters to maximize coverage and bit error rate?". Hence, we extend the traditional models in drone-based communications to include transmitter antenna gain patterns and wireless channel multi-path fading. The

results in this chapter will be based on the published paper [51].

- **Chapter 4**: In this chapter, we will develop a more comprehensive framework for the design of DSCNs. In particular, we study the co-existence of DSCs in a bounded area on top of an operational ground cellular network in a post-disaster situation. We define and study the design parameters such as optimal altitude and number of DBSs, etc., as a function of destroyed BSs, propagation conditions, etc. To address these design issues, we present a comprehensive statistical framework which is developed from a stochastic geometric perspective to characterize the aggregate interference. We then employ the developed framework to investigate the impact of several parametric variations on the performance of the DSCNs. Without loss of generality, we employ the coverage probability of a down-link MU as a performance metric of the network in the existence of co-channel interferers. It is demonstrated that by intelligently selecting the number of drones and their corresponding altitudes, ground users coverage can be significantly enhanced. This is attained without incurring a significant performance penalty to the MUs which continue to be served from operating ground infrastructure. The results in this chapter will be based on the published paper [52].

- **Chapter 5**: In this chapter, we develop the work we present in chapter 4 for a more comprehensive statistical framework to characterize and model large-scale DSCNs enabled post-disaster scenario for wide range recovery cellular networks. In the case of natural or man-made disasters, the cellular network is vulnerable to destruction resulting in coverage voids or coverage holes. DSCNs can be rapidly deployed to fill such coverage voids. Due to capacity and back-hauling limitations on DSCs

each coverage hole is assumed to require a multitude of DSCs to meet the shortfall coverage at the desired QoS. Moreover, ground users also tend to cluster in hot-spots in a post-disaster scenario. Motivated by this fact, we consider clustered deployment of DSCs around the site of a destroyed BS. Joint consideration of partially operating BSs and deployed DSCs yields a unique topology for such PS networks.

Borrowing tools from stochastic geometry, we develop a statistical framework to quantify the downlink performance of a DSCN. Our proposed clustering mechanism extends the traditional Matern and Thomas cluster processes to a more general case where cluster size is dependent upon the size of the coverage hole. We then employ the newly developed framework to find closed-form expressions to quantify the coverage probability, area spectral efficiency (ASE) and the energy efficiency (EE) for the downlink MU. We also explore several design parameters (for both of the adopted cluster processes) that address optimal deployment of the network (i.e., number of drones per cluster, drone altitudes and transmit power ratio between the traditional surviving BSs and the DBSs). The results in this chapter will be based on the published papers [53, 54].

- **Chapter 6**: The previous chapters study the performance of a flying cellular network in terms of coverage probability and the existence of co-channel interference using a realistic A2G LoS and NLoS path-loss models. Noting the similarities in the optimal design between cellular networks and flying cellular networks, in this chapter, we present a detailed analysis of the coverage and spectral efficiency of a downlink cellular network in a similar way to what we investigated in previous chapters. However, rather than relying on the first order statistics of the received SIR, such as coverage probability, we focus on character-

izing the meta-distribution of the SIR. Our analysis will be based on the alpha-beta-gamma (ABG) path-loss model which provides us with the flexibility to analyse urban macro (UMa) and urban micro (UMi) deployments. With the help of an analytical framework, we demonstrate that selection of underlying degrees-of-freedom such as BS height for optimization of first order statistics such as coverage probability is not optimal in the network-wide sense. Consequently, the SIR meta-distribution must be employed to select appropriate operational points which will ensure consistent user experiences across the network. Our design framework reveals that the traditional results which advocate the lowering of BS heights or even optimal selection of BS height do not yield consistent service experience across users. By employing the developed framework we also demonstrate how available spectral resources in terms of time slots/channel partitions can be optimized by considering the meta-distribution of the SIR. The results in this chapter will be based on the published paper [55].

- **Chapter 7**: In this chapter, we develop a comprehensive framework to characterize the performance of a drone-assisted backscatter communication based IoT sensor network. We consider a scenario where the drone transmits an RF carrier that is modulated by IoT sensor node (SN) to transmit its data. The SN implements load modulation which results in amplitude shift keying (ASK) type modulation for the impinging RF carrier. In order to quantify the performance of the considered network, we characterize the coverage probability for the ground based SN node. The statistical framework developed to quantify the coverage probability explicitly accommodates a dyadic backscatter channel which experiences deeper fades than that of the one-way Rayleigh channel. Our model also

incorporates Line of Sight (LoS) and Non-LoS (NLoS) propagation states for accurately modelling large-scale path-loss between drone and SN. We consider spatially distributed SNs which can be modelled using a spatial Binomial Point Process (BPP). We practically implement the proposed system using Software Defined Radio (SDR) and a custom designed SN tag. The measurements of parameters such as noise figure, tag reflection coefficient etc., are used to parametrize the developed framework. Lastly, we demonstrate that there exists an optimal set of parameters which maximizes the coverage probability for the SN. The result in this paper will be based on the accepted paper for publication [56].

- **Chapter 8**: This chapter concludes the thesis and discusses possible future directions for research.

1.4 List of Publications

1. Ali Hayajneh, Syed Ali Raza Zaidi, Desmond C. McLernon and Mounir Ghogho, 2016, December. Optimal dimensioning and performance analysis of drone-based wireless communications. In Globecom Workshops (GC Wkshps), 2016 IEEE (pp. 1-6).

2. Ali Hayajneh, Syed Ali Raza Zaidi, Desmond C. McLernon and Mounir Ghogho, 2016, June. Drone empowered small cellular disaster recovery networks for resilient smart cities. In Sensing, Communication and Networking (SECON Workshops), 2016 IEEE International Conference on (pp. 1-6).

3. Ali Hayajneh, Syed Ali Raza Zaidi, Desmond C. McLernon and Mounir

Ghogho, "Performance analysis of UAV enabled disaster recovery network: A stochastic geometric framework based on matern cluster processes," IET 3rd International Conference on Intelligent Signal Processing (ISP 2017), London, 2017, pp. 1-6.

4. Ali Hayajneh, Syed Ali Raza Zaidi, Desmond C. McLernon, Marco Di Renzo and Mounir Ghogho, "Performance Analysis of UAV Enabled Disaster Recovery Networks: A Stochastic Geometric Framework Based on Cluster Processes," in IEEE Access, vol. 6, pp. 26215-26230, 2018.

5. Ali Hayajneh, S. A. R. Zaidi, Desmond C. McLernon, M. Z. Win, A. Imran and M. Ghogho, "Optimal Coverage and Rate in Downlink Cellular Networks: A SIR Meta-Distribution Based Approach," 2018 IEEE Global Communications Conference (GLOBECOM), Abu Dhabi, United Arab Emirates, 2018, pp. 1-7.

6. Ali Hayajneh, S. A. R. Zaidi, M. Hafeez, Desmond C. McLernon and M. Z. Win, "Coverage Analysis of Drone-Assisted Backscatter Communication for IoT Sensor Network", 1st International Workshop on Wireless sensors and Drones in Internet of Things (Wi-DroIT) 2019, Santorini Island, Greece (Accepted for publication).

Chapter 2

Theory Preamble

Contents

In this chapter, we will show the most relevant tools and models that we will use throughout the rest of the thesis. For the spatial modelling of the DSCNs and any general types of network, we will provide a brief view for tools from stochastic geometry. Finally, we will present some fading channel models from statistical and standardization aspects.

2.1 General Notations

Throughout this thesis, we employ the following mathematical notations. The counting measure of a point process $\Phi(\mathcal{B})$ provides a count of points inside the compact closed subset $\mathcal{B} \in \mathbb{R}^2$ (i.e., bounded area). The probability density function (PDF) for a random variable X is represented as $f_X(x)$ with the cumulative density function written as $F_X(x)$. The exclusion symbol $\setminus$ represents the exclusion of a subset from a superset. The expectation of a function $g(X)$

of a random variable X is represented as $\mathbb{E}_X[g(X)]$. The bold-face lower case letters (e.g., $\mathbf{x}$) are employed to denote a vector in $\mathbb{R}^2$ and $\|\mathbf{x}\|$ is its Euclidean norm. The Laplace transform (LT) of any random variable Z is $\mathcal{L}_Z(s)$ (i.e., LT of the PDF of the random variable).

2.2 Stochastic Geometry and Spatial Modelling of Point Processes

Stochastic geometry for spatial distribution modelling as part of graph theory has been widely used to model large-scale randomness and uncertainty of many physical systems, especially for wireless communication networks. Stochastic geometry theories provide yet accurate and powerful tools for the modelling of heterogeneous networks and any wirelessly spatially distributed networks [57, 58]. It is mainly utilized to model the location/displacement of the communicating nodes, BSs and mobile users (MUs) to evaluate the performance metrics of the SIR and to aggregate channel impairments effect (i.e., mainly the aggregate interference received from co-channel transmitting terminals). Given a particular set of points (i.e., BSs or MUs) that is distributed in the space, the distribution of the points across the observation space follows a specific type of point processes. That is, for the different kind of network geometries, an accurate modelling of the points distributed across the space is essential. For example, user-centric BS deployment of the cellular network needs cluster based distributions to accurately model the BS distribution while the traditional macro-cell deployment can only be modelled with a uniform distribution of points. As we will show in the next chapters, stochastic geometry provides powerful tools to solve for closed-form expressions for the primary

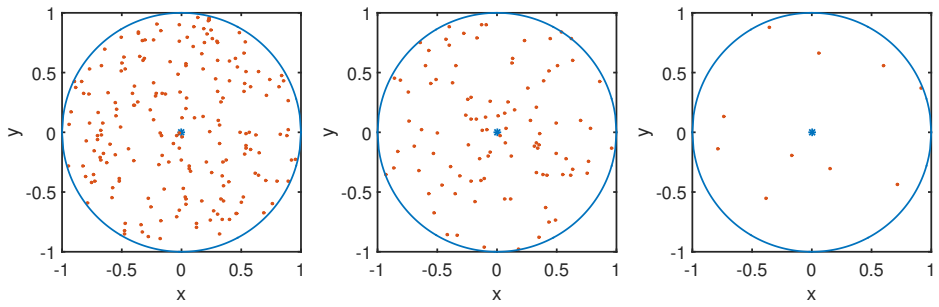

FIGURE 2.1: (left) A realization of a BPP with 200 nodes distributed in the unit circle. (centre) A realization of a BPP with 100 nodes distributed in the unit circle. (right) A realization of a BPP with 10 node distributed in the unit circle.

metric of performance (i.e., coverage, area spectral efficiency, statistics of SIR, etc.). We will also show how the deployment geometry of the wireless network requires a different and specific type of spatial distributions and requires different tools for analysis. In this section, we highlight some of the well known point processes, their related distance distribution characteristics, some of the stochastic geometry theories and the properties of the point process.

2.2.1 Binomial Point Process

We will start with the binomial point process (BPP)[1]. The BPP is mainly used to model the distribution and interaction of a fixed number of point/nodes distributed uniformly and independently inside a finite area (see Figure 2.1 for a two dimensional disk with unity radius). That is, the set space of the point process is defined as $\Phi = \{\mathbf{x_1}, \mathbf{x_2}, ..., \mathbf{x_N}\} \subset \mathbb{R}^d$, where N is the number of points in the set space and $\mathbf{x}_i$ is a shorthand to the d-dimensional vector $\mathbf{x}_i = \{x_1, x_2, ..., x_d\}$ in $\mathbb{R}^d$ [59,60]. For the set of nodes inside Φ, the probability of finding k points within the d-dimensional bounded annual $\mathcal{B}(A, B)$ is defined

[1]We will use the BPP to model the network geometry in chapter 4.

as follows [59]:

$$\mathbb{P}(\Phi(\mathcal{B}(0 \leq A < B \leq R)) = k) = \binom{N}{k} \left(\frac{|B-A|}{|R|}\right)^k \left(1 - \frac{|B-A|}{|R|}\right)^{N-k} \tag{2.1}$$

where $|.|$ is the Lebesgue measure which is simply for two dimensional space a collar of area $|B-A| = \pi(B^2 - A^2)$[2]. Here, we define the density of nodes in the d-dimensional space by [59, 61]:

$$\lambda = \frac{N}{C_d R^d}, \tag{2.2}$$

where C_d is the generalized Lebesgue measure of the unit-ball and can be written as $C_d = \pi^{\frac{d}{2}}/\Gamma(1 + d/2)$, where $\Gamma(z) = \int_0^\infty x^{z-1}e^{-x}\,\mathrm{d}x$. Intuitively for the a two dimensional unit-disk, the $C_2 = \pi\Gamma(2) = \pi$ and hence $\lambda = N/(\pi R^2)$ (points/unit-area). The most important property of the BPP is the non-stationary property:

- *Non-stationary:* The BPP is not a stationary process. That is, the characteristics of the chosen node are not the same as any point in other locations of the set space. For example, the distribution of the distance from any arbitrarily chosen node to the nearest point in the space is not the same for two different points $\mathbf{x_1}$ and $\mathbf{x_2}$. The BPP is considered as the basic distribution of all point processes. Namely, the BPP behaves as a Poisson point process (PPP) by letting $N \to \infty$ while keeping the density λ remaining the same as $R \to \infty$.

[2]Lebesgue measure is a way to assign a measure to a d-dimensional set space. It is, length, area and volume for the one, two and three dimensional set space, respectively. For $d > 3$ it is simply called volume.

2.2.2 Poisson Point Process

The most common process used to model the cellular networks randomness is the PPP. The main and principle term under the PPP is the homogeneity (stationary). That is, the average density of point/nodes in any Borel set $\Phi_{\mathcal{B}(0,R)} = \{\mathbf{x_1}, \mathbf{x_2}, ..., \mathbf{x_N}\} \in \mathcal{B}(0, R)$ is constant for any two independently and arbitrary chosen bounded areas in $\mathbb{R}^d$ [3]. With these preliminary properties, the probability of having n points/nodes in a subset B in $\mathbb{R}^d$ can be written as:

$$\mathbb{P}(\Phi(B) = k) = \exp\left(-\lambda|B|\right) \frac{\left(\lambda|B|\right)^k}{k!}, \tag{2.3}$$

where again $|.|$ is the Lebesgue measure. Hence, the counting measure of the 2-dimensional disk with radius r can be written as:

$$\mathbb{P}(\Phi(B) = k) = \frac{\left(\pi\lambda r^2\right)^k}{k!} \exp\left(-\pi\lambda r^2\right). \tag{2.4}$$

A special case of this probability is called the void probability. That is, assuming that there is no point inside a ball of radius R then $p^o = \mathbb{P}(\Phi(B) = 0) = \exp\left(-\pi\lambda R^2\right)$ (later noted as void probability). The main properties and comments on the PPP are:

- **Stationarity:** The PPP is a stationary process. That is, the characteristics of any arbitrarily chosen node are the same as any other point in other location of the set space. Hence, a general assumption on many wireless networks is the homogeneity and hence we model them by a

[3] The Borel set is a subset of the infinite topological open space which can be formed through countable intersection and union operations or any complementary relevant operation.

PPP.

- **In-homogeneous PPP:** An in-homogeneous PPP can be modeled in a way similar to (2.3), by simply replacing $\lambda|B|$ with $\int_B \lambda(r)dr$ [61]. Hence, the general counting measure of an in-homogeneous PPP can be written with respect to the intensity measure $\Lambda(B)$ as:

$$\mathbb{P}(\Phi(B) = k) = \exp\big(-\Lambda(B)\big) \frac{\big(\Lambda(B)\big)^k}{k!} \tag{2.5}$$

  In fact, the homogeneous PPP is a special case of the in-homogeneous PPP where the density of the points/nodes is constant ($\lambda(r) = \lambda$).

The PPP can be considered as a parent process to model different kind of geometries. For instant, assume a PPP modelling the location of BSs on the two dimensional space with MUs clustering around the BSs. Then the resulting point process is called a clustered point process.

2.2.3 Theorems and properties

Void Probability

This is the probability that the point process has no point at a given bounded area and can be written as

$$v_d(B) = \mathbb{P}\left(\Phi(B) = 0\right). \tag{2.6}$$

This can be evaluated for a general PPP with intensity measure $\Lambda(B)$ as

$$v_d(B) = \exp(-\Lambda(B)). \tag{2.7}$$

In cellular communication networks, the void probability is used to measure the distance distribution between the user at the origin of the area and the nearest neighbour BS for the modelling of nearest neighbour association scheme. That is, given a MU at the origin of a homogeneous PPP cellular network, then the distance R_1 to the nearest neighbour BS and the MU has the cumulative distribution function (CDF) $F_{R_1}(r_1) = \exp\left(-\pi\lambda r_1^2\right)$. In fact, this distance is in between two different sets of point processes (i.e., the MUs and the BSs) and the void probability cannot give the nearest distance distribution without taking into consideration the Slivnyak's theorem. According to Slivnyak's theorem, adding or removing a point from/to the PPP does not affect the properties of the point process. So, a MU added to the BSs set-space will preserve the characteristics of the BSs modelling point process.

Thinning

In many communication networks, the thinning process, $p(x)$-thinning process, is used to model the removal of points (nodes) from the set of all points that comprise the network point process. In the context of the thesis, thinning can be used to model the outage of some BSs due to destruction in a post-disaster scenario. We only focus on the uniform thinning without marking nor conditioning on the distance between the points. That is, we randomly remove points with probability of removal $p(x)$. As a result, the point process intensity measure can be obtained by

$$\Lambda_{p(x)}(B) = \int_B (1 - p(x))\Lambda(dx) \tag{2.8}$$

which is for a homogeneous PPP of density λ and constant probability of thinning $p(x) = p$ can be simply evaluated as $\lambda_t = (1-p)\lambda$. In the context of modelling a post-disaster cellular network, the distribution of the retained BSs

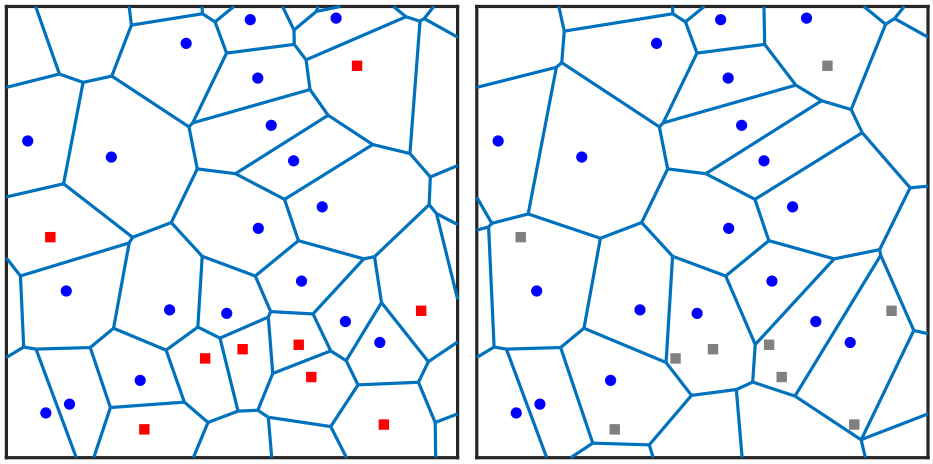

FIGURE 2.2: (a) A snapshot of a PPP modelling the location of BSs (blue circles and red squares) in a macro cell deployment of density λ_{BS}. The red squares represent destroyed BSs with probability of 0.3. (b) The same PPP in (a) when the destroyed BSs are removed from the network topology with new Voronoi tessellation for the resulting PPP of the density $(1-0.3)\lambda_{BS}$.

after the disaster can be modelled as a thinned PPP. That is, if we assume that a BS in a cellular network of density λ_{BS} has the probability p_d to be destroyed, then we can model the retained intact BSs by a new PPP with a density of $\lambda_2 = (1-p_d)\lambda_{BS}$ (see Figure 2.2 for visual illustration). The thinning process can also be used to model the effect of channel re-use in cellular networks. That is, if the network uses N number of carriers, the effective BSs density is $1/N$ for a fully-loaded network. However, this does not affect the nearest neighbour statistics for MU-BS association.

Probability generating and Laplace generating functionals

Probability generating and Laplace generating functionals are widely used to measure the aggregate interference experienced by a node in a wireless network. In wireless networks, the functionals provide a tractable tool to model the performance of the networks. The probability generating functional for a PPP

Φ can be modelled for a measurable function $v(x)$ as [62][4]:

$$G(v) = \mathbb{E}\left(\prod_{x\in\Phi} v(x)\right) = \exp\left(-\int_{\mathbb{R}^d} \big(1 - v(x)\big)\, \Lambda(dx)\right). \tag{2.9}$$

For the Laplace functional $L(u)$ we substitute $L(u) = G(\exp(-u))$ and hence we can write:

$$L(u) = \mathbb{E}\left(\prod_{x\in\Phi} v(x)\right) = \exp\left(-\int_{\mathbb{R}^d} \big(1 - \exp(-u(x))\big)\, \Lambda(dx)\right). \tag{2.10}$$

For instant, the Laplace functional for a two dimensional PPP of density λ can be written as

$$L(u) = \exp\left(-\int_0^\infty \big(1 - \exp(-u(r))\big)\, 2\pi\lambda r\, \mathrm{d}r\right). \tag{2.11}$$

2.3 Distance Distributions in Random Networks

In studying the spatial distribution of points/nodes/MUs inside the coverage area we importantly study the distance distributions inside the considered area of study. By modelling the distance distribution, we can evaluate the effect of interference by averaging over the distance distribution on the space. Also, in many communication systems the successful link connection from the MU to the serving node/base station is considered to be the largest strength signal. But, due to the direct relation between the average received signal strength and the distance between the two ends (i.e., $P \propto \frac{1}{r}$), knowledge of

[4]Note that the probability generating functional can be used to measure the void probability by setting $v(x) = 1 - \mathbb{1}_B(x)$ which results in $\prod_{x\in\Phi} v(x) = 1$ and then $\mathbb{P}\big(\Phi(B) = 0\big) = \exp(-\Lambda(B))$. This can be written for a PPP as $\mathbb{P}\big(\Phi(B) = 0\big) = \exp\big(-\pi\lambda r^2\big)$.

the nearest neighbour distributions is substantial for the performance analysis of the communication system. In the following, we show the most widely used distance distributions for the spatially distributed networks and users.

2.3.1 Distance Distributions in BPP

In any compact set of N nodes distributed inside the a disc $b(0, R)$, we can write the distance from any node on the disc to the centre of the disc as a uniform random variable with PDF:

$$f_R(r) = \frac{2r}{R^2}, \tag{2.12}$$

which has an average $\mathbb{E}_R[r] = \frac{2}{3R}$. This distribution is the basic distribution of the uniformly distributed nodes in the space. The distance distribution from the centre of $b(0, R)$ to the $n-$th nearest node in the 2-dimensional space follows the generalized beta distribution as

$$f_{R_n}(r) = \frac{2}{R}\frac{\Gamma(n+\frac{1}{2})\Gamma(n+1)}{\Gamma(n)\Gamma(n+\frac{3}{2})}\beta\left(\frac{r^2}{R^2}; n+\frac{1}{2}, N-n+1\right), \tag{2.13}$$

where $\beta(z; a, b) = \frac{1}{B(a,b)}z^{a-1}(1-z)^{b-1}$ is the beta density function and $B(a, b)$ is the beta function [63–65][5]. The first nearest neighbour distance distribution in a BPP can be written as

$$f_R(r) = \frac{2N}{r}\left(1-\left(\frac{r}{R}\right)^2\right)^{N-1}\left(\frac{r}{R}\right)^2. \tag{2.14}$$

In chapter 5, we will show an extension to (2.14) to count for the dis-

[5] Another formula for the nearest nth neighbour for a general d-dimensional BPP in [63, 64].

tance distribution between any two chosen points in the set space.

2.3.2 Distance Distributions in PPP

The nth nearest neighbour distance distribution can be obtained for a two dimensional homogeneous PPP as:

$$f_{R_n}(r) = \frac{2(\lambda C_2 r^2)^n}{r\Gamma(n)} \exp\left(-\lambda C_2 r^2\right). \tag{2.15}$$

For the first nearest neighbour distance distribution, we can write:

$$f_{R_1}(r_1) = 2\pi\lambda r \exp(-\pi\lambda r^2). \tag{2.16}$$

Since the PPP is a single parameter process (i.e., depends only on the density λ), applying any point process operation such as thinning and clustering directly changes the distance statistics of the process (see Figure 2.3 for an example of applying the thinning process to the homogeneous PPP). In the next chapters we will introduce an extra distance distributions for the selected point processes of the study. We will show distance characteristics for cluster processes and some other processes (see chapter 5 for details).

2.4 Wireless Channel Model

For the best and most accurate modelling and management of the wireless networks, we define the propagation models of the studied channels and terrains. That is, the optimal design of the wireless network for minimal interference

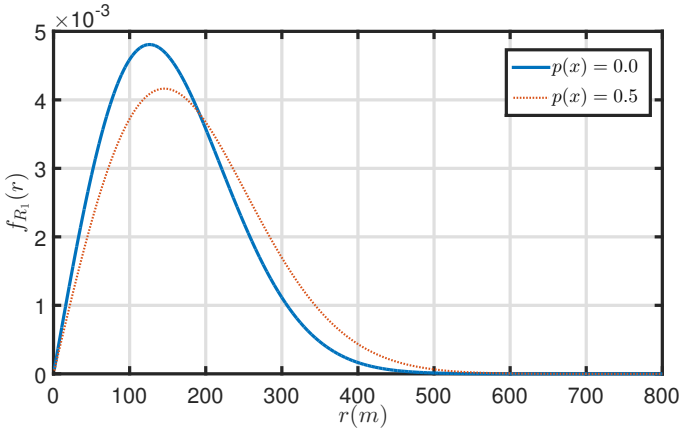

FIGURE 2.3: Probability density function for the first nearest neighbour distance $f_{R_1}(r)$ vs. the distance to the nearest neighbour for PPP. The density of the original PPP (blue solid line) is $\lambda = 10^{-5}$ where the (dashed orange line) is for an independently thinned PPP with $p(x) = 0.5$.

effect requires an accurate knowledge of the expected received signal from any arbitrary receiver in the network and this differs between the different cell size (i.e., femto, pico, small, micro and macro) and terrain type (i.e., urban, rural and metropolitan) of the cellular network. Wireless channel models can be categorized into small-scale and large-scale fading models.

2.4.1 Small-Scale Fading

In a wireless communication channel, signals experience changes in both the amplitude and phase of the transmitted signal. Due to the attenuation and phase shifts that the transmitted signal experiences, the received signal at the receiver terminal consists of a superposition of multiple copies of the transmitted signal, whereas each copy encounters different path characteristics. As a result, each of the received copies experiences differences in amplitude, phase shift and time delay. As illustrated in Figure 2.4, the characteristics of the fad-

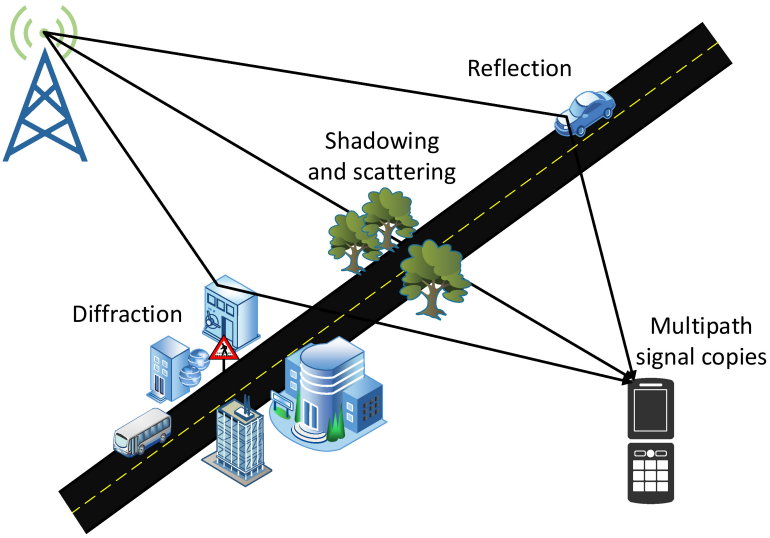

FIGURE 2.4: Multi-path fading effect.

ing channel itself change according to the number of reflectors and refractors. Thus, the number of received copies and the relative delays of all different copies of the signal vary with time. These kinds of random variations, according to the central limit theorem, makes the distribution of the complex superposition of the received signals a zero mean complex-valued Gaussian random process (ZMCGRP). As a result, the phase-shift experienced by every copy of the transmitted signal can be modelled by a random variable uniformly distributed (i.e., phase-shift varies between 0 and 2π) while the gain distribution of the fading coefficient will depend on the propagation media conditions. In this thesis, we will only focus on modelling the small-scale fading coefficient with a Rayleigh distribution.

The Rayleigh distribution is widely used to model the envelope of the multi-path fading channel when many fixed reflectors and scatterers exist. Namely, the channel with ZMCGRP impulse response and unity mean fading

coefficient has an envelope with the following probability distribution function (PDF):

$$f_G(g) = 2g \exp\left(-g^2\right). \tag{2.17}$$

In addition, with simple random variable transformation, the distribution of the power gain, $h = |g|^2$, of a unity mean Rayleigh fading channel can be written as:

$$f_H(h) = \exp\left(-h\right). \tag{2.18}$$

In the rest of the thesis we denote unity power gain Rayleigh fading by $h \sim \exp(1)$.

2.4.2 Large-Scale Fading

In general, large-scale fading is represented by the path-loss which is defined by the ratio between the received and transmitted signals assuming no multi-path fading. That is, the path-loss can be obtained as

$$PL = P_r - P_t \text{ dB}, \tag{2.19}$$

which can be written for general path-loss models as:

$$L(d) = \zeta + 10\alpha \log_{10}(d) \text{ dB}, \tag{2.20}$$

where P_r and P_t are the received and the transmitted signal powers, respectively. ζ is the excess frequency dependent path-loss value and α is the path-

TABLE 2.1: Path-loss models summery. All the distance (d) values are in km.

Type	$PL =$	**Frequency**
Macro Cells (Rural open area)	$90.7 + 31.8\log_{10}(d)$	900 MHz
Macro Cells (Rural quasi open)	$95.7 + 31.8\log_{10}(d)$	900 MHz
Macro Cells (Urban)	$123.3 + 33.7\log_{10}(d)$	900 MHz
Macro Cells (Rural open area)	$100.1 + 33.3\log_{10}(d)$	1800 MHz
Macro Cells (Rural quasi open)	$105.1 + 33.3\log_{10}(d)$	1800 MHz
Macro Cells (Urban)	$133.2 + 33.8\log_{10}(d)$	1800 MHz
Small Cells	$132.8 + 38.0\log_{10}(d)$	900 MHz
Small Cells (Medium sized cities)	$142.9 + 38.0\log_{10}(d)$	1800 MHz
Small Cells (Metropolitan centers)	$145.3 + 38.0\log_{10}(d)$	1800 MHz
Micro Cells	$101.7 + 26.0\log_{10}(d)$	900 MHz
Micro Cells	$145.3 + 38.0\log_{10}(d)$	1800 MHz

loss exponent. In many applications like cognitive radio communication, the interference management is not only affected by the transmission power generated by the interfering terminals/base stations. Indeed, the path-loss exponent is very important to build the architecture of the network and define the network elements and configuration parameters [60, 66, 67]. Path-loss statistics depend on the terrain of the area and the distribution of buildings and obstacles. In table 2.1 [68, 69], we can see that the path-loss model varies with the variation of the deployment geometry and hence the design of the network will change accordingly [68, 69]. In addition to Table 2.1, [7, 70] introduce a comprehensive surveys on the UAV to ground path-loss models, we summarize some of them as follows:

1. *A2G models*: For the A2G path-loss models, there is multiple formulas based on analytical, simulations or practical setups. The authors in [6] introduced a dual slope path-loss model based on ray tracing measure-

ments. The path-loss model can be written as

$$L_i(h,\theta)_{dB} = \zeta_i + 10\log_{10}\left(K_i\left(\frac{h}{\sin(\theta)}\right)^2\right), \tag{2.21}$$

where $K_i = \big((4\pi f)/c\big)^2$, f is the frequency, θ is the elevation angle, c is the light speed and ζ_i is the excess path-loss for $i \in \{LoS, NLoS\}$ in dB. For $f = 2000$ MHz ζ_{LoS} and ζ_{NLoS} have typical values $\{\zeta_{LoS}, \zeta_{NLoS}\} = \{0.1, 21\}$ for sub-urban, $\{\zeta_{LoS}, \zeta_{NLoS}\} = \{1, 20\}$ for urban, $\{\zeta_{LoS}, \zeta_{NLoS}\} = \{1.6, 23\}$ for dense-urban and $\{\zeta_{LoS}, \zeta_{NLoS}\} = \{2.3, 34\}$ for high-rise urban. We will use this formula in the rest of the chapter to capture the path-loss for the G2A link for LoS and NLoS scenarios. Furthermore, the probability of having a LoS A2G link is as follows:

$$\mathcal{P}_{LoS}(h,r) = \frac{1}{1 + a_1\, \mathrm{e}^{-b_1 c_1\, \tan^{-1}\left(\frac{h}{r}\right) + b_1\, a_1}}, \tag{2.22}$$

where a_1 and b_1 are environment-dependent constants with $c_1 = 180/\pi$. a_1 and b_1 have typical values $\{a_1, b_1\} = \{0.1, 21\}$ for sub-urban, $\{a_1, b_1\} = \{1, 20\}$ for urban, $\{a_1, b_1\} = \{1.6, 23\}$ for dense-urban and $\{a_1, b_1\} = \{2.3, 34\}$ for high-rise urban. This formula of the path-loss model has no limitations of the drone height and is valid for multiple environments and system parameters (i.e., for different city type and different carrier frequencies).

Another formula for the A2G path-loss is introduced in [33]. The paper shows that A2G path-loss follows two main propagation groups (i.e., two different path-loss profiles). The paper illustrate the methodology of which the model was deduced, as well as the different path-loss profiles including the occurrence probability of each profile (i.e., LoS and NLoS).

The total path-loss for LAP can be written as:

$$L(h,\theta) = 20\log\left(\frac{h-1.5}{\sin(\theta)}\right) + 20\log(f_{MHz}) - 27.55 + \eta_i, \quad i \in \{1,2\}, \tag{2.23}$$

where η_i is the excess path-loss which is a frequency and environment dependent. The value of η follows two groups, the first for LoS link and the second for NLoS. η_i is actually a random variable with an average of μ_i which can be found in [33]. Hence, probability of LoS can be quantified as follows:

$$\mathcal{P}_{LoS}(h,\theta) = \xi.(\theta - \theta_o)^{\sigma}, \tag{2.24}$$

where ξ and σ are frequency and environment dependent parameters obtained by curve fitting, θ_o is the minimum allowed elevation angle and has a value of $\theta_o = \pi/12$. Typical values for ξ and σ are available in table II of [33].

2. *C2A models*: These types of path-loss models are important for the modelling of the back-haul/front-haul links. However, this is out of the scope of the thesis. However, the most used formula in the literature for the C2A in suburban environments is given by [34]. The provided model is derived based on experimental data measurements conducted in a suburban environment for both terrestrial and aerial coverage. The C2A path-loss model can be written as

$$\mathcal{P}_{LoS}(d,\theta) = \underbrace{10\alpha\log(d)}_{\text{Terrestrial path-loss}} + \underbrace{A(\theta-\theta_o)\exp\left(-\frac{\theta-\theta_o}{B}\right) + \eta_o + \mathcal{N}(0, a\theta + \sigma_o)}_{\text{Aerial excess path-loss}}, \tag{2.25}$$

where d is the horizontal distance between the UAV and the cellular BS,

θ is the elevation angle, $\alpha = 3.04$ is the terrestrial path-loss exponent, $A = -23.29$ is the path-loss scaler, $\theta_o = -3.61$ is the angle loss offset, $B = 4.14$ is the angle scaler, $\eta_o = 20.70$ is the path-loss offset, $a = -0.41$ is the shadowing slope and $\sigma_o = 5.86$ is the shadowing offset.

3. *G2A path-loss model*: As we mentioned before, the uplink path loss model is not extensively studied in the literature despite some effort introduced in [71]. In this paper, the authors studied the impact of indoor and outdoor environments on the uplink and downlink path-loss models. For the uplink model, they gave two models based on two-ray and Winner-II. In their paper, they conclude that the Winner-II path-loss-model gives better modelling for the uplink channel for an urban emergency scenario. The path-loss model for the G2A in urban areas can be written as

$$\begin{aligned}\mathcal{P}_{LoS}(h, d_{out}) &= (44.9 - 6.55\log(h))\log(d_{in} + d_{out}) + 3446 + 5.83\log(h) \\ &\quad +23\log(f_c/5.0) + 17.4 + 0.5d_{in} - 0.8h_{MU} + L_o, \quad (2.26)\end{aligned}$$

where h is height of UAV mounted BS, d_{out} is aerial distance of the MU to UAV, d_{in} is the indoor distance of the MU in their building or house, h_{MU} is the height of the MU, f_c is the frequency in GHz and L_o is the additional indoor path-loss component due to the indoor obstacles like dividers, furniture.

As we mentioned in chapter 1, the path-loss model is a challenging problem for the optimal deployment of the DSCNs. In the next chapters, we will introduce the optimal parametrization design for the network geometry based on a statistical and practical modelling of the A2G path-loss model

which is the baseline for the following chapters. As we also described before, we will discuss a more practical path-loss model (i.e., $\alpha-\beta-\gamma$ path-loss model) to take into account the BS heights and to give more precise information about the network fairness for the service providers.

Chapter 3

Single Cell Dimensioning and Parametrization

Contents

In this chapter, we present the fundamental optimal dimensioning for single drone small cells (DSCs). For a more comprehensive addition to the literature, we extend the spatial and statistical modelling parameters that should be taken in the topology deployment for drone wireless communication systems. In-particular, transmitter antenna gain pattern and multi-path fading channel effects are considered. The aim objective of this chapter is to show that for certain cell setup parameters and coverage area, there is an optimal drone altitude that secures the best performance results. To this end, optimization is done by averaging for the studied performance metrics over all the down-link user (DU) locations inside the drone coverage area.

3.1 Introduction

As previously discussed in chapter 1, BSs acting as small cells in modern wireless communication systems have become a rapidly advancing and promising new technology. The main contribution in this field grows in parallel with

public safety and relief communication services. So, a significant attention is directed toward the optimization and utilization of low altitude platforms (LAPs) that communicate with ground-based systems in applications like PS, IoT communication, disaster relief communication services and coverage in high user-density scenarios like football games and any other crowded venues. Indeed, a substantial advantage of using drones to deploy the cells DSCs is that the cell topology and configuration parameters can be modified and tuned as required. In contrast to the fixed architecture of cellular networks (e.g., fixed locations/ heights of the BSs, etc.) drone heights and locations can be optimally modified to serve specific applications like hot-spots, disaster management, etc [72–75]. In this chapter, we address the optimal dimensioning of single cell deployment geometry.

3.1.1 Related Work

In the literature, design parameter optimization for DSCs is only addressed in terms of coverage probability but without taking into account the effect of the multi-path fading or any antenna pattern effects. Furthermore, most of the papers consider only optimization for one user and without taking into account the geometry of all the users across the actual coverage area. As an example, the authors in [12] introduced the use of DSCs to provide a service for air-to-ground devices in the scenario of device centric architecture and circular coverage areas. In this paper the authors investigate the optimal DSC altitude which leads to a maximum ground coverage and minimum required transmit power for a single DSC. In addition, the optimization considered two parameters, where the first is the distance between the two serving drones

where the interference are between them is probable and the second is the altitude of the drones. Due to parametrization limited studies, we will provide more wider parametrization.

In DSC applications, the path-loss calculations should consider a number of non-traditional models. To this end, the A2G average path-loss for LAPs in urban environments is investigated in many papers where it is expressed in terms of the LoS probability and excess path-loss [32, 33, 76]. In-particular, the authors in [32] show that the probability of LoS depends on the elevation angle of the MU and some other environment dependent parameters. So the variation of the path-loss as a function of the elevation angle, will lead to an optimal height for the drone. An analogous situation is the one for BS heights in the underlay cellular networks.

It is important to note however, as we will discuss later in the next chapters, that for heterogeneous networks the density of the users is not the same inside the entire coverage area. Accordingly, some areas may be defined as hot-spots and others as low or average density. Thus, the intensity and directivity pattern of the antenna are important for two reasons: the first is to decrease interference in the co-channel DSCs or the underlay cellular networks and the second is to concentrate more system resources to the higher density areas. In this context, many antenna gain patterns can be considered from theoretical to practical recommendations. Here, we will adopt the same models proposed in [68, 77, 78]. Note that, a comprehensive study on the conceptual framework of the architecture, standardization and cross platform design are still major issues. However, this will be studied in the next chapters and the framework will be extended to capture multiple scenarios and network geometries.

3.1.2 Contribution

In this chapter, we address the fundamental optimal dimensioning of the single drone small cells. We mainly focus on the scenarios where the drone is serving as flying BS for cellular voice and data traffic. However, this parametrization framework is also valid for other types of communication networks. For example, the design of data gathering drones which work in a sensor node field is basically the same but needs more investigation in the channel model to reflect the ground-to-air channel characteristics on the overall design. In addition, air to ground back/front-hauling in D2D and M2M communication can be designed in the same manner. Finally, the contribution and organization of this chapter can be summarized as follows:

1. More comprehensive modeling and parametrization is considered in terms of path-loss and comparison between two antenna propagation patterns (see section 3.2).

2. We numerically prove the existence of an optimal drone height that leads to optimal average performance metrics for all the possible locations of the MU in the drone coverage area (see section 3.3 for analysis and section 3.4 for the discussion of the numerical and simulation results).

3. We study the effect of changing the drone height over three performance metrics. Namely, coverage probability, bit error rate and coverage capacity (see section 3.3).

3.2 System Model

In this section we introduce both the geometrical configuration of a drone-based cell and the overall budget of the link between the drone (i.e., BS) and the MU (i.e., the receiver).

3.2.1 Deployment Geometry

We consider a drone under the control of a ground positioning system optimizing the height of the drone in order to achieve the optimal desired performance according to the quality of service (QoS) constraints. As illustrated in Figure 3.1, the drone is serving a circular coverage area with radius of R_o, and any MU is assumed to be inside this coverage area (where the users are uniformly distributed). Any user is located at a distance r from the centre of the coverage area (i.e., the projection of the drone onto the ground). The elevation angle of the drone to that specific user is θ rads, which is defined as the inner angle between the ground and the line connecting the MU to the drone. The drone in this model is located at h in meters, which is the height from the ground. It is bounded between the minimum height h_{min} (i.e., taking into account buildings and any obstructions) and the maximum height h_{max} (i.e., considering the capability of the serving drone to reach that maximum height).

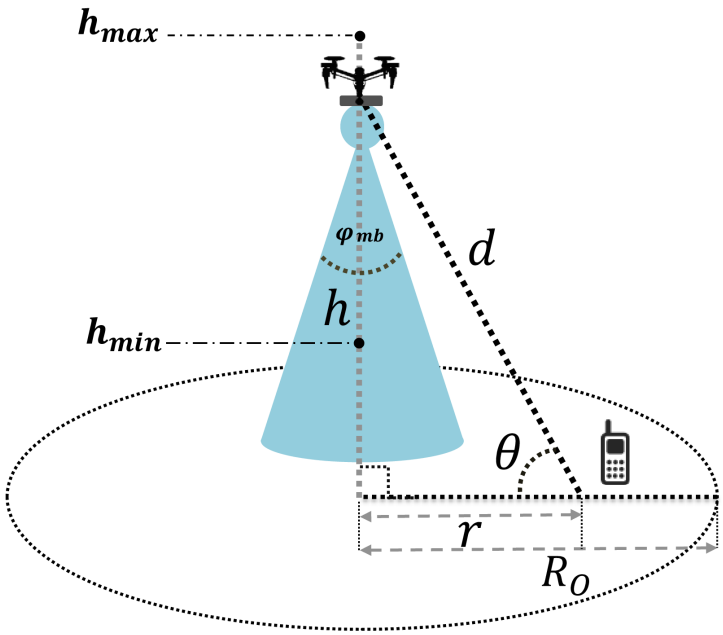

FIGURE 3.1: Drone small cell.

3.2.2 Drone to MU Link Budget

Consider the link between the drone (i.e., BS) and any MU (i.e., the receiver). The total link budget is expressed in terms of the received signal to noise ratio $\gamma(h, \theta)$ at the receiver antenna and assuming raised cosine pulses with a unity roll-off factor, and it can be written as [79]:

$$\gamma(h, \theta) = SNR = \frac{|g|^2 \, E_s \, G(\theta, \phi_{mb}) \, L(h, \theta)}{N_o}, \tag{3.1}$$

where g is the multi-path fading parameter with $|g|^2 \sim \exp(1)$, E_s is the transmitted symbol energy, N_o is the noise power spectral density of the zero mean complex additive white Gaussian noise (AWGN), $L(h, \theta)$ is the height and elevation angle dependent path-loss and $G(\theta, \phi_{mb})$ is the effective transmitter antenna gain as seen by the MU, parametrized in terms of MU elevation angle

and antenna main lobe beam-width, respectively. Furthermore, for simplicity and without loss of generality we assume a quasi-static Rayleigh fading channel and so the probability density function (PDF) of $\gamma(h,\theta)$ follows an exponential distribution $f_{\gamma(h,\theta)}(\gamma(h,\theta)) = \frac{1}{\bar{\gamma}(h,\theta)} \exp\left(-\frac{\gamma(h,\theta)}{\bar{\gamma}(h,\theta)}\right)$. As previously mentioned, the sectorized antenna gain function will be as follows [77]:

$$G(\theta,\phi_{mb}) = \begin{cases} A_{dB}, & \text{if } \theta > \pi/2 - \phi_{mb}/2 \\ B_{dB} = -A_{dB}, & \text{if } \theta \leqslant \pi/2 - \phi_{mb}/2. \end{cases} \tag{3.2}$$

where A_{dB} and B_{dB} are the effective antenna gains for the main and side lobes, respectively. Here, due to a limitation on the antenna patterns available, the antenna main lobe beam-width is constrained to three values (i.e., $\pi/20$, $\pi/6$ and $\pi/2$) and as result of this constraint A_{dB} is also constrained to $A_{dB} = \{15, 10, 3\}$ dB, respectively. The reason for this is to ensure an average (linear) unity gain with respect to θ. It is important to note however, that increasing the altitude of the drone will mean that more MUs will effectively see the antenna gain of the main lobe, but, the free space path-loss will increase. Note, that we will aslo use the antenna pattern from 3GPP standards which is [68]:

$$G(\theta,\phi_{mb}) = -\min\left(12\left(\frac{\theta}{\theta_{mb}}\right)^2, A_{dB}\right), \tag{3.3}$$

where A_{dB} and θ_{mb} here have a typical values of 20 dB and $\pi/18$, respectively. As we will show in the results section, the same optimal altitude exists for both of the considered antenna gain patterns. Note however, that there is a trade-off in selecting a specific θ_{mb}. That is, the architect of the network should take into account that the antenna main beam-width angle has to cover almost the entire coverage area for that specific optimal altitude. In fact, this is to

gain a better performance due to the reception of higher average power at the MU antenna. But unfortunately, other similar co-channel DSCs or underlay cellular cells may exist. Thus, they may suffer from higher interference due to such an antenna gain of the main beam-width.

Furthermore, to study the effect of the path-loss in DSCs it is important to adopt non-traditional models for both the up-link and the down-link communication paths, and in this context we follow the model derived in [6]. Thus, $L(h,\theta)$ in (3.1) will be modified and replaced by $\bar{L}(h,\theta)$ in (3.7) to take into account the probability of line of sight with the DSC BS. Thus for (3.7) we can write:

$$L_i(h,\theta)_{dB} = 10\log_{10}\left(K_i\left(\frac{h}{\sin(\theta)}\right)^{\delta}\right), \tag{3.4}$$

where $K_i = \zeta_i\left((4\pi f_{MHz})/c\right)^{\delta}$, and ζ_i is the excess path-loss for $i \in \{LoS, NLoS\}$ [6]. Furthermore, the probability of having a LoS link from the DSC and the desired MU follows the following formulas:

$$\mathcal{P}_{LoS}(\theta) = \frac{1}{1 + a_1\, \mathrm{e}^{-b_1 c_1\, \theta + b_1\, a_1}}, \tag{3.5}$$

$$\mathcal{P}_{NLoS}(\theta) = 1 - \mathcal{P}_{LoS}(\theta), \tag{3.6}$$

where a_1 and b_1 are environment-dependent constants and $c_1 = 180/\pi$. So, with (3.4) - (3.6) we can write the total average path-loss as follows:

$$\bar{L}(h,\theta) = \mathcal{P}_{LoS}(\theta)L_{LoS}(h,\theta) + \mathcal{P}_{NLoS}(\theta)L_{NLoS}(h,\theta). \tag{3.7}$$

Finally, from the above equations the total downlink budget as a func-

tion of the average SNR in (3.1) can be written as:

$$\bar{\gamma}(h,\theta) = \begin{cases} \frac{E_s\,\bar{L}(h,\theta)\,10^{\frac{A_{dB}}{10}}}{N_o}, & \text{if } \theta > \pi/2 - \phi_{mb}/2, \\ \frac{E_s\,\bar{L}(h,\theta)\,10^{\frac{B_{dB}}{10}}}{N_o}, & \text{if } \theta \leqslant \pi/2 - \phi_{mb}/2. \end{cases} \tag{3.8}$$

Now, by introducing the system model and with the above modelling parameters, we move to the analysis of the performance metrics in the following section.

3.3 Performance analysis

In this section we seek to derive an optimal value for the drone height (h) that will minimize certain performance metrics (e.g., average coverage probability, average bit error rate and coverage capacity). Note for a uniformly distributed users, the distance r in Figure 3.1 has a PDF:

$$f_r(r) = \frac{2r}{R_o^2}, \quad 0 \leq r \leq R_o, \tag{3.9}$$

and so the PDF of θ can easily be written after random variable transformation as:

$$f_\theta(\theta) = \frac{2h^2\cos(\theta)}{R_o^2\sin^3(\theta)}, \quad \tan^{-1}\left(h/R_o\right) \leq \theta \leq \pi/2. \tag{3.10}$$

3.3.1 Average Coverage Probability

Coverage probability $P_c(h)$ here is defined as the probability at which the SNR value is greater than a certain specified predefined threshold γ_{th}. Here, for a Rayleigh fading channel it follows that:

$$P_c(h,\theta) = \exp\left(-\frac{\gamma_{th}}{\bar{\gamma}(h,\theta)}\right). \tag{3.11}$$

Consequently, the average coverage probability over all the users inside the coverage area can be written as:

$$\begin{aligned}\bar{P}_c(h) &= \mathbb{E}_\theta\left[P_{out}(h,\theta)\right] \\ &= \mathbb{E}_\theta\left[\exp\left(-\frac{\gamma_{th}}{\bar{\gamma}(h,\theta)}\right)\right] \geq \bar{\rho}_c\end{aligned} \tag{3.12}$$

where $\bar{\rho}_c$ is the minimum coverage probability constraint. Now, by substituting (3.8) into (3.12), and after doing some manipulations, we can re-write the above equation as follows:

$$\begin{aligned}\bar{P}_c(h) = &\int_{tan^{-1}(h/R_o)}^{\pi/2-\phi_{mb}/2} \frac{2h^2\cos(\theta)}{R_o^2\sin^3(\theta)} \exp\left(-\frac{\gamma_{th}}{\bar{\gamma}(h,\theta)}\right) d\theta \\ &+ \int_{\pi/2-\phi_{mb}/2}^{\pi/2} \frac{2h^2\cos(\theta)}{R_o^2\sin^3(\theta)} \exp\left(-\frac{\gamma_{th}}{\bar{\gamma}(h,\theta)}\right) d\theta \\ = &\int_{tan^{-1}(h/R_o)}^{\pi/2-\phi_{mb}/2} \frac{2h^2\cos(\theta)}{R_o^2\sin^3(\theta)} \\ &\times \exp\left(-\frac{\gamma_{th}10^{\frac{-B_{dB}}{10}}\left(\frac{h}{sin(\theta)}\right)^\delta\left(e^{b_1(-c_1\theta+a_1)}a_1 K_{NLoS} + K_{LoS}\right)}{\frac{E_s}{N_o}\left(1+a_1 e^{b_1(-c_1\theta+a_1)}\right)}\right) d\theta \\ &+ \int_{\pi/2-\phi_{mb}/2}^{\pi/2} \frac{2h^2\cos(\theta)}{R_o^2\sin^3(\theta)}\end{aligned}$$

$$\times \exp\left(-\frac{\gamma_{th}10^{\frac{-A_{dB}}{10}}\left(\frac{h}{sin(\theta)}\right)^{\delta}\left(\mathrm{e}^{b_1(-c_1\theta+a_1)}a_1\,K_{NLoS}+K_{LoS}\right)}{\frac{E_s}{N_o}\left(1+a_1\,\mathrm{e}^{b_1(-c_1\theta+a_1)}\right)}\right)d\theta. \tag{3.13}$$

Thus, to find the optimum drone altitude (h_{opt}) we have to solve $\left(\frac{\partial \bar{P}_c(h)}{\partial h}=0\right)$ for h, where $h_{min} \leq h_{opt} \leq h_{max}$. As there is no closed-form solution exist; we will solve numerically and then verify with Monte Carlo simulations.

3.3.2 Average Bit Error Rate

Now, Average Bit Error Rate (ABER) is one of the well known performance measures of any communication system. Here, assuming M-ary phase shift keying (MPSK) and Gray bit-mapped constellations, the conditional error probability takes the form $P(e/\gamma) = a\,\mathrm{erfc}\left(\sqrt{b\gamma}\right)$, where $\mathrm{erfc}(x) = \frac{2}{\sqrt{\pi}}\int_x^{\infty}\exp(-x^2)dx$ is the complementary error function, a and b are modulation scheme Dependant constants (i.e., for BPSK: $a = 0.5$ and $b = 1$, and for QPSK: $a = 0.5$ and $b = 0.5$) [80]. Thus, assuming a Rayleigh fading channel the bit error rate at the desired MU receiver can be written as follows [81]:

$$P_e(h,\theta) = a\left(1-\sqrt{\frac{b\,\bar{\gamma}(h,\theta)}{b\,\bar{\gamma}(h,\theta)+1}}\right). \tag{3.14}$$

Consequently, the average bit error rate probability over the entire coverage area can be written as:

$$\begin{aligned}\bar{P}_e(h) &= \mathbb{E}_\theta\left[P_e(h,\theta)\right]\\ &= a\left(1-\mathbb{E}_\theta\left[\sqrt{b\,/(b+1/\bar{\gamma}(h,\theta))}\right]\right) \leq \bar{\rho}(e)\end{aligned} \tag{3.15}$$

where $\bar{\rho}(e)$ is the maximum average bit error rate constraint. Thus, by substituting (3.8) into the above equation, we can evaluate the average bit error rate probability for the desired coverage area.

3.3.3 Average Coverage Capacity.

Coupled with such drone assisted cells and the desired delay constrained applications such as voice and video streaming, the study of the coverage capacity performance metric for such networks is desirable. The coverage capacity here is defined as the average probability at which the channel capacity will be higher than a certain level such that the quality constraint cannot be achieved. Here, for a Rayleigh fading channel the coverage capacity for a certain threshold C_{th} Mbps is defined as follows:

$$\begin{aligned} P_{cov_C}(h,\theta) &= \Pr\left[W \log_2\left(1+\gamma(h,\theta)\right) \geq C_{th}\right] \\ &= \exp\left(-\frac{2^{C_{th}/W}-1}{\bar{\gamma}(h,\theta)}\right). \end{aligned} \tag{3.16}$$

where W is the channel bandwidth. Therefore, the average coverage capacity over the entire coverage area of the drone can be written as follows:

$$\begin{aligned} \bar{P}_{cov_C}(h) &= \mathbb{E}_\theta\left[P_{cov_C}(h,\theta)\right] \\ &= \mathbb{E}_\theta\left[\exp\left(-\frac{2^{C_{th}/W}-1}{\bar{\gamma}(h,\theta)}\right)\right]. \end{aligned} \tag{3.17}$$

So, by substituting (3.8) into the above equation, we can evaluate the average coverage capacity for the desired coverage area. Finally, we move to the discussion of these analytical results and verify them by Monte-Carlo simulations

TABLE 3.1: Simulation parameters.

Parameter	Value	Description
$\zeta_{LoS}, \zeta_{NLoS}$	1,20 dB	Excess path-loss
f_{MHz}	1800 MHz	Carrier frequency
δ	2	Path loss exponent
A_{dB}, B_{dB}	10,-10 dB	Antenna gain
ϕ_{mb}	$\pi/6$	Antenna beam width
θ_{mb}	$\pi/18$	3GPP Antenna beam width
a_1, b_1	$9.6, 0.28$	Environment dependent constants
W	20 Mhz	Channel bandwidth

in section 3.4.

3.4 Results and Discussion

In this section, we show numerical and simulation results for the DSCs deployment performance metrics, for the average coverage probability $\bar{P}_c(h)$, average bit error rate (ABER, $\bar{P}_e(h)$), and average coverage capacity ($\bar{P}_{cov_c}(h)$). Furthermore, we assume that the DSC is operating in an urban environment with the parameters shown in Table 3.1. Also, as described in the previous sections we consider a Rayleigh fading channel, and quadrature phase shift keying (QPSK) modulation scheme.

Figure 3.2 shows the drone altitude in meters vs. the average coverage probability for deployment with different cell radii. Here, we see that for a certain desired coverage area and antenna pattern there exists an optimum drone altitude at which the average coverage probability will be higher than at any other altitude. For example, for the coverage area with radius $R_o = 500$ m the optimum height of the drone will be around $h = 360$ m. Furthermore,

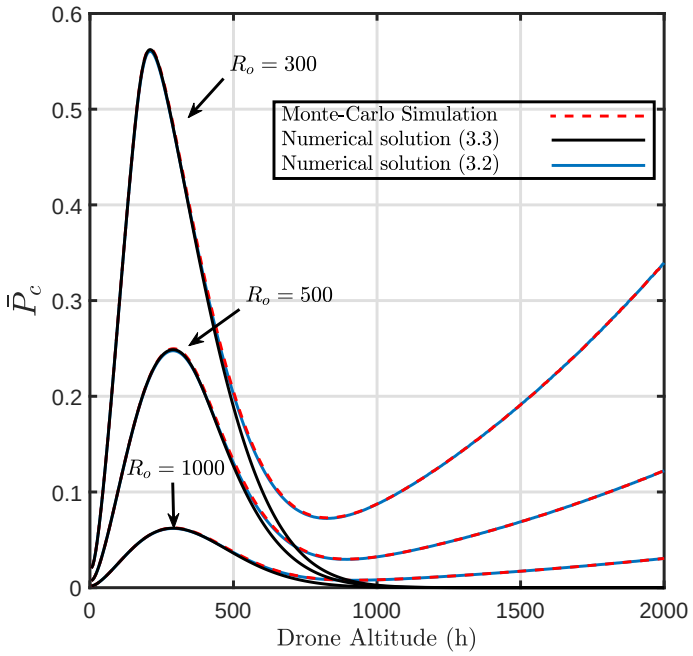

FIGURE 3.2: Drone altitude in meters vs. the average coverage probability for multiple cell radius deployment at $E_s/N_o = 65$ dB, $\phi_{mb} = \pi/18$ and $\gamma_{th} = -45$ dB .

we can notice that there is another optimum height which achieves better performance. As we can see in Figure 3.3, for $\phi_{mb} = \pi/6$ there is another higher $\bar{P}_c(h)$ around $h = 1200$ m. Undoubtedly, this is due to the antenna gain pattern that we adopted in (3.2), which means that much more coverage area will see more effective antenna gain as we increase the height of the drone. In fact, choosing the first maxima is more realistic because of the power constraint of the drone and the power consumption of climbing to this second optimal height. Adopting this antenna pattern is considered some how critical if compared with the 3GPP specification as indicated in (3.3). Finally, it is important to indicate that for any geometry deployment one has to take into account the limits of flying in terms of the minimum drone altitude (i.e., heights of buildings and obstructions) and the maximum range of the drone itself.

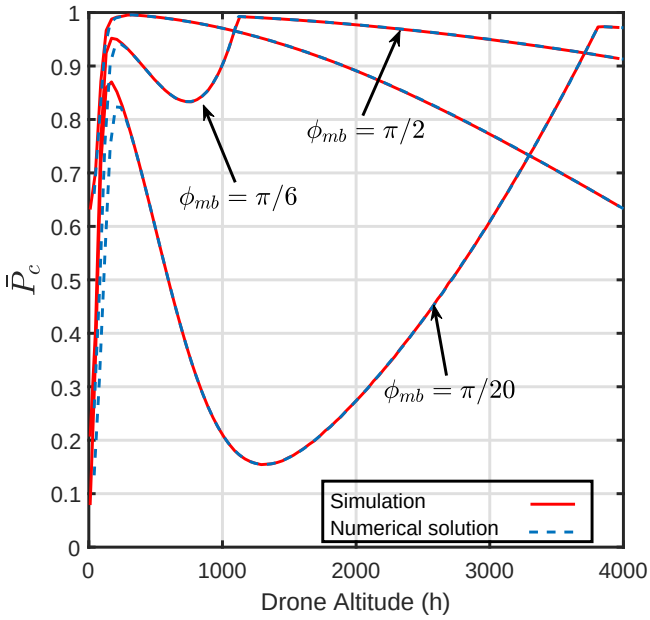

FIGURE 3.3: Drone altitude in meters vs. the coverage probability for multiple antenna gain patterns at $E_s/N_o = 65$ dB, $R_o = 300$ m and $\gamma_{th} = -45$ dB.

Figure 3.3 shows the drone altitude in meters vs. the average coverage probability for a fixed radius coverage area and multiple antenna beam widths. The results show that by increasing the beam width (i.e., higher spreading of effective gain on more elevation angles) then the average coverage probability will decrease. Likewise, we can notice that the optimal drone altitude is not affected by the antenna gain pattern. Note that with only one DSC, we can select the appropriate main beam width angle by selecting the one that achieves the best performance (i.e., by selecting $\phi_{mb} = \pi/2$). But, when considering the DSC in a field of multiple co-channel DSCs, we have to select the angle that achieves the best performance as well as the minimum interference between DSCs as we will show in the next chapter.

Figure 3.4 shows the signal to noise ratio (E_s/N_o) vs. the average coverage probability for multiple drone altitudes but with a fixed cell radius. Here, we can notice that as the drone altitude increases then the average coverage

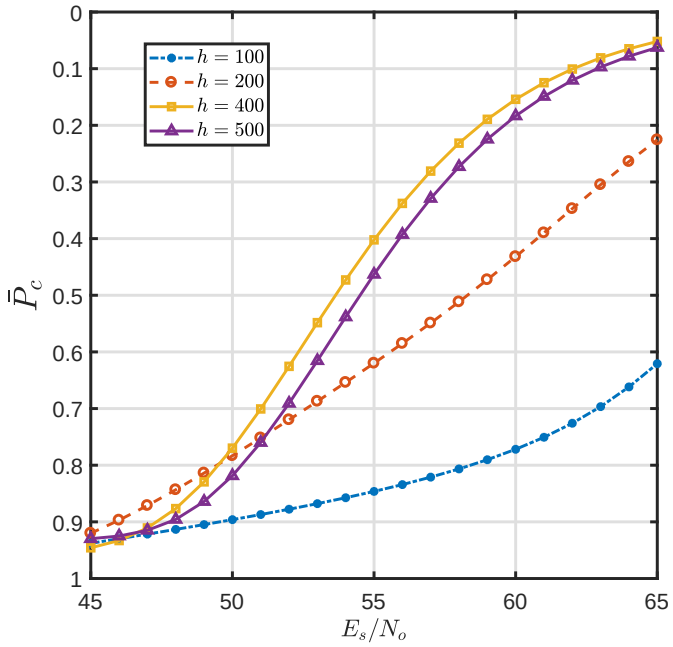

FIGURE 3.4: Signal to noise ratio (E_s/N_o) vs. the average coverage probability for multiple drone altitudes with fixed cell radius at $R_o = 500$ m, $\phi_{mb} = \pi/6$ and $\gamma_{th} = -45$ dB.

probability increase. This is up to a certain optimal height at which the coverage probability starts to decrease. Furthermore, Figure 3.5 also shows the signal to noise ratio (E_s/N_o) vs. average bit error rate for multiple drone altitudes. Here, we assume s QPSK modulation scheme in addition to the assumed Rayleigh fading channel. Specifically, at a certain point the behaviour is similar in both Figures 3.4 and 3.5. For example, for $h = 400$ m and $h = 500$ m, the deployment for $h = 500$ m outperforms that at $h = 400$ m. In conclusion, the same optimal drone altitude is valid to optimize the two performance metrics as well as for the coverage capacity.

Finally, Figure 3.6 shows the capacity threshold vs. the average coverage capacity for multiple drone altitudes with a fixed cell radius. We observe

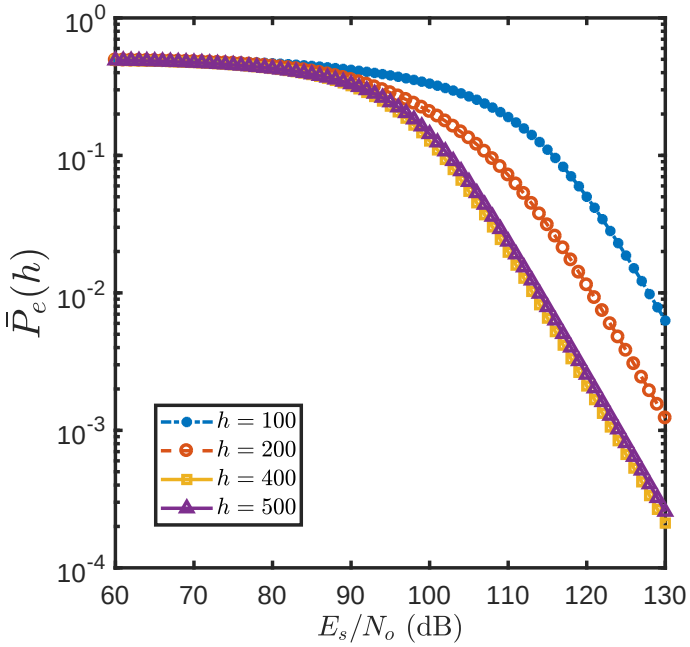

FIGURE 3.5: Signal to noise ratio (E_s/N_o) vs. average bit error rate for multiple drone altitudes with fixed cell radius $R_o = 500$ m and $\phi_{mb} = \pi/6$.

the same trend as with the previous metrics. The average coverage capacity follows the same optimal point for the drone altitude. To summarize, there are always many configurations at which the QoS constraint is achievable, and this concludes the advantage of reconfigurability of drone base cells as compared to the underlay cellular networks.

3.5 Conclusion

In this chapter, a deployment of a drone small cell served by low altitude platforms, known also as unmanned aerial vehicles, is studied. First, the down-link budget is examined and the antenna gain pattern with the proper path-loss models are enforced to accurately evaluate the SNR received at the

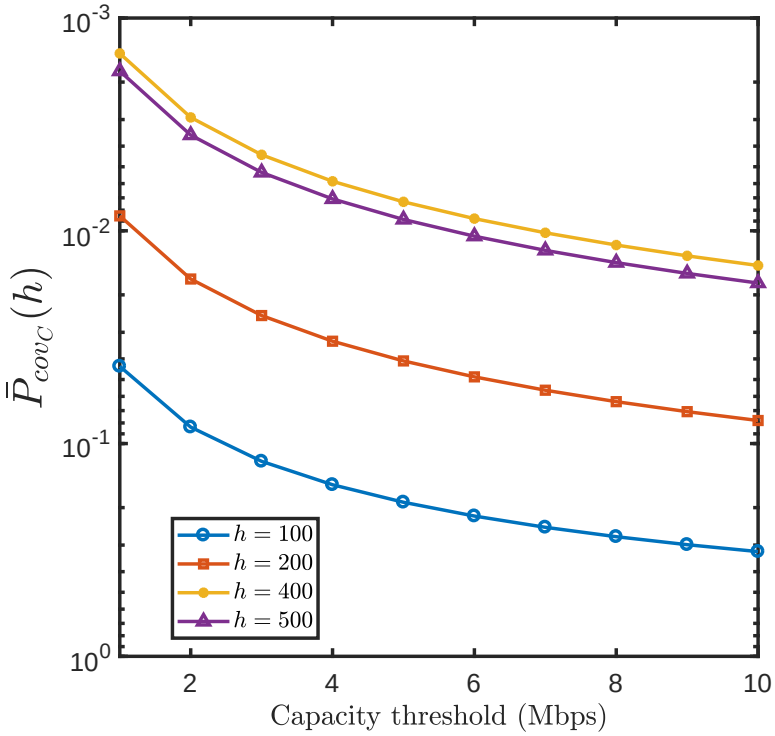

FIGURE 3.6: Capacity threshold vs. the average coverage capacity for multiple drone altitudes with fixed cell radius $R_o = 500$ m, $\phi_{mb} = \pi/6$ and $E_s/N_o = 50$ dB.

mobile terminal. Secondly, the performance metrics in the sense of coverage probability, error rate, and coverage capacity are studied to optimize the drone altitude that achieves the best performance. Furthermore, the numerical and simulation results show that there is an optimal drone height in the sense of averaging over all the MUs inside the entire desired coverage area.

To summarize, choosing the antenna pattern model is a critical issue. Hence, the use of the 3GPP specifications on antenna patterns is more practical, realistic and also an optimal altitude exists. Moreover, it is clear that the optimal altitude will change by changing the main-beam width angle if and only if the comparison between DSCs is carried out for only one MU. This is the same as changing the elevation angle of the MU which is directly related to the antenna intensity pattern. Also, another degree of freedom constraints

should be added in future, especially, the existence of the DSCs in a field of co-channel interferers and the effect of the total existing interference on the communication performance[1]. As a final remark, drone to drone relaying techniques, network architecture, interoperability with the underlay networks, routing and power efficiency are all open issues for research.

[1]This is the topic of the next chapter, where we show a more comprehensive performance analysis in the coexistence of co-channel interference and traditional cellular network.

Chapter 4

Drone-Based Finite Recovery Networks

Contents

In this chapter, we develop a more comprehensive framework for the design of drone empowered small cellular networks (DSCNs). In particular, we study the co-existence of drone small cells in a bounded area on the top of an operational ground cellular network in a post-disaster situation. We define and study the design parameters such as optimal altitude and number of drone BSs, etc., as a function of destroyed BSs, propagation conditions, etc. In order to address these design issues, we present a comprehensive statistical framework which is developed from a stochastic geometric perspective. We then employ the developed framework to investigate the impact of several parametric variations on the performance of the DSCNs. Without loss of any generality, in this chapter, the performance metric employed is coverage probability of a down-link mobile user. It is demonstrated that by intelligently selecting the number of drones and their corresponding altitudes, ground users coverage can be significantly enhanced. This is attained without incurring a significant performance penalty to the mobile users which continue to be served from operating ground infrastructure.

4.1 Introduction

In chapter 3, we studied the optimal dimensioning of DBS assisting in offloading the network capacity in a certain circular coverage area. To extend the framework for a wider coverage area and assuming multiple drones are required to off-load the area capacity shortfall, drone empowered small cellular networks (DSCNs) with multiple co-working drones present an attractive solution as they can be swiftly deployed for provisioning public safety networks. Despite the work in [12, 72–75, 78], the design and deployment of flying cells as a recovery network is not extensively investigated in the literature. So, in this chapter, by borrowing well-known tools from stochastic geometry, we will investigate the design space of flying cellular networks. We will also explore the co-existence properties of an overlaid DSCN with the operational part of the existing network.

4.1.1 Related Work

In the recent past [12, 72–75, 78] numerous studies have attempted to define the design space of the DSCNs from various different perspectives. Nevertheless, most of them either: (i) study a simple single-cell set up; (ii) do not account for intrinsic randomness in topology; (iii) abstract the coverage areas and interference via non-realistic models. The authors in [12] investigated drone small cells (DSCs) deployment to provision air-to-ground services. The authors consider a device-centric deployment approach and adopt modelling abstraction of circular discs for the coverage areas induced by DSCs. Moreover, they investigate the optimal DSC altitude which leads to a maximum

ground coverage and minimum required transmit power for a single DSC. Optimization for both: (i) distance between co-channel drones (i.e., drones sharing the same frequency) and (ii) the altitudes of co-channel drones was also performed. The study does not explore cross-tier interference management in the presence of large-scale DSCN deployment. The authors in [19], based on the results of [6], present a 3D optimization problem for DSCs with the aim to maximize the number of users to be covered by such DSCs using a numerical search algorithm to satisfy the defined quality of service (QoS) measures. The paper focuses on drone empowered future cellular networks for disaster recovery/ public safety. Nevertheless, the effect of cross network interference (i.e., interference between operational cellular infrastructure and DSCs in a post-disaster scenario) has not been addressed. To this end, we now present a holistic framework for characterizing the performance of an overlaid DSCN which is collocated with operational cellular infrastructure. We explicitly investigate the co-existence properties of both networks in the presence of cross-network interference. Moreover, we also demonstrate that the desired performance metric can be significantly enhanced via optimal control of drone altitude.

4.1.2 Contributions

The contribution and organization of this chapter are as follows:

1. The comprehensive spatial modelling of a drone-based public safety network is considered over a partially destroyed/offloaded cellular network. The impact of various parameters such as path-loss, number of DBSs, density of micro BSs (MBSs) and the altitude of the DBSs on both the

DSCN and the cellular network coverage has been investigated (see section 4.2).

2. Borrowing tools from stochastic geometry, we present a statistical framework for quantifying the performance of large-scale DSCNs deployment. The analytical framework is subsequently employed for design optimization.

3. The impact of the number of DBSs (and their height) on the coverage probability performance metric for both drone mobile users (DMUs) and micro mobile users (MMUs) (see section 4.3).

4. Finally, some critical design issues are explored and envisioned future developments are summarized (see section 4.5).

4.2 Network and Propagation Model

4.2.1 Deployment Geometry

Consider the down-link communication in a network formed by a DSCN overlaid on an existing cellular network. As illustrated in Figure 4.1, the disaster recovery network is established via deployment of a finite number of DBSs. The key objective is to complement the capacity of the operational cellular micro BSs serving the traffic originating from a coverage hole created due to the destruction of infrastructure. The number of drones required to meet the short-fall in coverage is strongly coupled with: (i) the probability (p^o) of destruction of an arbitrary MBS; and (ii) the radius R_r of the affected area (i.e., the disaster recovery area). As shown in Figure 4.1, it is assumed that in

a post-disaster scenario some of the MBSs are destroyed (illustrated as the red framed points). Consequently, N_d drones are deployed to cover the destroyed cells. However, the number of drones is not necessarily the same as the number of the destroyed cells. This is due to the limitation on the capacity of the DBSs as well as the difference in transmission power and radio prorogation conditions when compared to the MBSs. For the modelling of the spatial distribution of the overall wireless network, we borrow tools from stochastic geometry. To this end, it is assumed that N_d number of drones are uniformly distributed inside the two dimensional disc formed by the disaster recovery area. The overall network geometry is modelled with two collocated point process, the former is for the operational MBSs while the later is for the DBCN BSs, as follows:

1. **An inhomogeneous Poisson point process (IHPPP)**: Here we define the inhomogeneous Poisson point process, $\Phi_m = \{x_1, x_2, ..., x_N\} \subset \mathbb{R}^d$, as the superposition of two disjoint conditional PPPs: (i) a conditional PPP of density λ_1 such that $\Phi_1 = \{x_1, x_2, ..., x_N \in W \setminus \mathcal{B}(0, R_r)$[1]$\} \subset \mathbb{R}^d$ and (ii) a conditional PPP of points density λ_2 such that $\Phi_2 = \{x_1, x_2, ..., x_N \in \mathcal{B}(0, R_r)\} \subset \mathbb{R}^d$. Hence, the probability of finding $n = n_1 + n_2$ points (i.e, n_1 points from Φ_1 and n_2 points from Φ_2) inside disc of radius $R > R_r$ can be obtained as

$$\mathbb{P}(\Phi_m(\mathcal{B}(0, R)) = n = n_1 + n_2) = \prod_{i=1}^{2} \frac{(\lambda_i v(\mathcal{A}_i))^n}{n_i!} \exp\left(-\lambda_i v(\mathcal{A}_i)\right), \quad (4.1)$$

where λ_i is the density of the BSs per unit area of $\mathcal{A}_i$ (i.e., density of MBSs), $v(\mathcal{A}) = \int_{\mathcal{A}} dx$ is the Lebesgue measure [82]. In-particular, if the desired area is a ring with radii $A \leq r \leq B$, then $v(\mathcal{A}) = \pi(B^2 - A^2)$.

[1] $\mathcal{B}(0, R_r)$ denotes a ball of radius R_r centred at origin.

2. **Binomial point process (BPP)**: While the IHPPP formulation is adequate to model operational cellular network MBSs, the above equation cannot be employed for the DSCN formed inside the recovery area $\mathcal{B}(0, R_r)$. That is because that the specific number of drones N_d when uniformly distributed in this finite area, $\mathcal{B}(0, R_r)$, forms a binomial point process (BPP)[2] [59]. In particular, for a finite area of radius R_r in the N-dimensional space, the probability of having k transmitting interferers (i.e., co-channel drones) at the origin (i.e., the interference at $\mathcal{B}(0, 0)$) from the ring-shaped area $\mathcal{B}(0 \leq A < B \leq R_r)$ with, respectively, an inner and outer radius A and B inside $\mathcal{B}(0, R_r)$ can be evaluated as follows

$$\mathbb{P}(\Phi(\mathcal{B}(0 \leq A < B \leq R_r)) = k) = \binom{N_d}{k} \left(\frac{B^N - A^N}{R_r^N} \right)^k \left(1 - \frac{B^N - A^N}{R_r^N} \right)^{N_d - k}. \tag{4.2}$$

In summary, the spatial distribution of DSCs is captured using a BPP, while co-existing cellular network is modelled via a thinned IHPPP as described above.

[2]The spatial distribution of the drones is their projection onto the two-dimensional coverage region. This, can be obtained by angular transformation of the geographical three-dimensional distribution of the DBCN.

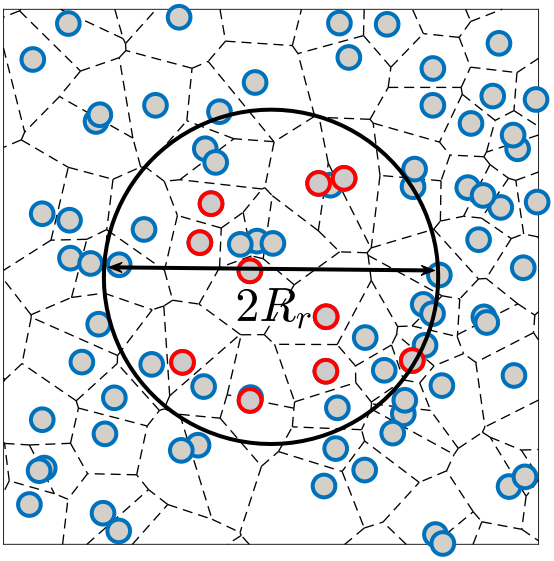

FIGURE 4.1: One realization of the proposed network model. The black large circle represents the recovery area of a radius R_r to be covered by drones (on the top of the existing cellular network). The small blue circles represents the MBSs. The red circles represent the destroyed BSs (any BS inside the circle destroyed with probability $p^o = 0.4$).

4.2.2 Propagation Model

Path Loss Model

In order to accurately capture the propagation conditions in a DSCN, we again employ the same path-loss that we used in chapter 3 with a path-loss model presented in [12] which is derived from practical measurements. The employed path-loss model adequately captures LoS and NLoS contributions for drone-to-ground communication as follows:

$$L_{LoS}(h,r) = \frac{\left(r^2+h^2\right)^{-1}}{K_{LoS}}, \tag{4.3}$$

$$L_{NLoS}(h,r) = \frac{\left(r^2+h^2\right)^{-1}}{K_{NLoS}}, \tag{4.4}$$

where again K_{LoS} and K_{NLoS} are environment and frequency dependent parameters such that $K_i = \zeta_i \left(c/(4\pi f_{MHz})\right)^{-\alpha}$, ζ_i is the excess path-loss for $i \in \{LoS, NLoS\}$ and α is the path-loss exponent which is equal to 2 as can be found in the literature of drone-based small cell applications. This propagation model categorizes the path-loss exponent or the excess path-loss into two groups depending on the probability of being in line of sight or not, whereas the majority on the literature categorizes into dual slope with regards to a threshold distance at which the slope of path-loss curve switches to a different value. Furthermore, the probability of having a LoS link from the DSC and the desired mobile user (MU) is as follows:

$$\mathcal{P}_{LoS}(\theta) = \frac{1}{1 + a_1 \, \mathrm{e}^{-b_1 c_1 \, \theta + b_1 \, a_1}}, \tag{4.5a}$$

$$\mathcal{P}_{NLoS}(\theta) = 1 - \mathcal{P}_{LoS}(\theta), \tag{4.5b}$$

where a_1, b_1 and c_1 are environment dependent constants, $c_1 = 180/\pi$. Consequently, the total average excess path-loss can be characterized as

$$\bar{\kappa}(\theta) = K_{LoS} + \frac{K_\Delta}{1 + a_1 \, \mathrm{e}^{-b_1 c_1 \, \theta + b_1 \, a_1}}, \tag{4.6a}$$

$$\bar{\kappa}(r) = K_{LoS} + \frac{K_\Delta}{1 + a_1 \, \mathrm{e}^{-b_1 c_1 \, \tan^{-1}(\frac{h}{r}) + b_1 \, a_1}}, \tag{4.6b}$$

where $K_\Delta = K_{LoS} - K_{NLoS}$, and $r = h/\tan(\theta)$. Note that, the average path-loss from the DBS to the desired MU can be quantified from the above equations as

$$\bar{L}_d(r) = \frac{(r^2 + h^2)^{-1}}{\bar{\kappa}(r)}. \tag{4.7}$$

The large-scale path-loss for the down-link of the cellular network is modelled by the well-known power law path-loss function

$$L_m(r) = \frac{r^{-\alpha}}{K}, \tag{4.8}$$

where α, the path-loss exponent has typical values for small/micro cells between 2 and 4. K is the excess path-loss and has typical values between 100 dB and 150 dB (see table 2.1 on page 45 and [68, 69] for details). The power law path-loss is widely adopted in literature for analysis of large-scale cellular networks[3].

Small-Scale Fading

It is assumed that large-scale path-loss is complemented with small-scale Rayleigh fading such that $|g|^2 \sim \text{Exp}(1)$. Also, it is assumed that the network is operating in an interference limited regime, i.e., performance of all links is dependent upon co-channel interference and thermal noise at the receiver front-end is negligible.

4.3 Coverage Probability

In order to characterize the link level performance of DSCN, we employ coverage probability as a metric. The coverage probability of an arbitrary user is

[3] An alternative general formula for the path-loss is $L(r) = \frac{1}{K(\epsilon + r^{\alpha})}$. This formula is widely used to mitigate the singularity at $r = 0$ and the divergence of the Laplace functional of aggregate interference with path-loss exponent equal to or less than $\alpha \leq 2$. Here, ϵ is defined as the minimum distance between the transmitter and the receiver. This is implicitly incorporated for drone-based communication with $\epsilon = h^2$ [83].

defined as the probability at which the received SIR is larger than a pre-defined threshold, β.

4.3.1 Link Distance Analysis

Coverage probability for the MU is strongly dependent upon link distance to the nearest neighbour serving BS since we assume a nearest neighbour association. Consequently, the conditional coverage probability as will be derived in the next sub-sections must be averaged over the random link distance. To this end, in this sub-section we characterize the distribution of the link distance: (i) between DBS and its corresponding DMU and (ii) the MBS and its down-link MMU.

Distance between DMU and DBS

Since DBSs are uniformly distributed in the disaster area, the distance between a DMU at the origin and the DBS can be quantified from the void probability of a BPP as follows [63]:

$$f_{R_1}(r_1) = \frac{2N_d}{r_1}\left(1-\left(\frac{r_1}{R_{r_1}}\right)^2\right)^{N_d-1}\left(\frac{r_1}{R_{r_1}}\right)^2. \tag{4.9}$$

In the next chapter, we will extend this distribution to a more generalized case where the drone and the MU are located at a distance from the coverage area centre and the nearest neighbour distance distribution will be conditional to the location of the drone.

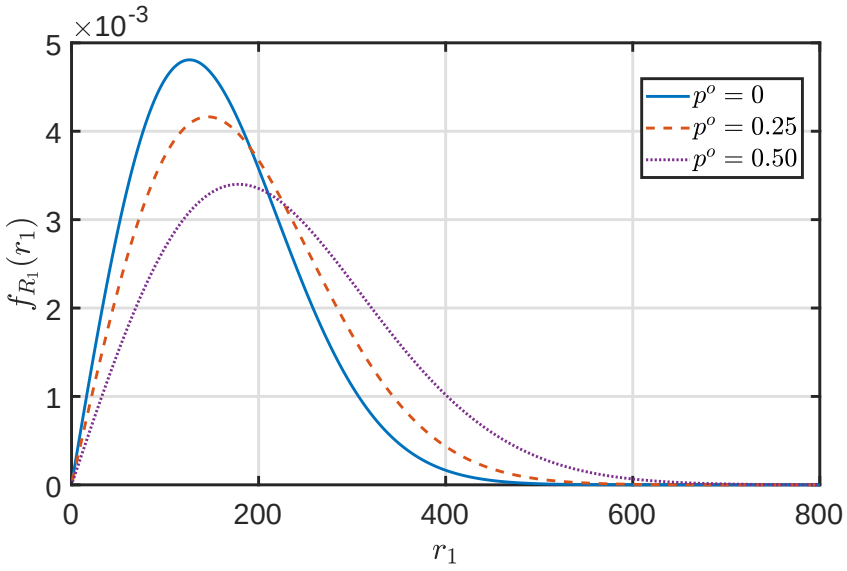

FIGURE 4.2: Probability density function for the nearest neighbour distance $f_{R_1}(r_1)$ vs. the distance to the nearest neighbour. The recovery area has radius 2 km and $\lambda_1 = 10^{-5}$.

Distance between MMU and serving MBS

From a stochastic geometry analysis for homogeneous PPP with a density λ, it is well known that the distance PDF of the nearest node can be written as $f_{R_1}(r_1) = 2\pi r_1 \lambda e^{-\pi r_1^2 \lambda}$ [61]. Hence, the cumulative density function (CDF) for the nearest neighbour can be written as $F_{R_1}(r_1) = 1 - e^{-\pi r_1^2 \lambda}$. In the case of the post-disaster operational cellular network, the stationary PPP assumption does not hold. As highlighted before, the MBSs form an IHPPP for which the link distance distribution has not been explored in the existing literature. Consequently, in the following proposition, we present an expression for the PDF of the distance between the MBS and its corresponding MMU.

Proposition 4.1

The PDF of the distance between the MMU at the center of the recovery area and the nearest MBS can be written as follows:

$$f_{R_1}(r_1) = \exp(-\pi\lambda_2 R_r^2)(2\pi\lambda_1 r_1 \exp(-\pi\lambda_1(r_1^2 - R_r^2))) + (1 - \exp(-\pi\lambda_2 R_r^2))(2\pi\lambda_2 r_1 e^{-\pi r_1^2 \lambda_2}). \quad (4.10)$$

Proof. We assume that the resulting IHPPP is the superposition of two conditioned PPPs (i.e., the first with nodes density λ_2 (with any node $x_{\{2,i\}} \in \mathcal{B}(0, R_r)$) and the second with density λ_1 (with any node $x_{\{1,i\}} \in W \backslash \mathcal{B}(0, R_r)$)). Furthermore, the MMU is only connected to a MBS outside the recovery area, if and only if, there are no operational BSs inside the recovery area. In other words, this is when the recovery area acts as a hole with radius R_r. Thus, the probability that the distance to the nearest neighbour MBS, R_1, is greater than R_r can be quantified as follows:

$$\begin{aligned} F_{R_1}^{(1)}(r_1) &= 1 - \Pr(R_1 \geqslant r_1), \\ &= 1 - \Pr(\text{Number of points of } \Phi_1 \\ &\qquad \text{inside the set } \{\mathcal{B}(0, r_1) \setminus \mathcal{B}(0, R_r)\} = 0), \\ &= 1 - \exp(-\pi\lambda_1(r_1^2 - R_r^2)). \end{aligned} \quad (4.11)$$

Next, by differentiating the expression in (4.11) the PDF can be obtained as

$$f_{R_1}^{(1)}(r_1) = 2\pi\lambda_1 r_1 \exp(-\pi\lambda_1(r_1^2 - R_r^2)). \quad (4.12)$$

Then, we average the nearest neighbour CDFs of the hypothetical Φ_1 and Φ_2 over the void probability of Φ_2 to obtain the average CDF of the nearest

neighbour distance to the MMU as

$$\begin{aligned} F_{R_1}(r_1) &= v_2^o F_{R_1}^{(1)}(r_1) + (1 - v_2^o) F_{R_1}^{(2)}(r_1), \\ &= \exp(-\pi\lambda_2 R_r^2)(1 - \exp(-\pi\lambda_1(r_1^2 - R_r^2))) \\ &+ \ (1 - \exp(-\pi\lambda_2 R_r^2))(1 - \exp\left(-\pi r_1^2 \lambda_2\right), \end{aligned} \tag{4.13}$$

where v_2^o is the void probability of the PPP with density λ_2 which models the nodes inside the recovery area. Thus by simply differentiating $F_{R_1}(r_1)$ in (4.13) we can write (4.10). □

Figure 4.2 depicts the PDF of the distance between the MBS and its down-link MMU. As is clear from the figure the average distance between the MMU and the MBS increases with the increase in the destruction probability. For instance, the average nearest neighbour distance in the original network is about 120 m while it increases to 190 m when $p^o = 0.5$.

4.3.2 Coverage Probability of a Stand-Alone DSCN

In order to perform comparative analysis, we first quantify the performance of a stand-alone DSCN, (i.e., in the absence of any cellular network). Without any loss of generality, we focus on the MU located at the centre of the disaster recovery area as it is the largest distant MU from any MBS (i.e., worst MU with regards to average received power) and has the worst interference conditions (i.e., largest aggregate interference power) [84]. We also assume that N_c channels are assigned to the N_d DBSs to serve the traffic originating from the disaster recovery area. The received SIR at the DMU can be quantified as

$$SIR^{(d)} = \frac{|g|^2 \ P_d \bar{L}_d(r_1)}{I^d_{\Phi_d}}, \tag{4.14}$$

where P_d is the transmit power employed by the DBS and $I^d_{\Phi_d}$ is the aggregate interference from the co-channel transmitting DBSs experienced by the MU and can be written as

$$I^d_{\Phi_d} = \sum_{i \in \Phi_d \setminus \{0\}} |g_i|^2 \, P_d \bar{L}(r_i), \tag{4.15}$$

where Φ_d is the set of all co-channel active DBSs. Consequently, the coverage probability for a DMU is given as

$$\begin{aligned} P_c^{(d)} &= \Pr\{SIR^{(d)} > \beta\}, \\ &= \Pr\left\{ |g|^2 \ > \frac{I^d_{\Phi_d}\beta}{P_d \frac{\left(r_1^2+h^2\right)^{-1}}{\bar{\kappa}(r_1)}} \right\}, \\ &= \mathbb{E}_{r_1}\left[\mathbb{E}_{I^d_{\Phi_d}}\left[\exp\left(-\frac{I^d_{\Phi_d}\beta}{P_d \frac{\left(r_1^2+h^2\right)^{-1}}{\bar{\kappa}(r_1)}} \right) \right] \right], \\ &= \mathbb{E}_{r_1}\left[\mathcal{L}_{I^d_{\Phi_d}}(s_1) \right] \end{aligned} \tag{4.16}$$

where $s_1 = \beta\bar{\kappa}(r_1)/(P_d\left(r_1^2+h^2\right)^{-1})$, $\mathcal{L}_{I^d_{\Phi_d}}(s_1)$ is the Laplace transform of the aggregate interference and this can be evaluated as in (4.17), where N_c is the number of channels available and $\left\lceil \frac{N_d}{N_c} \right\rceil$ is to assure that the total number of the remaining co-working nodes is an integer number [59].

$$\mathcal{L}_{I^d_{\Phi_d}}(s) = \left(1 - \frac{1}{R_r^2} \int_{r_1}^{R_r} \mathbb{E}_g \left[\left(1 - \exp\left(-\frac{s\,|g|^2 P_d}{(h^2+t^2)\bar{\kappa}(t)} \right) \right) 2\ t \right] dt \right)^{\left\lceil \frac{N_d}{N_c} \right\rceil - 1},$$

$$= \left(1 - \int_{r_1}^{R_r} \frac{2tsP_d}{R_r^2\left(\bar{\kappa}(t)h^2 + \bar{\kappa}(t)\,t^2 + sP_m\right)}dt\right)^{\left\lceil \frac{N_d}{N_c} \right\rceil - 1}. \tag{4.17}$$

4.3.3 Coverage Analysis of co-existing DSCN and Cellular Network

We now characterize the coverage probability of the DSCN operating in the presence of a partially destroyed ground cellular network. As highlighted before, we assume that ground BSs are destroyed with a certain probability p^o within a circular disaster-affected area. In practice, the shape of the disaster recovery area can be arbitrary and the probability of destruction can be a function of a natural phenomenon. Also, destruction across various ground BSs will be correlated which can be catered for by redefining p^o. However, for the sake of generality and tractability we employ a baseline model where p^o is a uniform random variable independent from BS location. The post-disaster operational cellular network forms a IHPPP such that

$$\begin{aligned} \lambda(r) &= \lambda_2 \mathbb{1}(r \leq R_r) + \lambda_1 \mathbb{1}(r > R_r), \\ &= \begin{cases} \lambda_1, & r > R_r, \\ \lambda_2 = (1-p^o)\lambda_1, & r \leq R_r, \end{cases} \end{aligned} \tag{4.18}$$

where λ_1 and λ_2 are respectively the original and the retained PPP density of the cellular network before and after destruction. Here, we will quantify the overall coverage by studying: (i) the coverage probability for the DMU and (ii) the coverage probability for a MMU. To this end, the SIRs at the DMU and MMU can be respectively quantified as

$$SIR^{(d)} = \frac{|h_o|^2 \;\; P_d \bar{L}_d(r_1)}{I_{tot}^{(d)}}, \tag{4.19}$$

$$SIR^{(m)} = \frac{|h_o|^2 \ P_m L_m(r_1)}{I_{tot}^{(m)}}, \tag{4.20}$$

where P_d and P_m are the transmitted signal power from the DBS and MBS, respectively, $I_{tot}^{(d)} = I_{\Phi_d}^d + I_{\Phi_m}^d$ and $I_{tot}^{(m)} = I_{\Phi_d}^m + I_{\Phi_m}^m$ are, respectively, the total aggregated co-channel interference seen by any down-link user located at the origin of the coverage area, and can be written as follows

$$I_{\Phi_d}^d = \sum_{i \in \Phi_d \setminus \{0\}} |g_i|^2 \, P_d \bar{L}_d(r_i), \tag{4.21}$$

$$I_{\Phi_m}^d = \sum_{i \in \Phi_m} |g_i|^2 \, P_m L_m(r_i), \tag{4.22}$$

$$I_{\Phi_m}^m = \sum_{i \in \Phi_m \setminus \{0\}} |g_i|^2 \, P_d \bar{L}_d(r_i), \tag{4.23}$$

$$I_{\Phi_d}^m = \sum_{i \in \Phi_d} |g_i|^2 \, P_m L_m(r_i). \tag{4.24}$$

Thus, the coverage probability, $P_c^{(d)}$, for any DMU in the coverage of a DBS can be written as follows:

$$\begin{aligned} P_c^{(d)} &= \Pr\{SIR^{(d)} > \beta\}, \\ &= \Pr\left\{ |g|^2 \ > \frac{I_{tot}^{(d)} \beta}{P_d \frac{r_1^{-2}}{\bar{\kappa}(r_1)}} \right\}, \\ &= \mathbb{E}_{r_1}\left[\mathbb{E}_{I_{\Phi_d}^d}\left[\exp\left(-\frac{I_{\Phi_d}^d \beta}{P_d \frac{r_1^{-2}}{\bar{\kappa}(r_1)}} \right) \right] \mathbb{E}_{I_{\Phi_m}^d}\left[\exp\left(-\frac{I_{\Phi_m}^d \beta}{P_d \frac{r_1^{-2}}{\bar{\kappa}(r_1)}} \right) \right] \right], \\ &= \mathbb{E}_r\left[\mathcal{L}_{I_{\Phi_d}^d}(s_1) \ \mathcal{L}_{I_{\Phi_m}^d}(s_1) \right]. \end{aligned} \tag{4.25}$$

Note here, that the Laplace transform of the total interference can be evaluated by simply applying the convolution property of Laplace transforms as $\mathcal{L}_{I_{tot}^{(d)}}(s) = \mathcal{L}_{I_{\Phi_d}^d}(s) \mathcal{L}_{I_{\Phi_m}^d}(s)$. Next, the coverage probability at the MMU can be

evaluated in the same way as in (4.25) as

$$\begin{aligned} P_c^{(m)} &= \Pr\{SIR^{(m)} > \beta\} = \Pr\left\{ \frac{|g|^2 \; P_m \frac{r_1^{-\alpha}}{K}}{I_{tot}^{(m)}} > \beta \right\}, \\ &= \mathbb{E}_{r_1}\left[\, \mathbb{E}_{I^m_{\Phi_m}} \left[\exp\left(-\frac{I^m_{\Phi_m} K\beta}{P_m r_1^{-\alpha}} \right) \right] \mathbb{E}_{I^m_{\Phi_d}} \left[\exp\left(-\frac{I^m_{\Phi_d} K\beta}{P_d r_1^{-\alpha}} \right) \right] \, \right], \\ &= \mathbb{E}_{r_1}\left[\mathcal{L}_{I^m_{\Phi_m}}(s_2) \; \mathcal{L}_{I^m_{\Phi_d}}(s_2) \right]. \end{aligned} \tag{4.26}$$

where $s_2 = K\beta/(P_m r_1^{-\alpha})$. In order to evaluate the Laplace transform of the aggregate interference for the MMUs, we can write the following:

$$\begin{aligned} \mathcal{L}_{I^m_{\Phi_m}}(s) &= \mathbb{E}(\exp(-sI_{\Phi_m})), \\ &= \mathbb{E}\left(\prod_{x_i \in \Phi_m} \mathbb{E}_G \left(\exp\left(-s \, |g|^2 \, L_m(r) \right) \right) \right), \end{aligned} \tag{4.27}$$

which can be solved using the generating functional of PPP as in [60, 66] such that

$$\mathcal{L}_{I^m_{\Phi_m}}(s) = \exp\left(- \underbrace{\int_{r_1}^{\infty} \left(1 - \mathbb{E}_G \left(-sP_m K \, |g|^2 \, L_m(r) \right) \right) \lambda(r) 2\pi r dr}_{A_1} \right). \tag{4.28}$$

Here, using the nodes density in (4.18), then A_1 in (4.28) can be written as

$$\begin{aligned} A_1 = {} & \frac{2\pi \, \lambda_2 {R_r}^2}{\alpha} {}_2\mathrm{F}_1(1, \frac{2}{\alpha}; \frac{\alpha+2}{\alpha}; -\frac{{R_r}^{\alpha}}{sKP_m}) \\ & - \frac{2\pi \, \lambda_2 {r_1}^2}{\alpha} {}_2\mathrm{F}_1(1, \frac{2}{\alpha}; \frac{\alpha+2}{\alpha}; -\frac{{r_1}^{\alpha}}{sKP_m}) \\ & + \frac{2sKP_m \pi \, \lambda_1 {R_r}^{2-\alpha}}{\alpha - 2} {}_2\mathrm{F}_1(1, \frac{\alpha-2}{\alpha}; 2\,\frac{\alpha-1}{\alpha}; -sKP_m {R_r}^{-\alpha}). \end{aligned}$$

TABLE 4.1: Simulation parameters.

Parameter	Value	Description
$\zeta_{LoS}, \zeta_{NLoS}$	1,20 dB	Excess path-loss
f_{MHz}	1800 MHz	Carrier frequency
α	4	Micro cell to ground Path-loss exponent
K	132 dB	Excess path-loss for micro cells
a_1, b_1	9.6, 0.28	Environment dependent constants
λ_1	1×10^{-5}	Base stations density
N_c	3	Available number of channels
P_d	1 dBW	Drone cell transmission power
P_m	10 dBW	Small BS cell transmission power

where ${}_2\mathrm{F}_1(a, b; c; d)$ is the Gauss Hyper-geometric function. One can solve this equation by change of variables, change of integral boundaries and finally using the identity $\int_0^u x^{\mu-1}/(1+\beta x)^v = \frac{u^\mu}{\mu}{}_2\mathrm{F}_1(\mu, v; 1+\mu; -\beta\, u)$ as in Eq.3.194.1-3 [65]. In particular, the expression in (4.28) can be written for $\alpha = 4$ as

$$A_1 = \frac{\pi\, sP_m\, \lambda_2}{2\sqrt{sP_m\, K}} \arctan\left(\frac{\sqrt{sP_m\, K}\, {R_r}^2}{sP_m}\right) - \frac{\pi\, sP_m\, \lambda_2}{2\sqrt{sP_m\, K}} \arctan\left(\frac{\sqrt{sP_m\, K}\, {r_1}^2}{sP_m}\right) + \frac{sP_m\, \pi\, \lambda_1}{\sqrt{sP_m\, K}} \arctan\left(\frac{\sqrt{sP_m\, K}}{{R_r}^2 K}\right).$$

4.4 Results and Discussion

In this section, we show numerical results for the coverage probabilities (P_c^d) and (P_c^m) of drone-based communication recovery network deployment. Furthermore, we assume that the DBCN is operating in an urban environment with the parameters shown in Table 4.1. Also, as described in the previous sections, we consider a Rayleigh fading wireless channel[4].

[4]The path-loss exponent for the drone to ground link (i.e., A2G link) is the same as the free space path-loss (i.e., $\alpha = 2$).

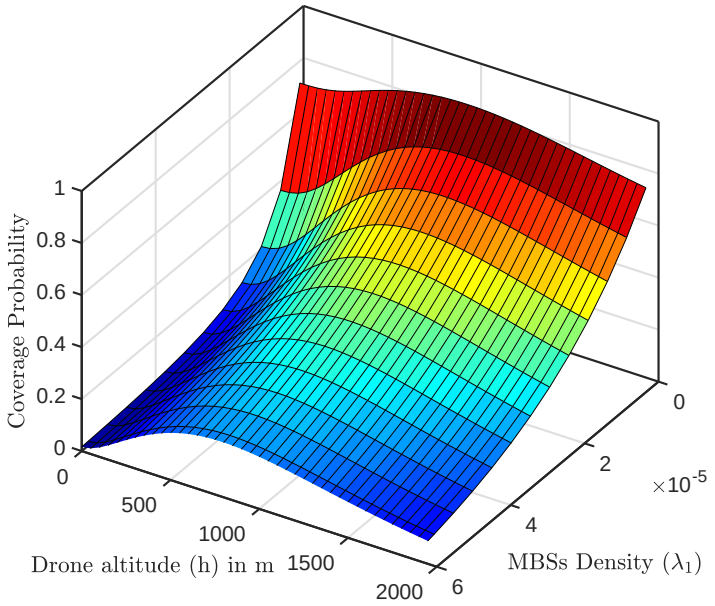

FIGURE 4.3: Coverage probability for a drone mobile user at the centre of the recovery area with both the DBSs and the MBSs sharing interference. The total available channels is 3. The destruction probability inside the recovery area is $p^o = 0.5$, with $\alpha = 4$, $R_r = 2$ km, $N_d = 6$, and $\beta = -3$ dB (see (4.25)).

Figure 4.3 shows the coverage probability for a DMU that is located at the centre of the recovery area (see (4.25)). The coverage probability is plotted against both the MBSs density (λ_1) and the DBSs altitude (h). An interesting observation here is that the drone-based recovery network can achieve a significant enhancement of the coverage probability when the MBS density is around a certain value. For example, with a MBS density equal to $\lambda_1 = 1 \times 10^{-5}$, a minimum coverage probability $P_c^{(d)} = 0.8$ can be obtained. That is, the deployment of drones as a recovery network can be utilized to the maximum for small/micro cells (i.e., with average micro cell radii between $200 < R_{avg} < 1000$ m). This is intuitively attributed to the fact that the interference which is seen by the DMU from the MBSs is lower as their density λ_1 is smaller.

Figure 4.4 shows the coverage probability of the DMU (see (4.25)).

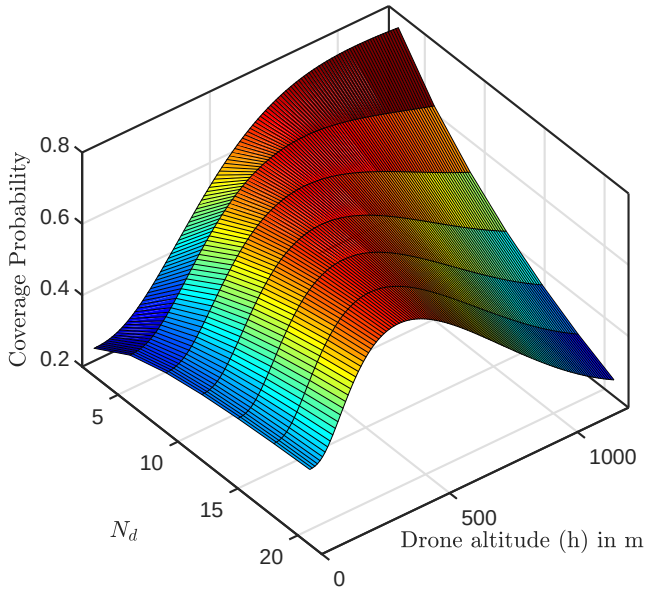

FIGURE 4.4: Coverage probability at the centre of the recovery area for drone mobile user with both the DBSs and the MBSs sharing interference. The total available channels is 3. The destruction probability inside the recovery area is $p^o = 0.5$. The MBS density of the original network $\lambda_1 = 1 \times 10^{-5}$, with $\alpha = 4$, $R_r = 3$ km and $\beta = -3$ dB (see (4.25)).

The coverage probability is plotted against N_d (the number of drones) and the drone altitude (h) in meters. As illustrated in Figure 4.4, it can be observed that with an increase in the number of DBSs the optimal altitude is reduced for the DBSs. Thus, altitude control gives a new degree of freedom to the optimal deployment of the DSCN. Generally, the the coverage probability values obtained with regard to the number of DBSs depends on two main factors: (i) the required total average network capacity, which intuitively increases as the number of DBSs increases and (ii) an increase in the number of channels deployed which translates into increases in the coverage probability.

Figure 4.5 shows the coverage probability for DMU vs. the drone altitude for multiple network configurations (see (4.25). Here, the solid lines

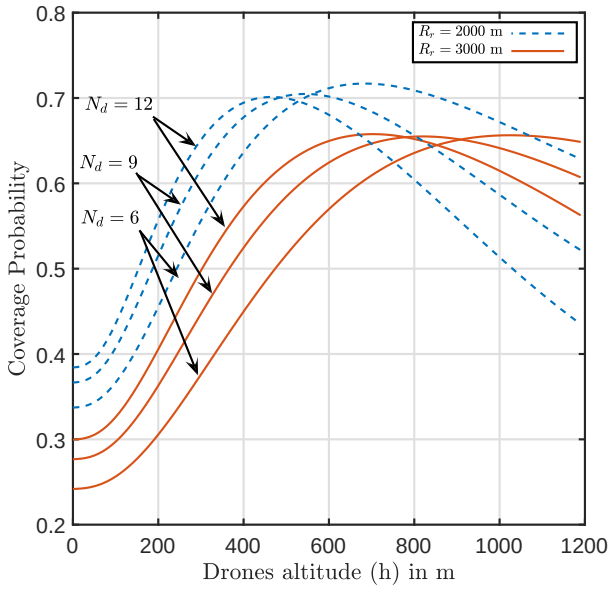

FIGURE 4.5: Coverage probability at the centre of the recovery area with both the DBSs and MBSs sharing in interference. The total available channels is 3. The destruction probability inside the recovery area is $p^o = 0.5$. The MBSs density of the original network $\lambda_1 = 1 \times 10^{-5}$. Path-loss exponent for the MBSs down-link is $\alpha = 4$, $R_r = 2$ km and $\beta = -3$ dB (see (4.25)).

correspond to the deployment geometry for a multiple number of drones for a disaster recovery area of radius $R_r = 2$ km while the dashed lines are for $R_r = 3$ km. The figure shows that the optimal drone altitude decreases as the number of drones increases. In turn, this corresponds to a decrease in interference experienced at the DMU. Also, an interesting observation is that a wider recovery area radius requires a higher drone altitude to maintain the same baseline coverage. Nevertheless, deploying DBSs at higher altitudes means that a smaller number of BSs are required to cover a wide recovery area. While this corresponds to a reduction in co-channel interference experienced at the DMU, this comes at the cost of reduced throughput. The down-link throughput of a MU increases with an increase in the number of DBSs due to aggregate load reduction on individual BSs.

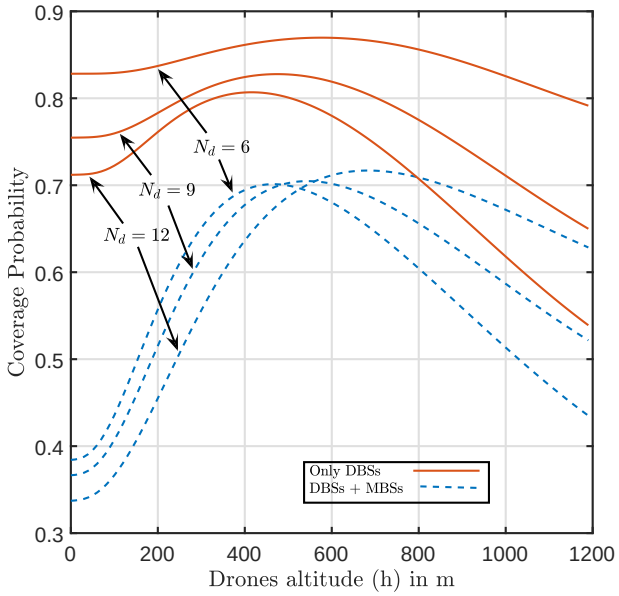

FIGURE 4.6: coverage probability at the centre of the recovery area with both the DBSs and MBSs. The total available channels is 3. The destruction probability inside the recovery area is $p^o = 0.5$. The MBSs density of the original network $\lambda_1 = 2 \times 10^{-5}$, $\alpha = 4$, $R_r = 2$ km and $\beta = -3$ dB (see (4.25) and (4.26)).

Figure 4.6 shows the coverage probability vs. drones altitude for the DMU for both: (i) the configurations when only DBSs are deployed (depicted with solid orange lines derived from (4.25)) and (ii) the configuration when the DBSs are overlaid on the operational cellular network (the dashed blue lines obtained from (4.25)). Here, we can observe two main trends: (i) good coverage can be achieved for the network deployment with only DBSs, and this can also be seen as allocating unique channels for the DBCN and (ii) there is a substantial need to search for the optimal altitude for the DBS, since the coverage probability dramatically decreases when an operational altitude other than the optimal altitude is selected.

Figure 4.7 shows the coverage probability of MMU vs. the drone altitude for multiple network configurations (see (4.26)). The dashed green

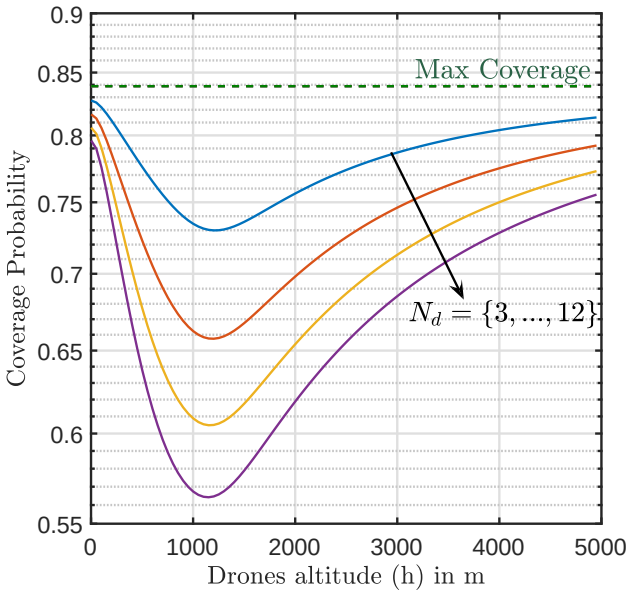

FIGURE 4.7: Coverage probability of MMU at the centre of the recovery area with both the DBSs and MBSs sharing in the interference. The total available channels is 3. The destruction probability inside the recovery area is $p^o = 0.5$. The MBSs density of the original network $\lambda_1 = 1 \times 10^{-5}$, $\alpha = 4$, $R_r = 2$ km and $\beta = -3$ dB (see (4.26)).

line shows the maximum achievable coverage of the MMU without the existence of the DSCN. Intuitively, this upper limit cannot be achieved in the presence of the DBSs, mainly due to non-zero co-channel interference which will be generated from the DBSs. For a recovery area with radius $R_r = 2$ km, the optimal drone altitude is lower than $h = 600$ m (see Figure 4.5). Consequently, for $N_d = 9$ DBSs the optimal network altitude is around 500 m, while the coverage probability for the MMU with the same deployment configuration of the DBCN is around 0.75 (i.e., this means that the ratio $((P_c^{(m)} - \text{Maximum Coverage})/\text{Maximum Coverage}) \times 100 = 90\%$) which is quite acceptable with the advantage of a higher achieved $P_c^{(d)}$. Consequently, a DSCN can be deployed by only optimizing the number of drones and their altitudes.

4.5 Conclusion

In this chapter, we developed a statistical framework for exploring the design space of a DSCN under realistic propagation conditions. The impact of co-channel inter and intra-network interference, when a DSCN is deployed to complement a capacity short-fall in disaster recovery scenario, has been explicitly accommodated in the model. In other words, the co-existence properties of finite and bounded overlaid DSCN networks are investigated. It is also shown that by optimizing the altitude of drone BSs (DBSs) and the number of drones the coverage probability of a ground user can be significantly enhanced in a post-disaster situation. Moreover, this can be accomplished at a minimum loss of performance incurred at a MMU that being served by an operational ground cellular network. Overall, coverage probability of ground users is significantly enhanced when DSCN is deployed and the network design is appropriately optimized.

Chapter 5

Drone Clustering over Cellular Network

Contents

In this chapter, we develop a comprehensive statistical framework to characterize and model large-scale unmanned aerial vehicle (UAV) enabled post-disaster recovery cellular networks. In the case of natural or man-made disasters, the cellular network is vulnerable to destruction resulting in coverage voids or coverage holes. Drone-based small cellular networks (DSCNs) can be rapidly deployed to fill such coverage voids. Due to capacity and back-hauling limitations on drone small cells (DSCs), each coverage hole requires a multitude of DSCs to meet the shortfall coverage at a desired quality-of-service (QoS). Moreover, ground users also tend to cluster in hot-spots in a post-disaster scenario. Motivated by this fact, in this chapter, we consider the clustered deployment of DSCs around the site of the destroyed BS. Accordingly, joint consideration of partially operating BSs and deployed DSCs yields a unique topology for such Public Safety (PS) networks. Hence, we propose a clustering mechanism that extends the traditional Matérn and Thomas cluster processes to a more general case where cluster size is dependent upon the size of the coverage hole. We then employ the newly developed framework to find closed-form expressions to quantify the coverage probability and the energy efficiency (EE) for the down-link mobile user. Finally, we explore several design parameters that address optimal deployment of the network (i.e., number of drones per cluster, drone altitudes and transmit power ratio between the traditional surviving BSs and the drone BSs).

5.1 Introduction

5.1.1 Motivation

In the last chapter, we studied the optimal dimensioning of DSCNs assuming the finite BPP distribution of DBSs in a small coverage area. However, due to capacity and back-hauling limitations on drone small cells (DSCs), each coverage hole requires a multitude of DSCs to meet the shortfall coverage at the desired quality-of-service (QoS). Also, for wider areas, where the capacity shortfall is needed in multiple areas, modelling the spatial distribution of drones by BPP is no longer valid. Hence, a wider comprehensive model to reflect the actual multi-coverage holes is required. Moreover, ground users also tend to cluster in hot-spots in a post-disaster scenario.

Despite several recent efforts [12, 22, 72, 74, 78], the design and deployment of flying cells as a disaster recovery network has not been extensively investigated in the literature. Again, the key difficulty is the absence of accurate models for post-disaster operational cellular infrastructure and user distribution. Nevertheless, some specific attributes of post-disaster systems such as surviving user clustering are well known in the existing literature [85]. These attributes can be accommodated in a stochastic geometric framework to provide system level understanding of DSCN empowered PS networks. To this end, we present cluster processes based on a stochastic geometric framework for exploring the design space of DSCNs. Noticing that the classical cluster processes do not cater for randomness in the cluster size (which is a key attribute of post-disaster cellular networks), we develop a novel Steinen cell [63, 86] based cluster process model. The model is employed to investi-

gate the design space of DSCNs and several important insights are presented. To the best of our knowledge, this is the first study to employ the proposed random clustering model to evaluate the design space for future DSCN deployments.

5.1.2 Related Work

The new structure of DSCNs leads to several new deployment topologies. For instance, cluster based fixed ground IoT networks have been addressed in [27][1]. In this study, an optimal clustering given the limited capacity for every UAV is investigated. Essentially, the optimal deployment of DSCNs is an application dependent problem. That is, for IoT and WSN applications, we need to define how many clusters we need to deploy while assuming that one UAV is only needed to serve each cluster. However, for a post-disaster scenario where a cellular BS is destroyed, demands for clustered users cannot be satisfied through a single UAV. The optimal network dimensioning considering the number of drones deployed per cluster thus becomes a design question. To this end, we will introduce the user-centric deployment geometry where each cluster is served by multiple UAVs. Our stochastic framework is built on following key attributes.

BS station destruction model: To model a post-disaster cellular network, we consider that BSs are independently destroyed with a certain probability. Thus, employing the widely used Poisson point process (PPP) model for the original cellular network implies that a post-disaster network can be modelled via a thinned point process. The independent thinning model for

[1]In chapter 7, we will study the performance of drone-assisted backscatter communications for an IoT sensor network.

post-disaster networks is widely adopted as in [12, 72, 74, 78]. Extension of this model to a scenario where BS destruction probability incorporates spatial correlation is more involved and may obscure some design insights. This aspect will be tackled in a future work.

Cluster based user and UAV deployment model: In order to model clustering between users in a post-disaster scenario, we extend the traditional Neyman-Scott cluster processes [62]. In [87–91] cluster processes have been employed to model user-centric heterogeneous cellular networks. In particular, Poisson cluster processes (PCP) such as the Matérn cluster process (MCP) and the Thomas cluster process (TCP) are employed to model locations of small cellular networks. Nevertheless, our analysis significantly differs from these existing works in two aspects; (i) in the existing literature, cluster processes which model small cellular networks are considered along with the PPP which models the underlying macro cellular network. However, in the context of disaster recovery networks the clusters are only created on dead spots (i.e., destroyed BSs). Consequently, this will result in a mixture model where (ii) the cluster size for a small cellular network is a design parameter. However, for a disaster recovery network, the cluster size is related to the coverage area of the desired destroyed cell site. Therefore, the cluster size itself is a random variable. These two factors are explicitly accommodated in our analysis. A mathematical analysis is presented in Section 5.3.

Cluster size model: As mentioned before, one of the key features of the resultant topology for a DSCN based PS network is that there exists a one-to-one mapping between the coverage area of the destroyed BS and the size of a cluster of UAV small cells deployed to meet the shortfall. Considering the strongest average received power based association cellular networks, asso-

ciation regions form a Voronoi tessellation. Consequently, for a post-disaster scenario, a Voronoi cell of a destroyed BS needs to be replaced with a cluster of UAVs. The cluster size is a function of the area of the Voronoi cell which itself is a random quantity. Also, the geometrical approximation of area for mapping is intricate. In this regards, [63, 86] have shown that the area of the Stienen cell (i.e., a circular inscribing-disc formed at the location of the destroyed BS with respect to its distance to the nearest neighbour) is an adequate proxy for the size of the Voronoi cell. Consequently, we consider clusters have random radii where the radius distribution corresponds to the Stienen cell [63, 86].

5.1.3 Contribution & Organization

To summarize, the key contributions and organization of this chapter are as follows:

1. We develop a comprehensive statistical model for quantifying the coverage, area spectral efficiency, and energy efficiency of DSCNs for post disaster recovery. To the best of our knowledge, the underlying topology yields a point process which has not been considered before even in the stochastic geometric literature.

2. Borrowing tools from stochastic geometry, we present a statistical framework for quantifying the performance of large-scale DSCNs deployment considering two types of cluster networks with different scenarios for the deployment geometry. Also, the analytical framework is subsequently employed for design optimization answering the following questions (see section 5.4):

(a) Is there an optimal cluster size to achieve an optimal coverage and throughput performance?

(b) Considering the optimal cluster size chosen, is there any optimal location for the drone small-cells and the number of drones in every cluster in a way to maximize the performance metrics?

(c) How does the variable cluster size change compared to fixing the size of all the clusters?

(d) How does changing the power ratios change the energy efficiency performance of the whole network? (see section 5.5).

3. Finally, some critical design issues are explored and possible future developments are summarized (see section 5.7).

5.2 Network and Propagation model

5.2.1 Deployment Geometry

Spatial Model for a Post-disaster Cellular Network

Similar to [52, 53, 87], we consider a large-scale macro-cellular network where the locations of the BSs are modelled by a homogeneous PPP (HPPP) (Φ) such that

$$\Phi = \{\mathbf{x_0}, \mathbf{x_1}, ..., \mathbf{x}_\infty, \forall\ \mathbf{x}_i \in \mathbb{R}^2\} \text{ with intensity } \lambda. \tag{5.1}$$

Coverage holes in post-disaster result from the destruction of the cellular infrastructure. These coverage holes are modelled by location independent thin-

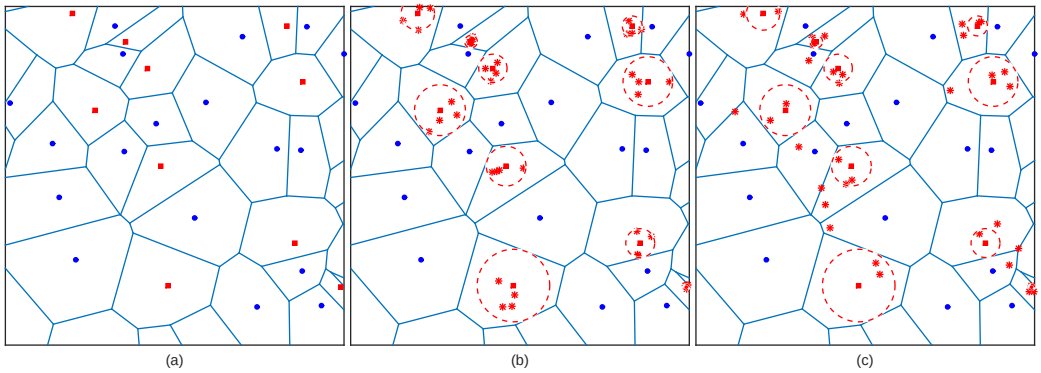

FIGURE 5.1: (a) Traditional cellular network where some MBSs are destroyed with probability $p^o = 0.3$. (b) Four DBSs are distributed uniformly in the two dimensional space around the centre of every destroyed MBS according to a MCP model as in (5.5). (c) Four DBSs are distributed normally in the two dimensional space around the centre of every destroyed MBS according to a TCP model as in (5.7). Blue circles, red squares and red stars are the retained MBSs, destroyed MBSs and the deployed DBS, respectively. A dashed circle is the radius of the deployment recovery area around the destroyed MBS.

ning of Φ with the probability of thinning represented by p^o [2]. Hence, the survived macro BSs (MBSs) will be modelled by a thinned HPPP [61] such that

$$\Phi_S = \{\mathbf{x} \in \Phi : \mathbb{1}(\mathbf{x}) = 1\} \text{ with intensity } \lambda_S = p_s\lambda, \tag{5.2}$$

where $\mathbb{1}(.)$ denotes a Bernoulli random variable[3]. Notice that the thinning process results in a new HPPP Φ_S which has intensity λ_S such that $\lambda_S = (1 - p^o)\lambda = p_s\lambda$, where p_s is the BS survival probability. Consequently, the HPPP of the destroyed BSs is given by

$$\Phi_D = \Phi \setminus \Phi_S, \tag{5.3}$$

[2]We adopted the uniform independent thinning for the sake of simplicity and the lack of any actual physical model for the destruction resulting from natural or man-made occurrences.

[3]Note that the Bernoulli random variable $\mathbb{1}(\mathbf{x})$ is independent of the location $\mathbf{x}$. However, $\mathbf{x}$ is only used as a location preserving parameter to preserve the original location of the holes.

which has an intensity of $\lambda_D = p^o\lambda$. The point process Φ_D, which preserves the number and the location of the holes, will then be used to model the location and number of points around which the DSCs are deployed to fill the coverage hole.

Network Model for DSCN

In order to fill the coverage holes after the thinning process, it is assumed that N_d DSCs, also called daughter points, are deployed as replacements for each destroyed BS in Φ_S. The key motivation behind deployment of multiple DBSs to fill the coverage hole created by a destroyed MBS pertains to the limitation on the capacity of the DBSs as well as the difference in transmission power and radio prorogation conditions as compared to the MBSs. Consequently, the resulting network geometry is modelled with two collocated point process, the former for the operational surviving MBSs (denoted by Φ_S) while the later is for the DBSs (denoted by Φ_D). The location of DSCs can be modelled by a general Neyman-Scott process [62]. This type of Poisson clustered process is formed by simply distributing a finite number of daughter points (N_d) around the parent point $\mathbf{x} \in \Phi_D$. The resulting point process is then the union of all the daughter points by preserving their locations around the parent points without including the parent points themselves. The union of all the DSCs in the space around the parent point process Φ_D (i.e., destroyed BSs) will form a clustered process which can be defined as

$$\Phi_C \stackrel{\Delta}{=} \bigcup_{i\in\{0,1,...,n-1\}} \{\Phi_{C_i} + \mathbf{x}_i\}, \forall\, \mathbf{x}_i \in \Phi_D, \tag{5.4}$$

where Φ_{C_i} is a cluster with N_d DSCs such that $\Phi_{C_i} = \{\mathbf{y_1}, ..., \mathbf{y}_{N_d}, \forall\ \mathbf{y}_i \in \mathbb{R}^2\}$, n is the number of the parent points in Φ_D and $\mathbf{x}_i$ is the location of the i^{th}

point in $\mathbb{R}^2$. Also, the clusters in Φ_C, without loss of generality, are divided into two sets of clusters: (i) the one called the representative cluster contains the set of all points around $\mathbf{x_0}$ (a typical destroyed BS) and is defined by $\Phi_{C_{in}} \triangleq \Phi_{C_0}$, and (ii) the set of all cluster process points except the points in the representative cluster which is defined by $\Phi_{C_{out}} \triangleq \Phi_C \setminus \Phi_{C_0}$.

Remark 5.1

We also denote $\Phi_{C_{\mathbf{x}}} = \Phi_{C_i}$ to denote the cluster around the parent point $\mathbf{x}_i \in \Phi_D$. Moreover, wherever M or T subscripts or superscripts appear, this means that the symbol is related to Matérn and Thomas cluster processes, respectively (as defined in subsequent discussion).

The distribution of the daughter points around the cluster centre defines the type of the cluster process (see Figure 5.1). Accordingly, we will study two types of cluster process where the DBSs are spatially distributed as follows:

1. **Matérn Cluster Process (MCP):** In a Matérn cluster process (MCP), a fixed number (N_d points) are distributed uniformly in the two dimensional space according to the density function

$$f^M(\mathbf{x}) = \frac{1}{\pi\sigma_M^2}, \quad \|\mathbf{x}\| \leq \sigma_M, \tag{5.5}$$

where σ_M is the radius of the cluster. Then, the PDF of the distance R from any point in the cluster to the parent point follows the uniform distribution

$$f_R^M(r) = \frac{2r}{\sigma_M^2}. \tag{5.6}$$

2. **Thomas Cluster Process (TCP):** In a Thomas cluster process the set

of cluster points (DBSs) are normally distributed in the two dimensional space $\mathbb{R}^2$ according to the density function

$$f^T(\mathbf{x}) = \frac{1}{2\pi\sigma_T^2} \exp\left(-\frac{\|\mathbf{x}\|^2}{2\sigma_T^2}\right), \tag{5.7}$$

where σ_T is the standard deviation and represents the scattering distance around the origin of the axis. Thus, the PDF of the distance R from any point in the cluster to the parent point follows the Rayleigh distribution[4]

$$f_R^T(r) = \frac{r}{\sigma_T^2} \exp\left(-\frac{r^2}{2\sigma_T^2}\right). \tag{5.8}$$

In this chapter, we assume that the typical drone mobile user (DMU) is located in the destruction zone and is always associated with the nearest DBS[5]. We also assume that, the probability of being associated to a MBS is very low since the distance to the nearest DBS is absolutely lower than the distance to the nearest MBS (i.e., the nearest DBS provides the highest average signal strength). Here, the assumption is accurate due to the adoption of cluster based distributions of the users and DBSs. Similarly, the authors in [88] show that this assumption is accurate even for the "maximum power association" scheme which is more sensitive for fading and network tier transmit power ratios. Clearly, the user is more likely to be served by its cluster centre if the distribution is more dense around the cluster centre. In our model, this is more likely to be accurate since we are using the nearest BS association. In addition, the large-scale model for the sky to ground channel is much favourable as regards providing line of sight links with higher received SIR at

[4]This follows from the joint transformation of $f_{X,Y}(x, y)$ to $f_{(R,\Theta)}(r, \theta)$ and then taking the marginal distribution of the distance R.

[5]With slight abuse of notations, we use DMU to denote to a typical user which is served by a flying drone BS.

the user antenna.

Remark 5.2 ▶ Spatial Model for DMUs

It is assumed that the distribution of the users around the centre of the clusters is the same as the DBSs with the same density. This follows from the fact that every DBS is associated to only one user in the same channel resource block. Hence, we map $\Phi_C \mapsto \Phi_C^{\mathrm{DMU}}$ for the set of the users around cluster centres with density $\lambda_C \mapsto N_d \lambda_C^{\mathrm{DMU}}$.

5.2.2 Propagation Model

Large-Scale Fading Model

In order to accurately capture the propagation conditions in a DSCN, we employ the path-loss model presented in the previous chapters. The employed path-loss model adequately captures line of sight (LoS) and non line of sight (NLoS) contributions for drone-to-ground communication as follows:

$$L_{LoS}(h,r) = K_{LoS}^{-1}\left(r^2+h^2\right)^{-\frac{\alpha}{2}}, \tag{5.9}$$

$$L_{NLoS}(h,r) = K_{NLoS}^{-1}\left(r^2+h^2\right)^{-\frac{\alpha}{2}}, \tag{5.10}$$

where h is the height of the drone in meters, r is the two dimensional projection separation between the drone and the DMU, K_{LoS} and K_{NLoS} are environment and frequency dependent parameters such that $K_i = \zeta_i \left(c/(4\pi f_{MHz})\right)^{-1}$, ζ_i is the excess path-loss for $i \in \{LoS, NLoS\}$ with typical values for urban areas ($\zeta_{LoS} = 1$ dB, $\zeta_{NLoS} = 20$ dB) and $\alpha = 2$ is the path-loss exponent for free space path-loss (see [12] for details). The probability of having a LoS link from

the DSC for the desired DMU is as follows:

$$\mathcal{P}_{LoS}(\theta) = \frac{1}{1 + a_1 \, \mathrm{e}^{-b_1 c_1 \, \theta + b_1 \, a_1}}, \tag{5.11a}$$

$$\mathcal{P}_{NLoS}(\theta) = 1 - \mathcal{P}_{LoS}(\theta), \tag{5.11b}$$

where a_1, b_1, c_1 are environment dependent constants, $c_1 = 180/\pi$ and θ is the elevation angle in degrees. Consequently, we define the total average excess path-loss as

$$\bar{\kappa}(r) = K_{NLoS} + \frac{K_{\Delta}}{1 + a_1 \, \mathrm{e}^{-b_1 c_1 \, \tan^{-1}(\frac{h}{r}) + b_1 \, a_1}}, \tag{5.12}$$

where $K_{\Delta} = K_{LoS} - K_{NLoS}$, and $r = h/\tan(\theta)$. Note that, the average path-loss from the DBS to the desired DMU can be quantified from the above equations as

$$\bar{l}_d(r) = \bar{\kappa}^{-1}(r)(r^2 + h^2)^{-1}. \tag{5.13}$$

The large-scale path-loss for the down-link of the cellular network is modelled by the well-known power law path-loss function

$$l_S(r) = K^{-1} r^{-\alpha}, \tag{5.14}$$

where α, the path-loss exponent, has typical values between 2 and 4. K is the excess path-loss and has typical values between 100 dB and 150 dB (see [68, 69] for details). This simple power law path-loss model is widely adopted in literature for analysis of large-scale cellular networks and has been used here to simplify the analysis as we are only studying the link for the

DSC associated DMU[6]. To conclude, the large-scale path-loss for the sky-to-ground channels is modelled by a single slope model with different values for the excess path-loss for the LoS and NLoS with path-loss exponent $\alpha = 2$. For the ground-to-ground channels we use a single model for both LoS and NLoS with the path-loss exponent $\alpha = 3.5$. This is due to the fact that the surviving BSs are all seen as interferers and are more likely to be in NLoS with the user which is assumed to be served by the nearest DBS.

Small-Scale Fading

It is assumed that large-scale path-loss for both of the traditional cellular-link and the DSCs is complemented with small-scale Rayleigh fading such that $|g|^2 \sim \text{Exp}(1)$. Also, it is assumed that the network is operating in an interference limited regime (i.e., performance of all links is dependent upon co-channel interference and thermal noise at the receiver front-end is negligible). The assumption of a Rayleigh fading model is due to simplicity of analysis. This assumption will not compromise our results, since Rayleigh fading implicitly gives a worst-case analysis of the Nakagami-m fading channel (e.g., where $m = 1$ no LoS component). However, the effect of LoS and NLoS components is incorporated into the large-scale fading model given by (5.12).

5.2.3 Transmission Model

In this chapter, we assume that the DMU is associated to nearest DBS (i.e., the BS which maximizes the average received signal to interference ratio (SIR)) and transmitters on the same frequency are considered as co-channel interfer-

[6]For a practical path-loss model for the cellular networks, chapter 6 will show a comprehensive performance analysis with higher-order statistics.

ers. These out-of-cell interferers can be classified into three categories: (i) the interference received from MBSs working on the same channel as the serving DBSs, (ii) the interference from the set of DBSs located inside the representative cluster and called "intra-cluster interferers", and (iii) the interferers from out of the representative cluster and called "inter-cluster interferers".

Remark 5.3

To complete the transmission model, we assume that the average number $\bar{N}_d$ of co-channel active DBSs inside any of the clusters has a Poisson distribution which is also related to the number of channel resources used (N_c) such that $\bar{N}_d = \frac{N_d}{N_c}$.

5.3 Distance distributions

In this section, we characterize link distance distributions which are required to quantify the large-scale path-loss given by (5.13). These distributions are employed to quantify coverage probability in section 5.4.

5.3.1 Distribution of the Radius of the Recovery Area

In order to tackle how to distribute the DSCs in the network we will study two types of cluster processes: (i) the traditional cluster process, where the standard deviation σ_i is fixed for all of the clusters and (ii) the modified Stienen's cell model. In the latter process, the standard deviation (i.e., the recovery cell radius) is considered to be the same as the radius of the Stienen's cell. This comes from the fact that the destroyed BSs will act as holes as defined in (5.3).

Here, the Stenien's cells are considered the most loaded cells and hence the circular modelling of the recovery area is a good approximation. Note, that for highly dense micro-cellular networks, as within cities, the approximation will be more accurate.

In the light of the above discussion, a good approximation of the recovery cell size can be built around the Steinen's model with cells of radius $\sigma_i \, \forall \, i \in \{M, T\}$. Thus, the distribution of the cluster spread in which the DBSs will be deployed is considered to be the distribution of the generalized Stienen's cell radius, i.e.,

$$f_{\sigma_i}(\sigma_i) = 2\pi\lambda\tau\sigma_i \exp\left(-\pi\lambda\tau^2\sigma_i^2\right), \forall i \in \{M, T\}. \tag{5.15}$$

Here, setting the value of $\tau = 2$ gives the distribution of the radius of the maximum inscribed circle, centred on the the destroyed MBS location and is equal to half of the distance to the nearest neighbour in the original tessellation which is well known as the Stienen's cell radius. Tunning the value of τ will tune the radius of the recovery area where the DBSs will be distributed.

5.3.2 Distance Distributions for MCP

We now consider the distance distributions assuming that DBSs and DMUs are uniformly distributed around the centres of the destroyed MBSs according to a MCP.

As shown in Figure 5.2, we consider a typical user at location $V_o = \|\mathbf{x}\|$ from the centre of the representative cluster and served by the link to the nearest DBS with a distance $R_1 = \|\mathbf{x} - \mathbf{y_1}\|$ where $\mathbf{y_1}$ represents the location

of the nearest DBS. Then to evaluate the distribution of the distance R_1, we need to make a random variable transformation and then apply order statistics rules on the well-known distribution of the DBSs distance R to the cluster centre which has the PDF:

$$f_R^M(r) = \frac{2r}{\sigma_M^2},\ 0 \leq r \leq \sigma_M, \tag{5.16}$$

and CDF $F_R^M(r) = \frac{r^2}{\sigma_M^2},\ 0 \leq r \leq \sigma_M$. We also assume that the distance V_o from the DMU to the cluster centre is a random variable with PDF,

$$f_{V_o}^M(v_o) = \frac{2v_o}{\sigma_M^2},\ 0 \leq v_o \leq \sigma_M. \tag{5.17}$$

Then, by performing a joint random variable transformation of $f_R^M(r)$ such that the distance $D(R, V_o) = \sqrt{V_o^2 + R^2 - 2V_oR\cos(\theta)}$ is the distance from the DMU at V_o and any arbitrary DBS at distance R from the centre of the cluster and θ is the angle between the lines R and V_o with the PDF $f_\Theta(\theta) = \frac{1}{2\pi}, 0 \leq \theta \leq 2\pi$, then the distribution of the distance R conditioned that DMU is at location V_o will have the PDF as follows [92]:

$$f_R^M(r|v_o, \sigma_M) = \begin{cases} f_{R^{(1)}}^M(r|v_o, \sigma_M) = \frac{2r}{\sigma_M^2}, & 0 \leq r \leq \sigma_M - v_o, \\ f_{R^{(2)}}^M(r|v_o, \sigma_M) = \frac{2r}{\pi\sigma_M^2} & \\ \qquad \times \arccos\left(\frac{r^2+v_o^2-\sigma_M^2}{2v_or}\right), & \sigma_M - v_o < r \leq \sigma_M + v_o, \end{cases} \tag{5.18}$$

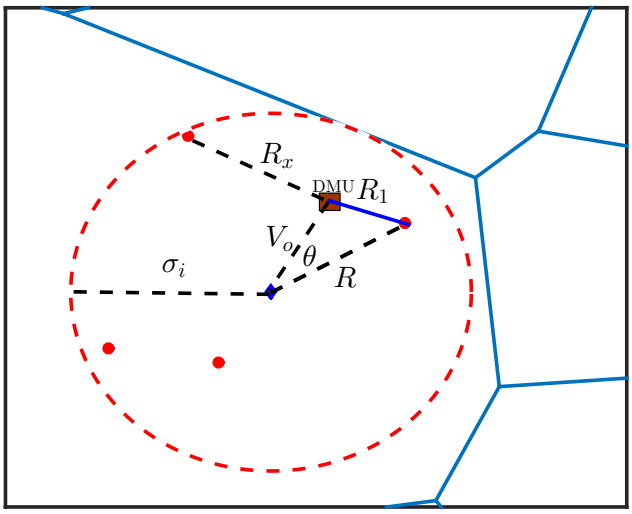

FIGURE 5.2: Spatial distribution of network elements. Brown square for the DMU. Red circles for DBSs. Red dashed circle is the recovery area. Blue diamond is the centre of the Voronoi cell (i.e., destroyed BS).

with the following CDF:

$$F_R^M(r|v_o) = \begin{cases} F_{R^{(1)}}^M(r|v_o) = \frac{r^2}{\sigma_M^2}, & 0 \le r \le \sigma_M - v_o, \\ F_{R^{(2)}}^M(r|v_o) = \frac{r^2}{\pi\,\sigma_M^2}\left(\theta_1 - \frac{1}{2}\,\sin\left(2\,\theta_1\right)\right) & \\ \qquad + \frac{1}{\pi}\left(\theta_2 - \frac{1}{2}\,\sin\left(2\,\theta_2\right)\right), & \sigma_M - v_o < r \le \sigma_M + v_o, \end{cases} \tag{5.19}$$

with $\theta_1 = \arccos\left(\frac{r^2-\sigma_M^2+v_o}{2v_o r}\right)$ and $\theta_2 = \arccos\left(\frac{-r^2+\sigma_M^2+v_o}{2v_o\sigma_M}\right)$.

Next, the distribution of the distance R_1 from the typical DMU and the nearest DBS can be evaluated as in the next proposition.

Proposition 5.1

The distribution of the distance R_1 from the typical DMU at V_o and the nearest DBS can be evaluated for MCP as in (5.20).

$f_{R_1}^M(r_1|v_o, \sigma_M) =$

$$
\begin{cases}
f^{M}_{R_1^{(1)}}(r_1|v_o,\sigma_M) = \frac{2N_d r_1}{\sigma_M^2}\left(1-\frac{r_1^2}{\sigma_M^2}\right)^{N_d-1}, & 0 \le r_1 \le \sigma_M - v_o, \\
f^{M}_{R_1^{(2)}}(r_1|v_o,\sigma_M) = \frac{2N_d r_1}{\pi\sigma_M^2}\arccos\left(\frac{r_1^2+v_o^2-\sigma_M^2}{2v_o r_1}\right) & \\
\quad \times\left[1-\left(\frac{r_1^2}{\pi\,\sigma_M^2}\left(\theta_1^1-\frac{1}{2}\sin\left(2\,\theta_1^1\right)\right)\right.\right. & \\
\quad \left.\left.+\frac{1}{\pi}\left(\theta_2^1-\frac{1}{2}\sin\left(2\,\theta_2^1\right)\right)\right)\right]^{N_d-1}, & \sigma_M - v_o < r_1 \le \sigma_M + v_o,
\end{cases}
\tag{5.20}
$$

with $\theta_1^1 = \arccos\left(\frac{{r_1}^2-\sigma_M^2+v_o}{2v_o r_1}\right)$ and $\theta_2^1 = \arccos\left(\frac{-{r_1}^2+\sigma_M^2+v_o}{2v_o\sigma_M}\right)$.

Proof. Let, N_d BSs be distributed uniformly inside a circle of radius σ_M, Then the derivation of the nearest neighbour distribution amongst the N_d DBSs follows the order statistics using the fact that for general N_d i.i.d. random variables $Z_i \in \{Z_1, Z_2, ..., Z_{N_d}\}$ ordered in ascending order with PDFs $f_{Z_i}(z)$. Then the PDF of $Z_1 = \min_i(Z_i)$ can be written as $f_{Z_1}(z) = N\left(1-F_{Z_i}(z)\right)^{N-1} f_{Z_i}(z)$ [93]. Then, by applying this to (5.18), we can write the PDF of the distance R_1 as

$$
f^{M}_{R_1}(r_1|v_o,\sigma_M) = \begin{cases} f^{M}_{R_1^{(1)}}(r_1|v_o,\sigma_M), & 0 \le r_1 \le \sigma_M - v_o, \\ f^{M}_{R_1^{(2)}}(r_1|v_o,\sigma_M), & \sigma_M - v_o < r_1 \le \sigma_M + v_o, \end{cases}
\tag{5.21}
$$

where

$$
f^{M}_{R_1^{(1)}}(r_1|v_o,\sigma_M) = N_d(1-F^{M}_{R^{(1)}}(r_1|v_o))^{N_d-1} f^{M}_{R^{(1)}}(r_1|v_o), \tag{5.22}
$$

$$
f^{M}_{R_1^{(2)}}(r_1|v_o,\sigma_M) = N_d(1-F^{M}_{R^{(2)}}(r|v_o))^{N_d-1} f^{M}_{R^{(2)}}(r_1|v_o). \tag{5.23}
$$

□

From the previous proposition, $f_{R_1}^M(r_1|v_o,\sigma_M)$ can be easily integrated in (5.20) to get the CDF of the nearest neighbour distance distribution as

$$F_{R_1}^M(r_1|v_o,\sigma_M) = \begin{cases} (1-F_{R^{(1)}}^M(r_1|v_o,\sigma_M))^{N_d}, & 0 \le r \le \sigma_M - v_o, \\ (1-F_{R^{(2)}}^M(r_1|v_o,\sigma_M))^{N_d}, & \sigma_M - v_o < r \le \sigma_M + v_o. \end{cases} \tag{5.24}$$

Proposition 5.2

The distribution of distance R_x from the in-cluster DBSs interferers to the typical user located at distance V_o from the cluster centre (conditioned that the nearest neighbour DBS is at distance R_1 with the distribution in (5.20)) is as follows:

$$f_{R_x}^M(r_x|v_o,\sigma_M,r_1) = \begin{cases} \frac{2r_x}{\sigma_M^2 - r_1^2}, & 0 \le r_x \le \sigma_M - v_o, \\ \dfrac{\frac{2r_x}{\pi\sigma_M^2}\arccos\left(\frac{r_x^2+v_o^2-\sigma_M^2}{2v_o r_x}\right)}{1-\frac{r_1^2}{\pi\sigma_M^2}\left(\theta_1^1-\frac{1}{2}\sin\left(2\theta_1^1\right)\right)-\frac{1}{\pi}\left(\theta_2^1-\frac{1}{2}\sin\left(2\theta_2^1\right)\right)}, & \sigma_M - v_o < r_x \le \sigma_M + v_o. \end{cases} \tag{5.25}$$

Proof. The proof of this is simple. Following from the fact that the distance to the nearest interferer is larger than the serving distance R_1, then the area of the circle formed by the distance from the typical user and the serving DBS is truncated from the whole area. Therefore, we can write the conditional distribution of this event as follows:

$$\begin{aligned} f_{R_x}^M(r_x|v_o,\sigma_M,r_1) &= f_R^M(r_x|v_o,\sigma_M), R > r_1 \\ &= \frac{f_R^M(r_x|v_o,\sigma_M)}{\int_{r_1}^{\infty} f_R^M(r|v_o,\sigma_M)dr} \\ &= \frac{f_R^M(r_x|v_o,\sigma_M)}{1-F_R^M(r_1|v_o,\sigma_M)}. \end{aligned} \tag{5.26}$$

Hence, by substituting $f_R^M(r_x|v_o,\sigma_M)$ and $F_R^M(r_1|v_o,\sigma_M)$ into (5.25) we complete the proof. □

Following on from the above proposition, we can easily show that the distribution of distances from the DMU at V_o to the out-of-cluster interferers can be evaluated for a MCP as in the next proposition.

Proposition 5.3

The PDF of the distance distribution from the typical user at distance V_o from the cluster centre to the interfering DBSs from out of the representative cluster can be written for MCP as

$$f_{R_o}^M(r_o|u,\sigma_M) = f_R^M(r_o|u,\sigma_M). \tag{5.27}$$

Proof. The proof of this follows the same steps used to evaluate (5.19) by doing the joint transformation for the uniformly chosen DBS - see also [87]. □

In the previous proposition, we assumed that the relative distances from the cluster DBSs to any typical DMU inside the cluster is independently identical amongst all the clusters. Hence, we will use shifted versions of (5.27) to complete the coverage probability analysis (see(5.42)) [62, P.90,Col.4.13].

5.3.3 Distance Distributions for TCP

Conditioning on the typical user located at distance $V_o = \|\mathbf{x}\|$ from the cluster centre we can write the PDF of the distribution of distance from any arbitrary

chosen drone to the typical user at v_o for TCP as [87]:

$$f_R^T(r|v_o,\sigma_T) = \frac{r}{\sigma_T^2}\exp\Big(-\frac{r^2+v_o^2}{2\sigma_T^2}\Big)\mathcal{I}_o\left(\frac{rv_o}{\sigma_T^2}\right), \tag{5.28}$$

and the CDF as:

$$F_R^T(r|v_o,\sigma_T) = 1 - Q_1\left(\frac{v_o}{\sigma_T},\frac{r}{\sigma_T}\right). \tag{5.29}$$

The distance V_o from the DMU to the cluster centre is also a random variable with the PDF,

$$f_{V_o}^T(v_o) = \frac{1}{\sigma_T^2}\exp\left(-\frac{v_o^2}{2\sigma_T^2}\right). \tag{5.30}$$

The nearest neighbour DBS to the typical user located at distance V_o from the centre of the cluster can be evaluated as follows in the next proposition.

Proposition 5.4

The PDF of the distance R_1 from the typical user at a distance V_o from the cluster centre to the nearest DBSs for TCP can be evaluated as

$$f_{R_1}^T(r_1|v_o,\sigma_T) = \frac{N_d r_1}{\sigma_T^2}\exp\Big(-\frac{r_1^2+v_o^2}{2\sigma_T^2}\Big)\mathcal{I}_o\left(\frac{r_1 v_o}{\sigma_T^2}\right) \times\left(Q_1\left(\frac{v_o}{\sigma_T},\frac{r_1}{\sigma_T}\right)\right)^{N_d-1}, \tag{5.31}$$

where $Q_1\left(\frac{v_o}{\sigma_T},\frac{r}{\sigma_T}\right)$ is the Marcum Q-function, and $\mathcal{I}_o\left(\frac{rv_o}{\sigma_T^2}\right)$ is the first kind Bessel function.

Proof. This can be evaluated by assuming that the number of drones (N_d) per cluster is fixed and using the order statistics of the distance distribution of the

cluster DBSs points to the typical user located at distance V_o from the centre of the cluster. □

In the next proposition we show the distribution of the distance from the in-cluster interferers and the typical DMU.

Proposition 5.5

The distribution of distance R_x from the in-cluster DBSs interferers to the typical user located at distance V_o from the cluster centre (conditioned that the nearest neighbour DBS is at distance R_1 with the distribution in (5.31)) can be written as

$$f^T_{R_x}(r|v_o,\sigma_T,r_1)=\frac{\frac{r_x}{\sigma_T^2}\exp\left(-\frac{r_x^2+v_o^2}{2\sigma_T^2}\right)\mathcal{I}_o\left(\frac{r_x v_o}{\sigma_T^2}\right)}{Q_1\left(\frac{v_o}{\sigma_T},\frac{r_1}{\sigma_T}\right)}. \tag{5.32}$$

Proof. The proof follows the same steps as in (5.26) □

Following the above proposition, we can easily show that the distribution of distances from the typical user at V_o to the out-of-cluster interferers can be evaluated for TCP as in the next proposition.

Proposition 5.6

The PDF of the distance distribution R_o from the typical user at distance v_o from the cluster centre to the interfering DBSs out of the representative cluster can be written for TCP as

$$f^T_{R_o}(r_o|u,\sigma_T)=\frac{r_o}{\sigma_T^2}\exp\Big(-\frac{r_o^2+u^2}{2\sigma_T^2}\Big)\mathcal{I}_o\left(\frac{r_o u}{\sigma_T^2}\right). \tag{5.33}$$

Proof. Proof follows the same steps as in Proposition 5.3. □

5.4 Coverage Probability

In order to characterize the link level performance of DSCNs, we employ coverage probability as a metric. The coverage probability of an arbitrary user is defined as the probability at which the received signal-to-interference-ratio (SIR^i) is larger than a pre-defined threshold β such that [7]

$$P_c^i = \Pr\{\mathrm{SIR}^i \geqslant \beta\}, \quad i \in \{M, T\}. \tag{5.34}$$

Then, considering that both the DBS and the MBS networks are sharing the same channel resources, the SIR^i can be quantified as:

$$\mathrm{SIR}^i = \frac{P_D \left|g\right|^2 \bar{L}_d(r_1)}{I_{\Phi^i_{C_{in}}} + I_{\Phi^i_{C_{out}}} + I_{\Phi_S}} = \frac{P_D \left|g\right|^2 \bar{L}_d(r_1)}{I^i_{tot}}, i \in \{M, T\}. \tag{5.35}$$

where

$$I_{\Phi^i_{C_{in}}} = \underbrace{\sum_{\mathbf{y} \in \Phi^i_{C_{in}}} P_D \left|g\right|^2 \frac{\left(h^2 + \|\mathbf{x_0} + \mathbf{y}\|^2\right)^{-1}}{\bar{\kappa}\left(\|\mathbf{x_0} + \mathbf{y}\|\right)}}_{\text{In-cluster interference}}, \tag{5.36}$$

$$I_{\Phi^i_{C_{out}}} = \underbrace{\sum_{\mathbf{x} \in \Phi^i_D \setminus \mathbf{x_0}} \sum_{\mathbf{y} \in \Phi^i_{C_\mathbf{x}}} P_D \left|g\right|^2 \frac{\left(h^2 + \|\mathbf{x} + \mathbf{y}\|^2\right)^{-1}}{\bar{\kappa}\left(\|\mathbf{x} + \mathbf{y}\|\right)}}_{\text{Out-of-cluster intereference}}, \tag{5.37}$$

$$I_{\Phi_S} = \underbrace{\sum_{\mathbf{x} \in \Phi_S} P_S \left|g\right|^2 L_S(\|\mathbf{x}\|)}_{\text{Interference from survival BSs}}. \tag{5.38}$$

[7] The network is assumed to be operating in an interference limited regime, (i.e., performance of all links is dependent upon co-channel interference and thermal noise at the receiver front-end is negligible).

Here r_1 represents the distance from the DMU to the nearest DBS; $|g|^2$ is the channel power gain coefficient and it is assumed to be the same for all the links; $I_{\Phi^i_{C_{in}}}$ represents the received interference from the DBSs in the representative cluster; $I_{\Phi^i_{C\,out}}$ represents the received interference from the co-channel DBSs concurrently transmitting with the considered representative link from out of the cluster; I_{Φ_S} is the interference received from the retained MBSs; and P_S and P_D are the transmit power for the MBS and DBS respectively. Consequently, the coverage probability can be evaluated as

$$\begin{aligned} P_c^{i_s} &= \Pr\{\mathrm{SIR}^{i_s} \geqslant \beta\}, \\ &= \Pr\{|g|^2 \geqslant I^i_{tot}\beta\bar{\kappa}(r_1)\left(r_1^2+h^2\right)/P_D\}, \\ &\overset{(a)}{=} \mathbb{E}_{r_1,\sigma_i}\Big[\mathbb{E}_{I^i_{tot}}\Big[\exp\left(-sI^i_{tot}\right)\Big]\Big], \\ &\overset{(b)}{=} \mathbb{E}_{r_1,\sigma_i}\left[\mathcal{L}_{I_{\Phi^i_{C_{in}}}}(s|r_1,\sigma_i)\mathcal{L}_{I_{\Phi^i_{C_{out}}}}(s|r_1,\sigma_i)\mathcal{L}_{I_{\Phi_S}}(s)\right] \end{aligned} \tag{5.39}$$

where $s = \beta\left(r_1^2+h^2\right)\bar{\kappa}(r_1)/P_D$, (a) is obtained by averaging over the channel coefficient and (b) is obtained by applying the definition of the Laplace transform and then using the addition property of the Laplace transformation of independent random variables.

Next, we introduce the coverage probability for DMU under the two deployment topologies rendered via MCP and TCP.

5.4.1 Coverage Probability for MCP

To complete the analysis of the coverage probability, we need to quantify the Laplace transformations for the interference at the typical DMU. In the next

lemma, we introduce the Laplace transform of the distribution of the in-cluster interference for the MCP.

Lemma 5.1

The Laplace transform of the interference at the DMU from the in-cluster DBSs for MCP can be evaluated as

$$\mathcal{L}_{I_{\Phi^M_{C_{in}}}}(s|r_1,\sigma_M)=\sum_{i=1}^{N_d}\left(\int_{r_1}^{\infty}\frac{f^M_{R_x}(r_x|v_o,\sigma_M)}{1+\frac{sP_D}{\bar{\kappa}(r_x)(h^2+r_x^2)}}\,\mathrm{d}r_x\right)^{i-1}\times\xi(i,N_d), \tag{5.40}$$

where

$$\xi(i,N_d)=\frac{\bar{N}_d^i\exp(-\bar{N}_d)}{i!\Sigma_{k=1}^{N_d}\frac{\bar{N}_d^k\exp(-\bar{N}_d)}{k!}}. \tag{5.41}$$

Proof. Please refer to Appendix A.1. □

In order to complete the analysis of the coverage probability, we also need to derive the Laplace transform of the interference from out-of-cluster DBSs (see Lemma 5.2).

Lemma 5.2

The Laplace transform of the interference distribution at the DMU from out-of-cluster DBSs for MCP can be evaluated as in (5.42).

$$\mathcal{L}_{I_{\Phi^M_{C_{out}}}}(s|\sigma_M)=\exp\Big(-2\pi\lambda_D\int_0^{\infty}\Big(1-\exp\Big(-\frac{N_d}{N_c}\times\int_0^{\infty}\Big(1-\frac{1}{1+sP_D\bar{\kappa}(u)(h^2+u^2)}\Big)f^M_{R_o}(u|v,\sigma_M)du\Big)\Big)vdv\Big). \tag{5.42}$$

Proof. Please refer to Appendix A.2. □

5.4.2 Coverage Probability for TCP

For the sake of comparative analysis, the Laplace transform of the distribution of the in-cluster interference for TCP, can be obtained in the following Lemma.

Lemma 5.3

The Laplace transform of the interference at the DMU from the in-cluster DBSs for TCP can be evaluated as:

$$\mathcal{L}_{I_{\Phi^T_{C_{in}}}}(s|r_1,\sigma_T) = \sum_{i=1}^{N_d} \left(\int_{r_1}^{\infty} \frac{f^T_{R_x}(r_x|v_o,\sigma_T)}{1+\frac{sP_D}{\bar{\kappa}(r_x)(h^2+r_x^2)}}\, \mathrm{d}r_x \right)^{i-1} \times \xi(i,N_d). \quad (5.43)$$

Proof. Please refer to Appendix A.3. □

Lemma 5.4

The Laplace transform of the interference distribution at the DMU from out-of-cluster DBSs for TCP can be evaluated as:

$$\mathcal{L}_{I_{\Phi^T_{C_{out}}}}(s|\sigma_T) = \exp\Big(-2\pi\lambda_D \int_0^{\infty} \Big(1-\exp\Big(-\frac{N_d}{N_c} \times \int_0^{\infty} \Big(1-\frac{1}{1+sP_D\bar{\kappa}(u)(h^2+u^2)}\Big) f^T_{R_o}(u|v,\sigma_T)du\Big)\Big)vdv\Big). \quad (5.44)$$

Proof. Please refer to Appendix A.4. □

The Laplace transform of the interference from the retained MBSs is calculated in Lemma 5.5. In this Lemma, we will relax the dependency of the

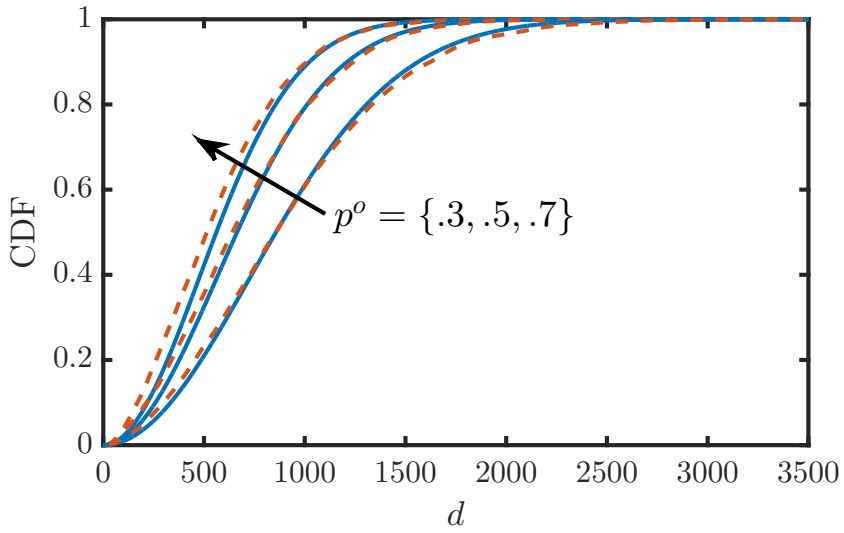

FIGURE 5.3: Nearest MBS distribution CDF for TCP. $\lambda = 1 \times 10^{-6}$. Dashed line for Monte-Carlo simulation. Solid line for the relaxed distance distribution $F_D(d) = 1 - \exp(-\pi\lambda_S d^2)$.

drone network parent points and the location of the retained BSs. In other words, we will relax the dependency of location between the retained MBSs and the typical DMU. This relaxation is compulsory, since the distribution of the distance between the retained MBSs and the desired DMU is not known for correlated BSs and DMUs locations. Moreover, this assumption is assumed to be close to the true value since we are averaging over the random user location at V_o which will average to a location at the location of the parent point (i.e., the destroyed BS), and this is valid for both the MCP and TCP topologies. An insight into the accuracy of this assumption is shown in Figure 5.3. The figure shows the CDF of a distance D from the typical DMU at V_o to the nearest neighbour retained MBS.

Lemma 5.5

The Laplace transform of the interference distribution at the drone typical user from the retained MBSs with density $\lambda_S = (1 - p^o)\lambda$ can be

approximated as follows:

$$\mathcal{L}_{I_{\Phi_S}}(s) = \exp\Big(- \pi \frac{\lambda_S}{N_c} \frac{s^{-\frac{2}{\alpha}} P_S^{-\frac{2}{\alpha}}}{\operatorname{sinc}\left(\frac{2}{\alpha}\right)} \Big) \tag{5.45}$$

where $s = \beta \left(r_1^2 + h^2\right) \bar{\kappa}(r_1)/P_D$.

Proof. The proof of this is straight forward from the Laplace transform of the PPP and can be illustrated as follows:

$$\begin{aligned}
\mathcal{L}_{I_{\Phi_S}}(s) &= \mathbb{E}(\exp(-sI_{\Phi_S})), \\
&= \mathbb{E}(\exp(-s \sum_{\mathbf{x}\in\mathbf{\Phi_S}} P_S \left|g\right|^2 L_S(\|\mathbf{x}\|))), \\
&= \mathbb{E}_{\Phi_S}\Big(\prod_{\mathbf{x}\in\mathbf{\Phi_S}} \mathbb{E}_{|g|^2}\Big(\exp\Big(-s \left|g\right|^2 L_S(\|\mathbf{x}\|)\Big)\Big)\Big), \\
&\overset{(a)}{=} \exp\Big(- 2\pi\lambda_S \int_0^\infty \frac{sP_S K_S^{-1} r^{-\alpha+1}}{1 + sP_S K_S^{-1} r^{-\alpha}} \,\mathrm{d}r\Big), \\
&\overset{(b)}{=} \exp\Big(- 2\pi \frac{\lambda_S}{N_c} \frac{s^{-\frac{2}{\alpha}} P_S^{-\frac{2}{\alpha}}}{\operatorname{sinc}\left(\frac{2}{\alpha}\right)} \Big)
\end{aligned} \tag{5.46}$$

where (a) is obtained by applying the expectation over the fading channel coefficient assuming i.i.d. Rayleigh channels followed by the probability generating functional (PGFL) of the PPP of the Rayleigh distribution and then followed by Cartesian to polar transformation and then solving the integration to get (b) which completes the proof. □

Theorem 5.1

The coverage probability of a typical DMU with fixed recovery cell radius σ_i can be respectively evaluated for Matérn and Thomas cluster processes as

$$P_c^M(\sigma_M) = \int_0^\infty \int_0^\infty \mathcal{L}_{I_{\Phi^M_{C_{out}}}}(s|r_1,\sigma_M)\mathcal{L}_{I_{\Phi^M_{C_{in}}}}(s|r_1,\sigma_M)\mathcal{L}_{I_{\Phi_S}}(s) \times f^M_{R_1}(r_1) f^M_{V_o}(v_o)\,\mathrm{d}r_1\,\mathrm{d}v_o, \tag{5.47}$$

and

$$P_c^T(\sigma_T) = \int_0^\infty \int_0^\infty \mathcal{L}_{I_{\Phi^T_{C_{out}}}}(s|r_1,\sigma_T)\mathcal{L}_{I_{\Phi^T_{C_{in}}}}(s|r_1,\sigma_T)\mathcal{L}_{I_{\Phi_S}}(s) \times f^T_{R_1}(r_1) f^T_{V_o}(v_o)\,\mathrm{d}r_1\,\mathrm{d}v_o. \tag{5.48}$$

Theorem 5.2

The coverage probability of a typical DMU with variable recovery area cell radius σ_i can be respectively evaluated for Matérn and Thomas cluster processes as:

$$P_c^{M_s} = \int_0^\infty P_c^M(\sigma_M) f_{\sigma_M}(\sigma_M)\,\mathrm{d}\sigma_M, \tag{5.49}$$

and

$$P_c^{T_s} = \int_0^\infty P_c^T(\sigma_T) f_{\sigma_T}(\sigma_T)\,\mathrm{d}\sigma_T, \tag{5.50}$$

where the superscript s denotes to the fact that the coverage probability will be averaged over the Stienen's cell radius.

Next, we will use the coverage probability results above to quantify area spectral and energy efficiencies.

5.5 Area Spectral Efficiency and Energy Efficiency

Until now, we have studied the coverage probability for the two assumed system models. To study the network level performance, we need to quantify the Area Spectral Efficiency (ASE) of the network given that a channel reuse is assumed. In this section we show analysis of ASE for both the MCP and the TCP.

Proposition 5.7

Given the coverage probabilities in (5.49) and (5.50), the ASE of the network for MCP can be evaluated as

$$ASE_M = \lambda_D N_d N_c P_c^{M_s} \log_2 (1+\beta), \tag{5.51}$$

and for TCP as

$$ASE_T = \lambda_D N_d N_c P_c^{T_s} \log_2 (1+\beta). \tag{5.52}$$

In order for a comprehensive study of the network, we also make use of the term energy efficiency (E_{eff}). The E_{eff} (in general) can be evaluated as [94]:

$$E_{eff} = \frac{\text{Area Spectral Efficiency}}{\text{Average Network Power Consumption}} = \frac{ASE}{\lambda_D N_d P_D}. \tag{5.53}$$

Given the ASE in (5.51) and (5.52), we can evaluate E_{eff} for MCP as

$$E_{eff}^M = \frac{N_c P_c^{M_s} \log_2 (1+\beta)}{P_D}, \text{ b/J/Hz}, \tag{5.54}$$

TABLE 5.1: Simulation parameters.

Parameter	Value	Description
$\zeta_{LoS}, \zeta_{NLoS}$	1,20 dB	Excess path-loss
f_{MHz}	900 MHz	Carrier frequency
α	3.5	Path loss exponent
K	132 dB	Excess path-loss for macro cells
a_1, b_1	$9.6, 0.28$	Environment dependent constants
λ	1×10^{-6}	Base stations density
N_c	$2, 1$	Available number of channels
P_D	1 dBW	Drone cell transmission power
P_S	10 dBW	MBS cell transmission power

and for TCP as

$$E_{eff}^{T} = \frac{N_c P_c^{T_s} \log_2(1+\beta)}{P_D}. \text{ b/J/Hz} \tag{5.55}$$

5.6 Results and Discussion

In this section, we show numerical results for the coverage probabilities (i.e., $P_c^{M_s}$ and $P_c^{T_s}$) and energy efficiency (i.e., E_{eff}^{M} and E_{eff}^{T}) of drone-based communication recovery network deployment. Furthermore, we assume that the DBSs are operating in an urban environment with the parameters shown in Table 5.1.

Figure 5.4 shows the coverage probability of a random uniformly chosen user inside the recovery area for both MCP and TCP with fixed cluster size (see (5.47) and (5.48)). The coverage probability is plotted against both the cluster radius (σ_i) and the DBSs altitude (h). An interesting observation here is that the drone-based clustered recovery network can achieve a significant enhancement of the coverage probability when the cluster radius is around a

certain value and the optimal point changes by changing the height of the drones and vice versa. That is, we will have a unique optimal drone height for every chosen cluster radius σ_i. We can notice also that a significant coverage probability can be achieved inside of the clusters with coverage figures up to 0.85 by only utilizing $N_d = 3$ drones with one channel. It is worth also to keep in mind that the proposed system is considering a user centric distribution where the location of the drones is coupled with the location of the users where the capacity needs to be extended. This means that these coverage probabilities can be achieved only inside of the circular shaped coverage areas of the recovery cells. Moreover, choosing between MCP and TCP as a framework for the network performance analysis does actually depend on the distribution of the users in the targeted recovery areas (e.g., uniformly for rural areas and normally for high-dense urban areas). This due to the fact that the cellular infrastructure is actually being built towards the user and hence the distribution of the users will define which type of cluster process is more suitable for the recovery network.

Remark 5.4

For the case of $\lambda = 1 \times 10^{-6}$, the average optimal cell size is close to 250m which is approximately the same as the Stenien's cell average radius. That is, the variable cell radius is more realistic and gives an implicit optimal selection of the recovery cell radius.

Figure 5.5 depicts the coverage probability against the altitude of the drones for both of the MCP and TCP where the Stenien's cell size is deployed (see (5.49) and (5.50)). The coverage probability shows that for a thinning probability of 0.1, with 5 drones deployed in every cluster, the optimal drone altitude will slightly change as the number of channels increases and this will

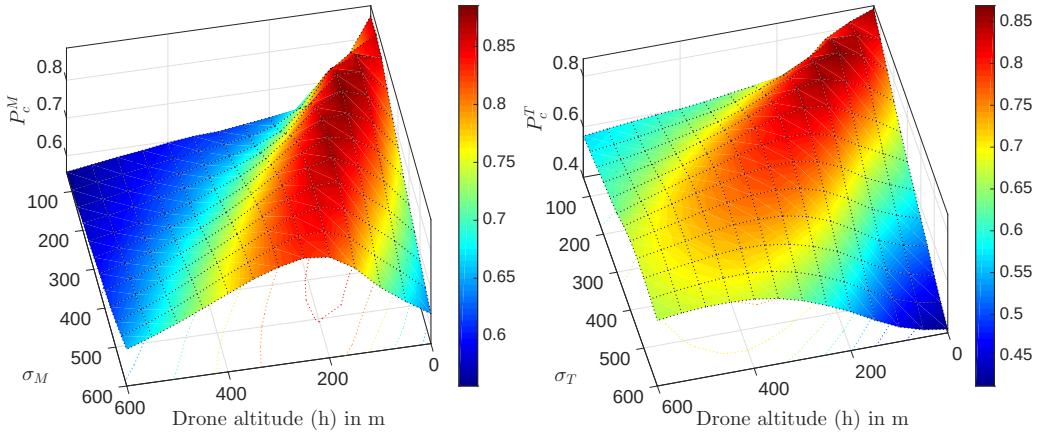

(A) Coverage probability for MCP. (B) Coverage probability for TCP.

FIGURE 5.4: Coverage probability for an arbitrarily chosen typical user for fixed value of recovery cell radius σ_i. $N_c = 1$, $p^o = 0.2$, $\lambda = 1 \times 10^{-6}$, $N_d = 3$, $\alpha = 3.5$, $P_D/P_S = 0.2$ and $\beta = -5$ dB.

intuitively increase the coverage probability. For example, for TCP, there is an optimal altitude difference of 30m when increasing the number of channels from 2 to 3. This existence of an optimal drone altitude which maximizes the coverage probability is due to the adoption of an LoS/NLoS model for the large-scale path-loss model which is widely addressed in the literature of stochastic geometry [6, 53, 95].

Figure 5.6 shows the coverage probability plotted against the number of drones per cluster for multiple transmit power ratios for both of MCP and TCP where the Stenien's cell size is deployed (see (5.49) and (5.50)). The coverage probability curves show that, for a fixed transmit power ratio, there is an optimal number of drones at which the higher densification of the clusters will not increase the coverage probability. For example, for the configuration where the ratio $P_D/P_S = 1\%$, we need only 3 drones to achieve the optimal coverage. This is an interesting result which is contrary to the idea of densification of the heterogeneous networks. The main reason for this phenomenon is the adoption of the LoS/NLoS 3D model for large-scale fading. This can be further justified

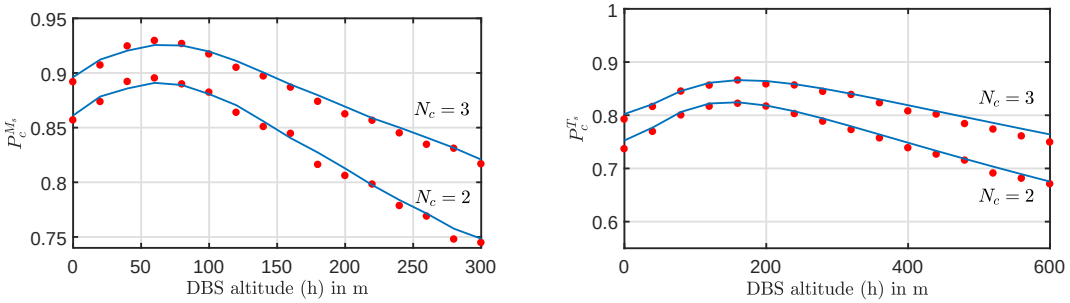

(A) Coverage probability for MCP. (B) Coverage probability for TCP.

FIGURE 5.5: Coverage probability for an arbitrarily chosen DMU for Stenien's recovery for MCP and TCP (see (5.49) and (5.50)). Original MBS and DMU densities is $\lambda = 1 \times 10^{-6}$. The destruction probability $p^o = 0.1$. $\alpha = 3.5$. $N_d = 5$. and $P_D/P_S = 0.2$. Blue solid lines for the exact solution and the red dots for the Monte-Carlo simulation.

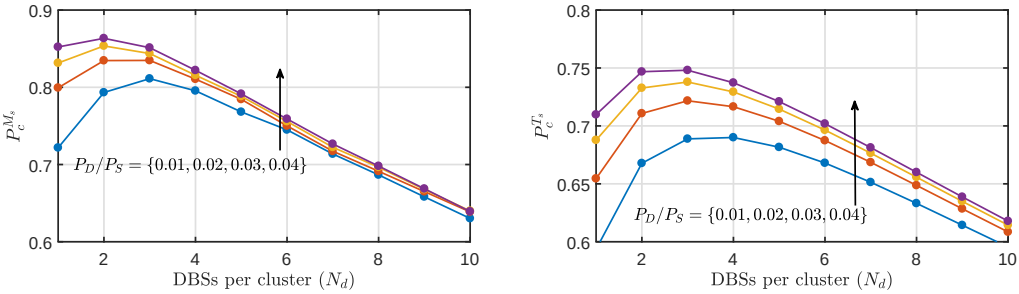

(A) Coverage probability for MCP. (B) Coverage probability for TCP.

FIGURE 5.6: Original MBSs density is $\lambda = 1 \times 10^{-6}$. The destruction probability $p^o = 0.1$. $\alpha = 3.5$ and $P_D/P_S = \{1, 2, 3, 4\} \times 10^{-2}$.

as illustrated in [96]. In this chapter, the authors showed that the densification under the 3GPP path-loss models with variable BS elevation will change the behaviour of the network performance metrics with regard to the change of the density of the deployed BSs. That is, for any chosen network density of BSs, there is an optimal density of BSs that gives the optimal coverage probability as well as the optimal ASE. In addition, the BSs density which maximizes the achievable coverage probability will differ from the one which maximizes the ASE.

Remark 5.5

In this chapter, we assumed that the number of drones N_d per cluster is fixed. In fact, this is made for the sake of simplicity and to reduce the number of integrations to average for the coverage probability. This assumption is compromised by the fact that the number of active drones per cluster is a Poisson random number which is captured by (5.41). That is, at any certain snapshot of the network, the number of active drones in any arbitrarily chosen cluster differs from the remaining network clusters. For accurate evaluation of the performance metrics, one needs to consider the number of drones per cluster as a random variable. This random variable should consider the size of the Voronoi cell as a parameter to estimate the number of the required DBSs per cluster. Hence, we need to do a random variable transformation into the Stenien's cell radius to reflect the area of the cell and then relate this area with the effective density of the original network.

Figure 5.7 shows E_{eff} plotted against the number of drones per cluster for multiple configuration of transmit power ratios for both the MCP and TCP where the Stenien's cell size is deployed (see (5.54) and (5.55)). No value of an optimal number of drones can be seen for the case of energy efficiency. That is, as we increase the number of the drones we increase the network throughput. Moreover, the trend of the energy efficiency is to increase as we increase the transmit power ratio.

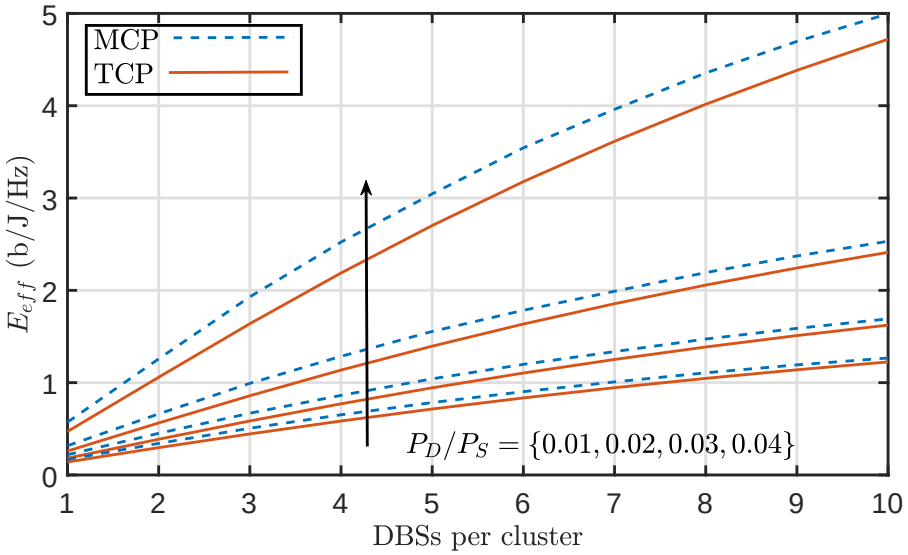

FIGURE 5.7: Energy efficiency vs. the number of drones per cluster. Original MBSs density is $\lambda = 1 \times 10^{-6}$. The destruction probability $p^o = 0.1$. $\alpha = 3.5$. and $P_D/P_S = \{1, 2, 3, 4\} \times 10^{-2}$.

5.7 Conclusion

In this chapter, we introduced a statistical and analytical framework for evaluating the coverage probability and energy efficiency performance metrics for cluster based drones enabled recovery networks. Results show that there are a number of parameters which influence optimal deployment of the recovery network: (i) number of drones in a cluster, (ii) drone altitudes, (iii) transmission power ratio between drone BSs and traditional BSs, and (iv) the recovery area radius. Furthermore, it is also shown that by optimizing these parameters the coverage probability and the energy efficiency of a ground user can be significantly enhanced in a post-disaster situation.

Chapter 6

Optimal Coverage in Downlink Cellular Networks

Contents

In this chapter, we revisit the design aspects for the traditional cellular networks. We present a detailed analysis of the coverage and spectral efficiency of a downlink cellular network. Rather than relying on the first order statistics of received signal-to-interference-ratio (SIR) such as coverage probability, we focus on characterizing its meta-distribution. Our analysis is based on the alpha-beta-gamma (ABG) path-loss model which provides us with the flexibility to analyze urban macro (UMa) and urban micro (UMi) deployments. With the help of an analytical framework, we demonstrate that selection of underlying degrees-of-freedom such as BS height for optimization of first order statistics such as coverage probability is not optimal in the network-wide sense. Consequently, the SIR meta-distribution must be employed to select appropriate operational points which will ensure consistent user experiences across the network. Our design framework reveals that the traditional results which advocate lowering of BS heights or even optimal selection of BS height do not yield consistent service experience across users. By employing the developed framework we also demonstrate how available spectral resources in terms of time slots/channel partitions can be optimized by considering the meta-distribution of the SIR.

6.1 Introduction

6.1.1 Motivation and Related Work

As we described in previous chapters, network densification is considered as a key design tool to satisfy the ever-increasing demand for any-time, anywhere wireless connectivity. The fundamental idea behind densification is to bring the network closer to the user, i.e., reduce the cell size while increasing the density of deployment. Fundamentally, this enables more aggressive spectrum reuse across spatial dimensions, resulting in enhanced network throughput. Moreover, reduction in cell-size results in an improved coverage for the intended users. Nevertheless, the aggressive spatial reuse, when coupled with reduced cell size, poses significant challenges in terms of interference management. This has resulted in a fundamental question which has intrigued network designers and researchers for the past few years: "How are coverage and throughput related to the deployment density?"

To answer this question, the performance of large-scale cellular networks must be quantified in terms of underlying design parameters such as base station (BS) density, path-loss exponents, transmit power employed by BSs and available channel resources, etc. Unfortunately, traditional analysis based on hexagonal tessellation does not yield any significant insight due to lack of analytical tractability. In [97], the authors introduced a tractable approach for the analysis of coverage and rate in large-scale wireless networks using stochastic geometry. In the recent past [62, 98–107], stochastic geometry has been extensively employed to investigate the design space of large-scale cellular deployments under different 5G architectures and access methodologies. The

interested reader is referred to [99] for a detailed survey.

The results in [97] demonstrated that the coverage probability in a signal to interference ratio (SIR) limited scenario is independent of the BSs density. Consequently, the network area spectral efficiency increases with an increase in the BS density. The analysis was revisited in [101] which investigated the impact of line of sight (LoS) and non-line of sight (NLoS) propagation on the coverage and area spectral efficiency. The authors demonstrated that in contrast to [97], there exists an optimal BS density beyond which the area spectral efficiency is reduced with further densification. Both of these analyses ignored the impact of BS height on the network performance. In [103], the authors extended the analysis of [101] to capture the impact of non-zero height difference between user equipment (UE) and BS. The authors presented area spectral efficiency (ASE) crash, i.e. the phenomenon of significant deterioration in ASE with network densification with realistic elevation consideration. This framework is further extended in [96] and [108] under different fading considerations. One of the key observations which follows from these studies is that the BS heights should be lowered as it reduces the path-loss between a UE and a BS. On a closer inspection it is obvious that the path-loss model used in [96] and [108] does not adequately capture the fact that LoS probability increases with an increase in the BS height. while the path-loss and NLoS probability increases with a decrease in BS height. This is indeed adequately captured in [68] and is employed in [6] to investigate optimal height for a low altitude platform empowered with a cellular BS. Consequently, it is obvious that there exists an optimal height for the BS deployment which will maximize the area spectral efficiency and lowering the BS height is not always optimal.

All these investigations are based on first-order analysis, i.e. on the cov-

erage probability. In [102] the authors showed that although the calculation of SIR distribution for the cellular network (which provides a basis for coverage and spectral efficiency calculations) is straight-forward, it only provides limited information about the coverage of individual links. In other words, it is difficult to establish what percentage of links will be able to experience a certain coverage for a desired target SIR threshold from the coverage probability alone. The authors in [102] presented a framework for the evaluation of what is known as the meta-distribution of SIR which is the distribution of coverage conditioned on a point process (see section III for further details). The meta-distribution of the SIR is a better metric as averaging can be often misleading. Notice that the meta-distribution in [102] is for the power-law/path-loss model which does not discriminate between NLoS and LoS propagation. Combining insights from [96, 108] and [102] one may ask a really important design question, i.e., if h^* is the BS height which maximizes the network performance on average, i.e. in terms of coverage probability for instance, does it also minimize the variance in coverage? In other words, is the h^* which maximizes first order performance metric optimal in terms of the SIR meta-distribution. To this end, this chapter presents a comprehensive framework for the investigation of the design space of large-scale cellular networks in terms of the meta-distribution of SIR considering the realistic propagation model.

Remark 6.1

As we described before, this chapter's topic is a natural digression for the work that we addressed in the last chapters. This is because of the similarities between the drone cellular network and the traditional network. The new thing here is the use of higher-order statistics to give further design aspects for the network operators, especially for those who care about the user's fairness in contrast to the traditional best-effort

network design.

6.1.2 Contributions

The key contributions of this chapter are as follows:

1. Considering a very general Alpha-Beta-Gamma (ABG) propagation model, we first quantify the coverage probability and rate coverage probability for downlink communications in a large-scale cellular network.

2. We then present an analytical framework to quantify higher-order moments of the coverage and rate coverage probability which quantify the respective meta-distribution.

3. The meta-distribution of SIR is often recovered using higher-order moments in conjunction with the Gil-Pelaez theorem [102]. However, this requires complex integration for which numerical integration takes a long time to converge. We present a solution based on Mnatsakanov's theorem which simplifies and speeds up the evaluation of the meta-distribution.

4. We investigate the design space of the considered network and present several important insights.

5. Lastly, we consider the resource allocation problem in terms of bandwidth partitioning or time-slot sharing and show how such a problem can be tackled using the meta-distribution.

TABLE 6.1: Path-loss model parameters.

Type	Model	λ range	α	β	γ
UMi	LoS	$10^{-3} - 10^{-5}$	2.0	31.4	2.1
	NLoS	$10^{-3} - 10^{-5}$	3.5	24.4	1.9
UMa	LoS	$10^{-5} - 10^{-7}$	2.8	11.4	2.3
	NLoS	$10^{-5} - 10^{-7}$	3.3	17.6	2.0

6.1.3 Organization

The rest of the chapter is organized as follows: Section 6.2 introduces the system model and deployment geometry of the network. Section 6.3 gives the performance analysis and mathematical modelling. Section 6.4 presents numerical results. Finally, Section 6.5 provides some future work and conclusions.

6.2 System Model

6.2.1 Spatial and Network Models

We consider a large-scale cellular network where the locations of the BSs are modelled by a homogeneous Poisson point process HPPP such that [61]:

$$\Phi = \{\mathbf{x_0}, \mathbf{x_1}, ..., \mathbf{x}_\infty, \forall\ \mathbf{x}_i \in \mathbb{R}^2\}, \tag{6.1}$$

with density λ. We also assume that the Voronoi cell $C(\mathbf{x})$ which is defined as

$$C(\mathbf{x}) = \{\|\mathbf{x}-\mathbf{y}\|^2 \leq \|\mathbf{y}-\mathbf{z}\|^2 \ \ \forall \ \ \mathbf{x} \in \mathbf{\Phi}, \mathbf{z} \in \mathbf{\Phi}\backslash\{\mathbf{x}\}, \mathbf{y} \in \mathbb{R}^2\} \tag{6.2}$$

may have one or more users. At a particular time instance, only a single user is served on a particular resource channel to avoid intra-cell interference.

6.2.2 Propagation Model

Large-Scale Fading

We assume that the large-scale fading model follows the ABG large-scale path-loss model [109], i.e., the path-loss can be written as

$$L_i(h,r)_{dB} = 10\,\alpha_i \log_{10}(\sqrt{h^2+r^2}) + \beta + 10\,\gamma_i \log_{10}(f) + \mathcal{X}_{\sigma_i} \tag{6.3}$$

where h is the vertical difference in height between the BS and the mobile user, r is the horizontal distance between the mobile user and the BS, α_i is the path-loss exponent, $\mathcal{X}_{\sigma_i}$ is the shadow fading deviation in dB for the large-scale fluctuation and γ and β are the ABG path-loss parameters in dB as shown in Table 6.1[1]. The reason for adopting this model is that the model incorporates both NLoS and LoS propagation models and also provides a realistic and practical three-dimensional model that explicitly incorporates the height of the BS as a path-loss parameter. Moreover, this model is valid for UMi/UMa networks since it implicitly shows the valid ranges of the base station densities

[1]For the sake of simplicity and tractability, we will neglect the effect of the log-normal shadowing parameter $\mathcal{X}_{\sigma_i}$ in this chapter.

by giving the terrestrial distance range. In order to capture the actual effect of both the LoS/NLoS parts of the model, we need to know the probability that the user will have LoS connection with the BS at a certain height from the ground. We adopt the same model that is developed in [6]. Hence, the probability of the mobile user to be in LoS/NLoS with the associated BS can be written as

$$\mathcal{P}_L(h,r) = \frac{1}{1 + a_1\, \mathrm{e}^{-b_1 c_1 \tan^{-1}\left(\frac{h}{r}\right) + b_1\, a_1}},\ \mathcal{P}_{NL}(h,r) = 1 - \mathcal{P}_L(r), \tag{6.4}$$

where a_1 and b_1 are environment-dependent constants with $c_1 = 180/\pi$[2].

Small-Scale Fading

It is assumed that large-scale path-loss is complemented with small-scale Rayleigh fading such that $|g|^2 \sim \mathrm{Exp}(1)$ where $|g|^2 \sim$ is the channel gain between any arbitrary user and the BS. Also, it is assumed that the network is operating in an interference limited regime (i.e., performance of all links is limited by the co-channel interference and thermal noise at the receiver front-end is negligible). The assumption of the Rayleigh fading model is due to the simplicity of the analysis. This assumption yields the worst case performance and the analysis can be easily extended to a more generic Nakagami-m fading model. However, the effect of LoS and NLoS components is incorporated into the large-scale fading model given by (6.3).

Transmission Model and Channel Partitioning

In this chapter we assume that the mobile user is associated to the nearest BS (i.e., the BS which maximizes average received SNR) and also assume

[2]From now on, we will write the subscript L to refer to LoS and use NL to refer to $NLoS$.

transmitters on the same frequency are considered as co-channel interferers. The probability density function for the distance R_1 from the downlink user to the nearest BS assuming a HPPP can be written as

$$f_{R_1}(r_1) = 2\pi r_1 \lambda e^{-\pi r_1^2 \lambda}. \tag{6.5}$$

To decrease the level of the aggregate interference and increase network capacity, we assume that channel partitioning is applied (i.e., orthogonal frequency division multiple access (OFDMA) or time division multiple access (TDMA)). That is, the total BS channel bandwidth W is shared in terms of time/frequency. Hence, the channel is partitioned in time/frequency into N_s partitions (i.e., sub-carriers for OFDMA or time-slots for TDMA) and this number of partitions is assigned randomly into N_a active users per cell. In addition, we will neglect the randomness of the number of active users in the cell and assume that N_a is a fixed number (For more details on the distribution of N_a, you can refer to [110]). Moreover, this kind of medium access scheme (i.e., channel partitioning) can be extended to any other medium access scheme (i.e., ALOHA, CSMA, CSMA-CA, etc.).

6.3 Performance analysis

In this section, we study two main types of coverage performance: (i) the coverage probability and (ii) the rate coverage probability. For a complete performance analysis, we evaluate two main higher-order statistics of these metrics. Namely, we quantify the meta-distribution and the spatial capacity. These types of higher-order statistics provide a better insight into the two

main types of cellular services. The first for a best effort network coverage probability and the second for a rate coverage of the network.

6.3.1 Coverage Probability

The coverage probability is defined as the probability that the SIR will be greater than a certain predefined value θ. The average SIR at a downlink user located at the the origin can be quantified as

$$\mathrm{SIR} = \underbrace{\frac{|g|^2 \; L_L^{-1}(r_1)}{I_\Phi}\mathcal{P}_L(r_1)}_{\mathrm{SIR}_L} + \underbrace{\frac{|g|^2 \, L_{NL}^{-1}(r_1)}{I_\Phi}\mathcal{P}_{NL}(r_1)}_{\mathrm{SIR}_{NL}}. \tag{6.6}$$

Here, SIR_L is SIR when there is a LoS link between the user and the BS, SIR_{NL} is SIR when there is a NLoS link between the user and the BS and I_Φ is the aggregate interference from the co-channel transmitting BSs experienced by the mobile user and can be quantified as

$$\begin{aligned} I_\Phi &= I_{\Phi_L} + I_{\Phi_{NL}} \\ &= \sum_{i \in \Phi \setminus \{0\}} |g|^2 \, L_L(h, r_i) + \sum_{m \in \Phi \setminus \{0\}} |g|^2 \, L_{NL}(h, r_m), \end{aligned} \tag{6.7}$$

where Φ is the set of all co-channel active BSs, Φ_L and Φ_{NL} are the set of all LoS and NLoS active base stations, respectively, and r_1 is the horizontal distance from the mobile user to the nearest BS and I_{Φ_L} and $I_{\Phi_{NL}}$ are the aggregate interferences from the LoS and NLoS active base stations, respectively. Here, we assume that the channel power fading coefficients for the co-channel interferers, $|g|^2$, are iid Rayleigh distributed random variables.

The coverage probability for any arbitrary mobile user can be evaluated

as in the following theorem.

Theorem 6.1 ► (Coverage probability)

Coverage probability for any ergodic stationary PPP with a density λ of BSs, N_s channel partitions and N_a active users per cell can be evaluated as

$$P_\theta = \Pr\left[\text{SIR} \geq \theta\right] = \int_0^\infty \left[\mathcal{P}_L(h, r_1)A(r_1, \theta) + \mathcal{P}_{NL}(h, r_1)B(r_1, \theta)\right] f_{R_1}(r_1)\,\mathrm{d}r_1, \tag{6.8}$$

where

$$A(r_1, \theta) = \exp\Big(- 2\pi \frac{\lambda N_a}{N_s} \int_{r_1}^\infty 1 - \eta(s, r)\,\mathrm{d}r\Big)\big|_{s=\frac{\theta}{L_L^{-1}(h, r_1)}},$$
$$B(r_1, \theta) = \exp\Big(- 2\pi \frac{\lambda N_a}{N_s} \int_{r_1}^\infty 1 - \eta(s, r)\,\mathrm{d}r\Big)\big|_{s=\frac{\theta}{L_{NL}^{-1}(h, r_1)}}.$$

with $\eta(s, r)$ defined in Appendix B.1.

Proof. Please refer to Appendix B.1 for proof. □

In the results section, we will focus on the full-load capacity of the network where the number of the active users N_a requiring service at the same time in any cell is equal to the number of channel partitions N_s.

6.3.2 Rate Coverage Probability

The rate coverage is defined as the average probability at which the channel transmission rate will be greater than a certain level such that the rate QoS threshold R_o will be achieved[3]. The coverage rate for a certain threshold R_o

[3]Here, we denote the coverage rate probability as the short term coverage rate.

bits/s/Hz is defined as follows:

$$P_{R_o} = \Pr\left[\frac{W}{N_s}\log_2\left(1+\mathrm{SIR}\right) \geqslant R_o\right] = \Pr[\mathrm{SIR} \geqslant 2^{\frac{R_o N_s}{W}} - 1]. \tag{6.9}$$

By intuition, the total channel bandwidth is divided into the N_s number of channel partitions even for OFDMA or TDMA. For OFDMA it gives the effective channel bandwidth experienced that is associated to the user. For the TDMA scheme, it is the effective time utilization by the user, where $1/N_s$ is the effective normalized throughput of the maximum sum rate. Consequently, the coverage probability for the desired user at the origin can be quantified as in the next theorem.

Theorem 6.2 ▶ (Coverage rate probability)

The coverage rate for any ergodic stationary PPP with a density λ of BSs, N_s channel partitions and N_a active users per cell can be evaluated as

$$P_{R_o} = \int_0^\infty [\mathcal{P}_L(h,r_1)A(r_1,R_o) + \mathcal{P}_{NL}(h,r_1)B(r_1,R_o)]f_{R_1}(r_1)\,\mathrm{d}r_1, \tag{6.10}$$

where

$$A(r_1,R_o) = \exp\Big(-2\pi\frac{\lambda N_a}{N_s}\int_{r_1}^\infty 1-\eta(s,r)\,\mathrm{d}r\Big)\Big|_{s=\frac{2^{\frac{R_o N_s}{W}}-1}{L_L^{-1}(h,r_1)}},$$
$$B(r_1,R_o) = \exp\Big(-2\pi\frac{\lambda N_a}{N_s}\int_{r_1}^\infty 1-\eta(s,r)\,\mathrm{d}r\Big)\Big|_{s=\frac{2^{\frac{R_o N_s}{W}}-1}{L_{NL}^{-1}(h,r_1)}},$$

with $\eta(s,r)$ defined in Appendix B.1.

Proof. The proof follows the same steps as for Theorem 6.1. □

For the derived formulas in (6.8) and (6.10) and the rest of the chap-

ter, we will use the asterisk super-script to refer to the optimal values of the parameters that maximize the chosen coverage function. In particular, we write

$$\{h^*, \lambda^*\}_\theta = \underset{h,\lambda}{\arg}\ \max P_\theta \tag{6.11}$$

for the coverage probability and

$$\{h^*, \lambda^*\}_{R_o} = \underset{h,\lambda}{\arg}\ \max P_{R_o} \tag{6.12}$$

for the rate coverage probability. In the following section, we analyze the meta-distribution for the considered cellular network.

6.3.3 Meta-distribution

The coverage probability and rate coverage derived in (6.8) and (6.10) only provide average performance. Such an averaging does not provide an insight on the network level performance. From a network level perspective, the fraction of the users which can attain a certain desired level of coverage is important to quantify the quality-of-experience for the users. To this end, the authors in [102] introduced the meta-distribution of the coverage which is given as

$$\bar{F}_{P_c}(x) \triangleq \mathbb{P}^! \left(P_c > x\right). \tag{6.13}$$

In other words, the meta-distribution is the complementary cumulative density function (CCDF) of the coverage probability. In this chapter, we are interested in the coverage under the ABG path-loss model which implicitly accounts for

LoS/NLoS propagation:

$$\bar{F}_{P_\theta}(x) \triangleq \mathbb{P}^!(P_\theta \geq x) \text{ and } \bar{F}_{P_{R_o}}(x) \triangleq \mathbb{P}^!(P_{R_o} \geq x) \tag{6.14}$$

where $\mathbb{P}^!$ is the Palm measure conditioned on that the user being located at the origin. More clearly, the meta-distribution provides the probability that any arbitrary user in the network will achieve $P_\theta > x$, $P_{R_o} > x$ in $F_{P_{(.)}} \times 100\%$ of the time. The calculation of the meta-distribution is been made possible by the Gil-Pelaez theorem [111] and can be quantified as

$$\bar{F}_{P_\theta}(x) = \frac{1}{2} + \frac{1}{\pi} \int_0^\infty \frac{\mathrm{Im}[e^{-jt\log x} M_{jt}(\theta)]}{t} \, \mathrm{d}t, \tag{6.15}$$

and

$$\bar{F}_{P_{R_o}}(x) = \frac{1}{2} + \frac{1}{\pi} \int_0^\infty \frac{\mathrm{Im}[e^{-jt\log x} M_{jt}(R_o)]}{t} \, \mathrm{d}t, \tag{6.16}$$

where $M_{jt}(\theta)$ and $M_{jt}(R_o)$ are the complex jb^{th} moments of P_θ and P_{R_o}, respectively and Im[.] is the imaginary part symbol with $j = \sqrt{-1}$. In order to find exact expressions of the meta-distribution, we need to find the expressions for $M_m(\theta)$ and $M_m(R_o)$ which are the real m^{th} moments. This can be quantified as in the following theorem.

Theorem 6.3 ▶ (Moments)

The moments $M_m(\theta)$ and $M_m(R_o)$ for any ergodic stationary PPP with density λ, N_s channel partitions and N_a active users per cell can be evaluated as

$$M_m(\theta) = \int_0^\infty [\mathcal{P}_L(h, r_1) A_m(r_1, \theta) + \mathcal{P}_{NL}(h, r_1) B_m(r_1, \theta)] f_{R_1}(r_1) \, \mathrm{d}r_1, \tag{6.17}$$

$$M_m(R_o) = \int_0^\infty [\mathcal{P}_L(h, r_1) A_m(r_1, R_o) + \mathcal{P}_{NL}(h, r_1) B_m(r_1, R_o)] f_{R_1}(r_1)\, \mathrm{d}r_1, \tag{6.18}$$

where

$$A_m(r_1, \theta) = \exp\Big(-2\pi \frac{\lambda N_a}{N_s} \int_{r_1}^\infty 1 - \eta_m(s, r)\, \mathrm{d}r \Big)\Big|_{s=\frac{\theta}{L_L^{-1}(h, r_1)}},$$
$$B_m(r_1, \theta) = \exp\Big(-2\pi \frac{\lambda N_a}{N_s} \int_{r_1}^\infty 1 - \eta_m(s, r)\, \mathrm{d}r \Big)\Big|_{s=\frac{\theta}{L_{NL}^{-1}(h, r_1)}},$$
$$A_m(r_1, R_o) = \exp\Big(-2\pi \frac{\lambda N_a}{N_s} \int_{r_1}^\infty 1 - \eta_m(s, r)\, \mathrm{d}r \Big)\Big|_{s=\frac{2^{\frac{R_o N_s}{W}} - 1}{L_L^{-1}(h, r_1)}},$$
$$B_m(r_1, R_o) = \exp\Big(-2\pi \frac{\lambda N_a}{N_s} \int_{r_1}^\infty 1 - \eta_m(s, r)\, \mathrm{d}r \Big)\Big|_{s=\frac{2^{\frac{R_o N_s}{W}} - 1}{L_{NL}^{-1}(h, r_1)}},$$

with $\eta_m(s, r)$ defined in Appendix B.2.

Proof. Please refer to Appendix B.2 for proof. □

Here, substituting (6.17) and (6.18) into (6.15) and (6.16) gives exact expressions of the meta-distributions. Unfortunately, this way of evaluating the meta-distribution is intractable and requires a long time for the numerical integrations. To make this more tractable, an excellent precise approximation of the Gil-Pelaez theorem can be obtained by utilizing Mnatsakanov's theorem [112]. Using Mnatsakanov's theorem, we will be able to recover the distribution of any arbitrary random variable, conditioned on the requirement that any real integer's m^{th} moment is defined. Hence, the meta-distribution can be given in approximate value as

$$\bar{F}_{P_\theta}(x) \approxeq \sum_{k=0}^{[\mu x]} \sum_{j=k}^{\mu} \binom{\mu}{j} \binom{j}{k} (-1)^{j-k} M_m(\theta), \tag{6.19}$$

$$\bar{F}_{P_{R_o}}(x) \approxeq \sum_{k=0}^{[\mu x]} \sum_{j=k}^{\mu} \binom{\mu}{j} \binom{j}{k} (-1)^{j-k} M_m(R_o), \tag{6.20}$$

where μ is an arbitrary integer such that the larger it is the more accurate is the approximation. We choose this approximation due to its fast convergence to the exact solution which is evaluated by the Gil-Pelaez theorem which requires integrations of complex numbers. As we will show in the results section, the first 25 moments will be sufficient to precisely recover the distribution. From the m^{th} moments in (6.17) and (6.18), we evaluate the second cumulants (variances) for both coverage probability and rate coverage probability as

$$var(\theta) = M_2(\theta) - M_2^2(\theta), \tag{6.21}$$

$$var(R_o) = M_2(R_o) - M_2^2(R_o). \tag{6.22}$$

These variances provide more insight on the spread of the coverage values over all the users for a certain desired threshold and its deviation from the average value. Intuitively, the less the variance, the better is the fairness between the network users in terms of coverage.

6.3.4 Spatial Coverage Capacity and Spatial Rate Capacity

In order to answer the question "What is the maximum density of the concurrent active users that satisfy a certain predefined coverage reliability?" we derive expressions for the spatial coverage capacity and spatial rate capacity. These metrics provide fine grained characteristics of the cellular network and network level service quality.

Definition 6.1 : (Spatial coverage capacity)

The spatial coverage rate for any ergodic stationary PPP with density λ of BSs, N_s channel partitions and N_a active users per cell is defined as the maximum effective density of users that have SIR values greater than the QoS threshold θ with probability at least $P_\theta = x$ and can be evaluated as

$$SCC(x, \theta, N_s) \triangleq N_a \lambda \bar{F}_{P_\theta}(x), \tag{6.23}$$

and the optimal operating point for network full capacity is defined as

$$\{\lambda^*, h^*, N_s^*\} \triangleq \underset{\lambda, h, N_s}{\arg} SCC(x, \theta, N_s). \tag{6.24}$$

Here, we can use simple two dimensional search algorithms to find this optimal operating point.

Definition 6.2 : (Spatial rate capacity)

The spatial rate capacity for any ergodic stationary PPP with density λ of BSs, N_s channel partitions and N_a active users per cell is defined as the maximum effective density of users that have channel rate values greater than the QoS threshold R_o with probability at least $P_{R_o} = x$ and can be evaluated as

$$SRC(x, R_o, N_s) \triangleq N_a \lambda \bar{F}_{P_{R_o}}(x), \tag{6.25}$$

and the optimal operating point for network full capacity is defined by

$$\{\lambda^*, h^*, N_s^*\} \triangleq \underset{\lambda, h, N_s}{\arg} SRC(x, R_o, N_s). \tag{6.26}$$

Using the accurate approximation we introduced in (6.19) and (6.20), we can easily find the solution for (6.24) and (6.26) without the need for applying the Gil-Pelaez theorem.

From the above analysis of the network performance metrics, we can build a comprehensive framework for analysing network level performance and capture the individual and spatial performance in a fine-grained strategy instead of only looking to the standard average coverage probability metrics.

6.4 Results and Discussion

In this section, we present numerical results for the given evaluated metrics. We will assume an urban environment with the parameters $a_1 = 9.6$, $b_1 = 0.28$, $f = 2$ GHz carrier frequency and the BS total available bandwidth $W = 20$ MHz. Also, as described in the previous sections, we consider Rayleigh flat wireless fading channels.

6.4.1 Impact of Network Densification on Optimal Height and Optimal Average Coverage Probability

In Figure 6.1, we show the optimal BS height and the corresponding optimal values of the coverage probability against BS densities of the network for different values of the SIR θ threshold. In this figure, we clearly observe that the optimal BS height changes as we vary the BS's density. That is, with the adopted LoS/NLoS model of large-scale fading, there is an optimal operational height at which the network operator will gain nearly the same coverage

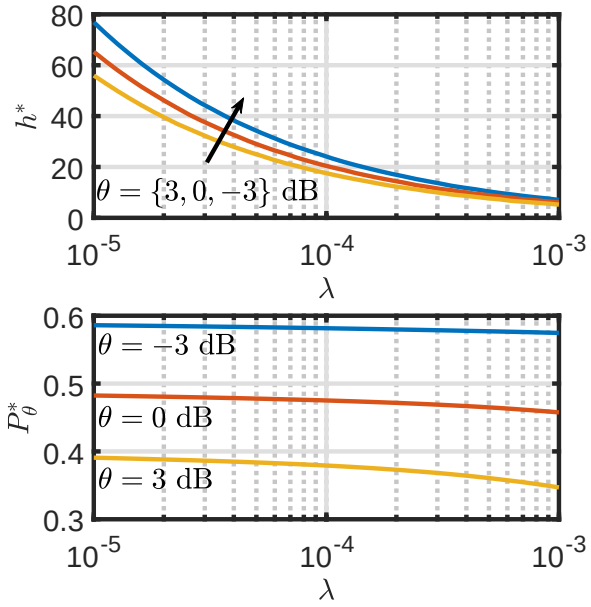

FIGURE 6.1: Optimal values for the BS height (top) and the corresponding coverage probability (bottom) using the ABG-UMi path-loss model for different values of coverage SIR threshold θ.

probability for any chosen base station density. Moreover, the chosen height of the BSs does explicitly depend on the SIR θ threshold which is pre-defined as the QoS metric. This also applies to the rate coverage probability (P_{R_o}) which must be optimized in parallel with the coverage probability.

6.4.2 Optimal Parameter Selection Considering the Variance of the Received SIR

Figure 6.2 shows both the first and second cumulants of the coverage probabilities (i.e., the mean as the coverage probability/rate coverage probability and the variance as a deviation measure). The main motivation for studying the variance is that it is considered as the most important measure of fairness between the users. The most interesting point here is that the slope of

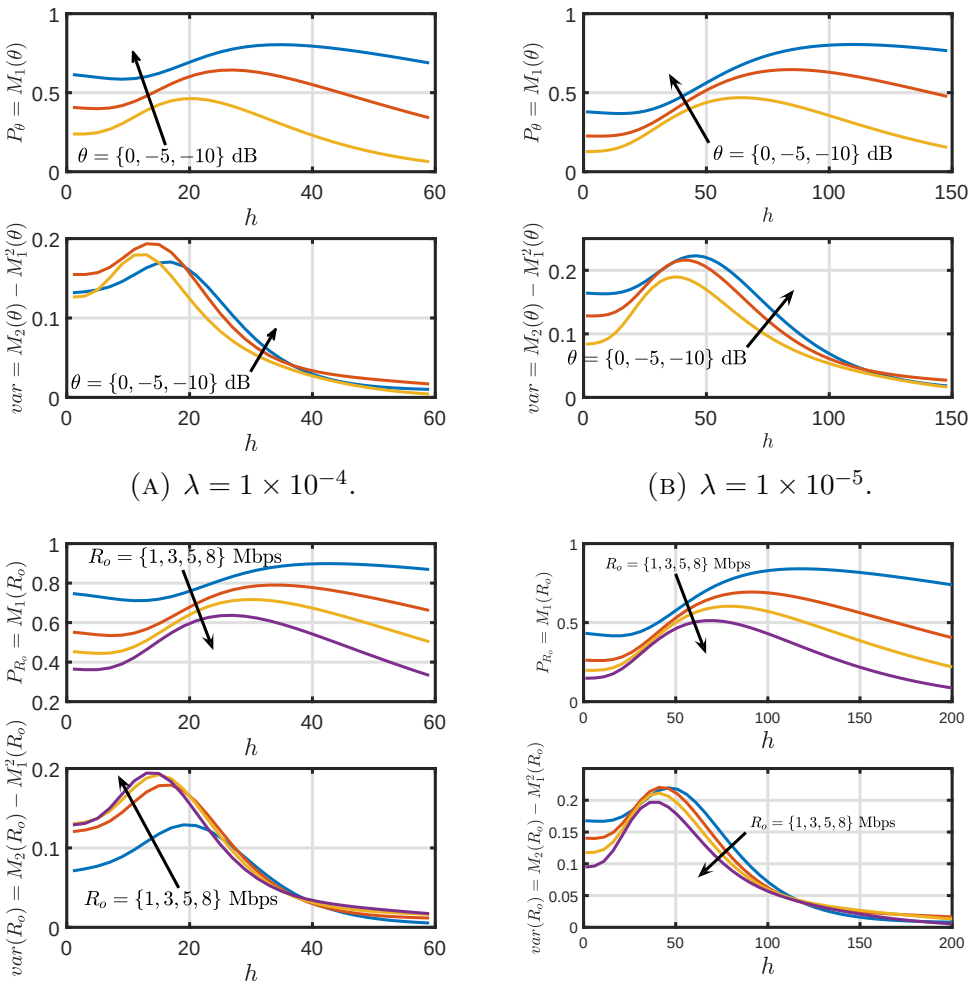

(A) $\lambda = 1 \times 10^{-4}$. (B) $\lambda = 1 \times 10^{-5}$.

(C) $\lambda = 1 \times 10^{-4}$. (D) $\lambda = 1 \times 10^{-5}$.

FIGURE 6.2: (A)+(B) Coverage probability and coverage variance. (C)+(D) Coverage rate probability and coverage rate variance. All for the UMi large-scale fading model, $W = 20$ MHz and $N_a = N_s = 1$.

the variance curves is much steeper for BS heights which are greater than the optimal height h^* that maximizes the first moment. That is, increasing h beyond h^* will slightly decrease P_θ and P_{R_o}, but it will decrease the variances more rapidly. Hence, the network operator may choose to sacrifice the optimal values of P_θ and P_{R_o} to gain more fairness for the users. For example, in Figure 6.2.(C) the height that maximizes P_{R_o} for $R_o = 8$ Mbps is around 25 meters which corresponds to a variance of 0.13. However, increasing the

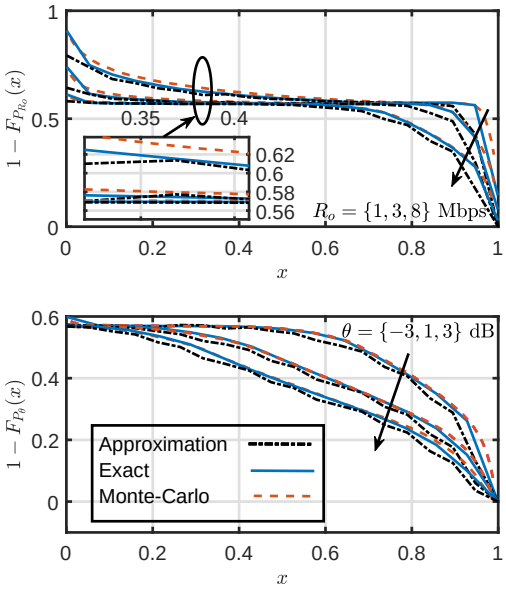

FIGURE 6.3: Meta-distribution of coverage rate probability (top) and meta-distribution for coverage probability (bottom). All for the UMi large-scale fading model, $W = 20$ MHz and $N_a = N_s = 1$.

height of the base station by 5 meters will result in a slight decrease in P_{R_o} by .05 and that will also decrease the variance to 0.07 which is approximately half of 0.13. That is, an additional 70% more users will gain the same optimal value of P_{R_o}. More clearly, this will increase the user's fairness over the entire network. However, this behaviour needs to be considered carefully due to the large number of parameters involved in the network radio access planning.

6.4.3 Evaluation of Meta-distribution and Optimal Bandwidth Partitioning

Figure 6.3 shows a comparison between the exact solution (see (6.15) and (6.15)), approximation (see (6.19) and (6.20)) and Monte-Carlo simulations for the meta-distribution. As seen from the plot, the approximation that we

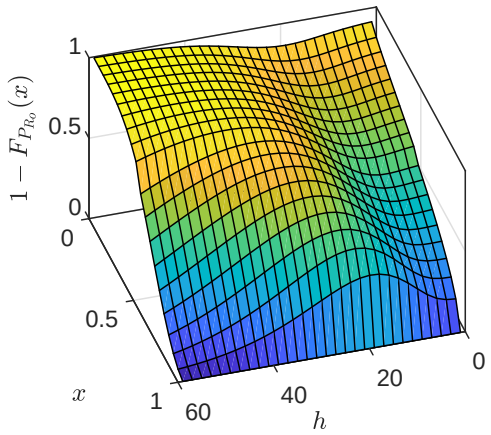

FIGURE 6.4: Meta-distribution for coverage rate for single tier network with $\lambda = 1 \times 10^{-4}$, $R_o = 3$ Mbps and $N_s = N_a = 1$.

used matches the exact solution and the Monte-Carlo simulation. The three bunches of curves are for different values of θ and R_o, but for the same system parameters and BSs density. As expected, the corresponding values of the meta-distribution are different for the three curves. This means that P_θ and P_{R_o} do not provide sufficient information about the network performance. For example, the values for the meta-distribution are $\bar{F}_{P_{\theta=-3\text{dB}}}(0.8) = 0.40$ while $\bar{F}_{P_{\theta=0\text{dB}}}(0.8) = 0.27$. That is, 13% less users at $\theta = 0$ dB QoS will not achieve the 0.8 coverage probability as compared to the value at $\theta = -3$ dB.

Another interesting point is that, with the optimal height deployment, the meta-distribution is less likely to have zero values and the curves are more likely to be flat. In some papers, the meta-distribution is approximated (using the first two or three moments) by the beta-distribution and the generalized beta-distribution [106]. But, this is not valid for our model and so it dramatically fails. This is due to the fact that the optimal height deployment is more favourable for the environmental conditions and results in more LoS links, in particular for the nearest neighbour association which flattens the curve and decreases the variance (i.e., more fairness between users - see [106] for more

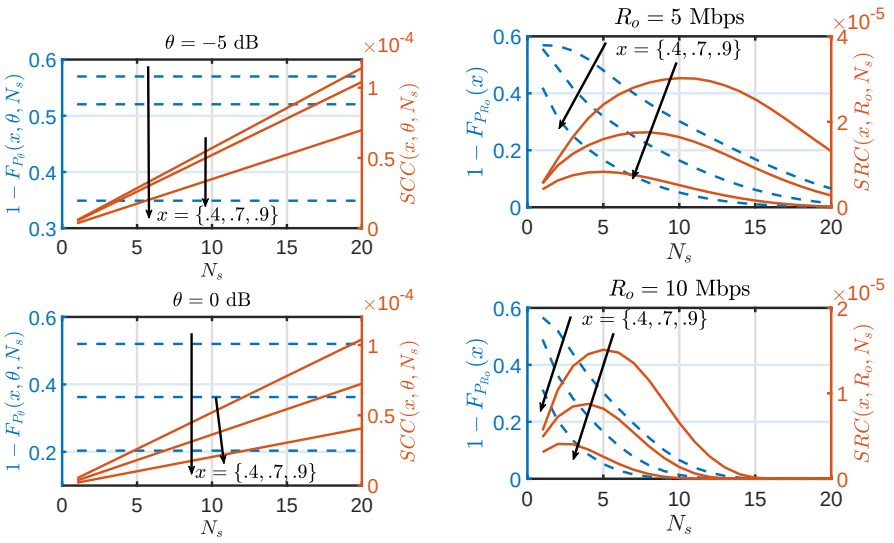

(A) (B)

FIGURE 6.5: (a) Meta-distribution (left axis- see (6.19)) and SCC (right axis - see (6.23)) against the number of channel partitions. (b) Meta-distribution (left axis- see (6.19)) and SRC (right axis - see (6.23)) against the number of channel partitions. All for UMi large-scale fading model, $W = 20$ MHz and for full-load cell $N_a = N_s$.

details). Hence, the two or three parameter distribution mapping like the beta-distribution and the generalized beta-distribution is not sufficient and this is why we have used Mnatsakanov's theorem as an approximation. Finally, Figure 6.4 shows the effect of changing the BSs height on the meta-distribution. As shown in this figure, for any arbitrarily chosen value of x, there is an optimal height at which the meta-distribution will be maximized. This is valid for both $\bar{F}_{P_\theta}(x)$ and $\bar{F}_{P_{R_o}}(x)$.

Figure 6.5 shows the meta-distributions ($\bar{F}_{P_\theta}(x)$ and $\bar{F}_{P_{R_o}}(x)$) and the spatial capacities $SCC(x, \theta, N_s = N_a)$ and $SRC(x, R_o, N_s = N_a)$. An interesting point about the full-load SRC is that for any arbitrarily chosen value of reliability x, there is an optimal number of channel partitions N_s that max-

imizes the SRC. This optimal N_s varies with the desired rate threshold R_o. For example, for $x = 0.4$ and $R_o = 5$ Mbps, the optimal number of channel partitions for the full-load capacity is $N_s = N_a = 10$ and the density of users who achieve R_o is 3×10^{-5} while for $N_s = 18$ there are 33% less users who achieve the same R_o. As clearly shown in the figure, this optimal number of partitions selections is only valid when studying the SRC and it is not valid for the SCC where there are no optimal values for N_s. This is due to the fact that the effective rate is dependent on the number of channel partitions and is a logarithmic function of the SIR while the standard coverage probability is not.

6.5 Conclusion

In this chapter, we highlighted some important aspects of the design for the radio access of the ultra-dense and traditional cellular networks. We gave expressions to quantify the coverage probability and the coverage rate probability. For the sake of better characterization of the network performance, we evaluated the higher-order moments for both the coverage probability and coverage rate probability. As a result of the higher-order moments, we quantified the meta-distribution to characterize the users' fairness experience using the exact solution of Gil-Pelaez and also Mnatsakanov's theorem for an accurate approximation. Using the evaluated performance metrics, we studied the impact of changing any of the main system model parameters on the overall performance of the network. As the main result, we showed that both the partitioning factor of the channel and the BS height play very important roles in optimizing the network performance. Finally, for a future extension, we

will study the same performance metrics for a multi-tier, user-centric heterogeneous network.

Chapter 7

Drone-Assisted Backscatter Communication for IoT Sensor Network

Contents

In this chapter, we develop a comprehensive framework to characterize the performance of a drone-assisted backscatter communication-based Internet of Things (IoT) sensor network. We consider a scenario where the drone transmits an RF carrier that is modulated by IoT sensor node (SN) to transmit its data. The SN implements load modulation which results in amplitude shift keying (ASK) type modulation for the impinging RF carrier. In order to quantify the performance of the considered network, we characterize the coverage probability for the ground based SN node. The statistical framework developed to quantify the coverage probability explicitly accommodates a dyadic backscatter channel which experiences deeper fades than that of the one-way Rayleigh channel. Our model also incorporates Line of Sight (LoS) and Non-LoS (NLoS) propagation states for accurately modelling large-scale path-loss between drone and SN. We consider spatially distributed SNs which can be modelled using a spatial Binomial Point Process (BPP). We practically implement the proposed system using Software Defined Radio (SDR) and a custom designed SN tag. The measurements of parameters such as noise figure, tag reflection coefficient etc., are used to parametrize the developed framework. Lastly, we demonstrate that there exists an optimal set of parameters which maximizes the coverage probability for the SN.

7.1 Introduction

The number of connected consumer electronic devices has exponentially increased over the past few years. According to recent statistics [113], there are already 19.4 billion internet connected devices that are in use across the globe, with the number of Internet-of-Things (IoT) devices currently around 8.3 billion. The number of IoT devices is expected to increase at a startling compound annual growth rate (CAGR) of 10%. With such a massive volume of devices, it is becoming increasingly important to explore energy efficient (EE) IoT Sensor Node (SN) design. This is mainly motivated by the fact that recharging the deployed SNs individually on a regular basis might be impractical, especially for those SNs which have limited post-deployment accessibility.

To realize EE design for IoT SNs, there are two possible avenues which have gained significant interest from the research community: (i) developing energy optimal protocols/architecture for communication; (ii) harvesting energy from ambient natural/synthetic sources to power the communication hardware. In the recent past [114], there has been a significant interest in simultaneous wireless power and information transfer (SWIPT) based SN design. The SWIPT techniques employ a rectenna, i.e., an antenna and a diode to charge an on board energy storage component (such as a battery or a super-capacitor). The harvested power is in turn employed for provisioning communication between the SN and the intended access point (AP). The key limitation of SWIPT is that the harvested power is very small and the RF signals which are optimal for energy harvesting are not necessarily optimal for communication.

RF Backscatter based communication [115–118] presents an attractive

alternative. Backscatter radio communication does not require expensive active components such as as RF oscillators, mixers, crystals, decoupling capacitors, etc. The SNs communicate with the AP (also called the Reader) by modulating the ambient un-modulated RF carrier which is transmitted by the AP. The RF carrier modulation is achieved by connecting an antenna to different loads which translates into different antenna-load reflection coefficients. Interested readers are directed to [113] for a recent tutorial which provides a comprehensive coverage of the backscatter based SN design. RF backscatter based IoT SNs are particularly well suited for applications where periodic polling can be employed for SN data aggregation/collection. In other words, the data collection can be duty cycled by the reader in an adaptive manner. This is particularly useful in multi-modal sensing where certain knowledge at the reader can be employed to increase/decrease the duty cycle of data collection. For instance, in smart agriculture application, weather data can be exploited to duty cycle the collection of reading from soil moisture sensors. RF backscatter based IoT SNs are particularly well suited to environmental monitoring applications where SNs are spread across a wider geographical region. Our prime interest in RF backscatter based SNs is in the context of smart agriculture where such sensors can provide wide scale deployment at a very low cost. In practice, it is possible to print these sensors (either using conductive ink on paper or on the semiconductor substrate) and mount a single chip to implement a SN node. Some initial investigations on backscatter based SNs for soil moisture monitoring are conducted in [117, 119–121].

The key issue with the traditional approaches is that the coverage range for RF backscatter based SNs is only of the order of few hundred meters at best. Consequently, a dense deployment of readers is required for provisioning data collection which is costly, as this requires not only more hardware

but also post-deployment maintenance. A simple solution would be to use a single RF reader which is mounted on a mobile platform which can navigate the intended monitoring area. Drones present an attractive choice for mounting the backscattering reader as several farmers are using drones for various other agricultural monitoring functions. For instance, multi-spectral cameras mounted on drones are being used to calculate vegetation indices (for instance normalized differential vegetation index (NDVI)) which highlight a particular characteristic of vegetation. To this end, this chapter explores the performance of RF Backscatter based IoT SNs with a Drone mounted Flying Reader (DFR).

7.1.1 Contributions

In order to fully understand the networking dynamics of a backscatter based IoT SN served by the DFR, it is essential to characterize both the link and the network level performance of such deployments. To this end, in this chapter:

1. We aim to develop a comprehensive statistical framework to characterize the performance of the considered IoT SN. To the best of our knowledge this is the first study which presents such a statistical framework to characterize the performance of drone assisted backscatter based IoT SNs.

2. The performance of SNs is measured and quantified in terms of the well known coverage probability metric. The coverage probability is defined as the probability that the received signal-to-noise-ratio (SNR) exceeds a certain desired threshold. The threshold can easily be selected to sat-

isfy a certain desired bit-error-rate (BER), i.e. coverage probability can essentially serve as a proxy for the successful packet decoding probability.

3. The framework presented in this chapter implicitly incorporates realistic propagation dynamics of communication between DFR and SNs by: (i) employing the large-scale path-loss model which accommodates both Line-of-Sight (LoS) and Non-LoS (NLoS) link states; and (ii) by employing the small-scale fading model which captures the dyadic nature of backscatter communication, i.e., forward propagation (from DFR-to-SN) and backward propagation (SN-to-DFR) may experience non-zero correlation[1].

4. Due to a dyadic Rayleigh fading channel, it is difficult to analyse the performance of randomly scattered SNs[2]. However, we present alternative closed-form expressions which are amenable to analysis.

5. We practically implement a tag and software-defined radio (SDR) based reader and parametrize the developed framework to investigate the coverage performance of SNs. Lastly, the impact of various parametric variations and optimal dimensioning of the network is briefly explored.

7.1.2 Organization

The rest of the chapter is organized as follows: Section 7.2 introduces the system model and deployment geometry of the network. Section 7.3 gives the performance analysis and mathematical modelling. Section 7.4 presents

[1]Notice that due to dyadic fading channel, the analysis of performance is different from the scenario in [52, 54] where a drone is used as a BS.

[2]We borrow tools from stochastic geometry for analysis. The interested reader is directed to [99] for a comprehensive tutorial.

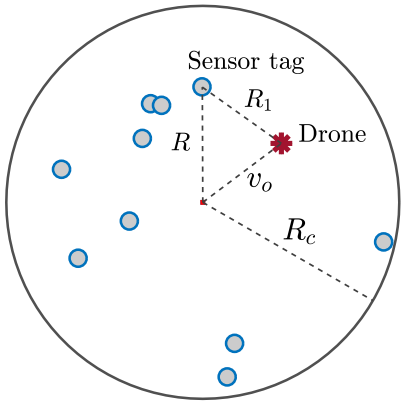

FIGURE 7.1: Drone-assisted smart IoT agriculture geometry. A snapshot of the distribution of 10 sensor tags on the circular area of a radius R_c.

numerical results. Finally, Section 7.5 provides some future work and conclusions.

7.2 System Model

7.2.1 Spatial and Network Models

As depicted in Figure 7.1, we consider a scenario where a drone is employed for data aggregation from SN tags. The drone is furnished with a mono-static SN tag reader and is tasked to cover a desired service area which is modelled by a disc of radius R_c. It is assumed that SN tags are uniformly distributed in the intended service area. The reader does not possess any prior knowledge about the tag location and randomly moves across the area such that its reference distance to the centre of the disc is v_o[3]. Assuming that the number of SNs is

[3]For a randomly chosen point inside the circular coverage area, v_o is no longer constant and is indeed a random variable, say V_o with PDF given by $f_{V_o}(v_o) = \frac{2v_o}{R_c^2}$, for $v_o \in [0, R_c]$.

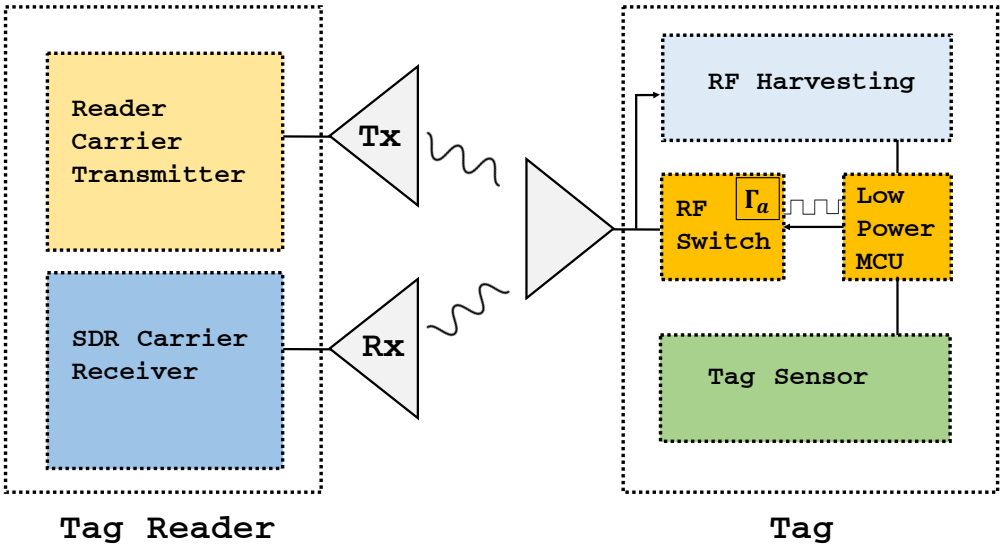

FIGURE 7.2: Architecture of backscatter DFR and SN.

finite and fixed, the spatial distribution of the SNs is captured by a binomial point process (BPP) such that [61]:

$$\Phi = \{\mathbf{x_0}, \mathbf{x_1}, ..., \mathbf{x_{N_s}}, \forall\ \mathbf{x}_i \in \mathbb{R}^2\}, \tag{7.1}$$

where N_s is the number of tags on the two dimensional set space. At a particular time instance, only one SN is served on a particular resource channel to avoid co-channel interference. The sensor at the location $\mathbf{x_i}$ is associated to the nearest neighbour flying drone reader.

7.2.2 SN Tag and DFR's SDR Implementation

The backscattering SN tag reflects the ambient RF carrier transmitted by the DFR by modulating the antenna's reflection coefficient. This is simply achieved by connecting the antenna to two different loads (one for information

bit '0' and the other for information bit '1'). In our SN design, the load modulation is driven by the serial payload data packets generated by the ultra-low power microcontroller unit (MCU). Either MSP430 from Texas Instrument or STM32L063R8 ARM M0+ are suitable as their power-consumption is only several μA in different modes. In our reference implementation the tag charges a super-capacitor by harvesting energy from an RF carrier. The harvested power is used to drive the SN MCU. In a nutshell, our load modulation scheme translates to amplitude shift keying (ASK). We associate the higher tag's antenna reflection coefficient Γ_a to the binary logic '0' and design a circuit which tries to minimize the reflection coefficient for binary logic '1' (i.e., no reflected carrier for the 1 binary logic). Hence, if the binary logic '1' has a reflection coefficient $\Gamma_a = 0$, the resulting tag transmit signal can be written as [116]:

$$x_{Tag}(t) = \begin{cases} \Gamma_a b_n(t - nT), & \text{Logic 0,} \\ 0, & \text{Logic 1,} \end{cases} \tag{7.2}$$

for $t \in [nT, (n+1)T]$, where $b_n(t - nT)$ is the information bit of a duration T. Figure 7.3 depicts the reception and decoding of a serial data with the payload word "OK" in our reference implementation. The carrier is generated by the Nuand BladeRF SDR transceiver with the transmit power of 14 dBm. The bottom blue waveform presents the received modulated carrier with a bit rate of 2.4 kbps. As we can see, the reflection coefficient effects the distance between the two binary levels of the modulated carrier and this directly effects the choice of constellation size[4] and the likelihood of correct demodulation, i.e., the bit error rate of the communication link. The red bit sequence is the decoded bits after performing level detection on the bandpass received RF

[4]It is envisioned that higher-order modulation can be implemented by employing cascaded RF switches.

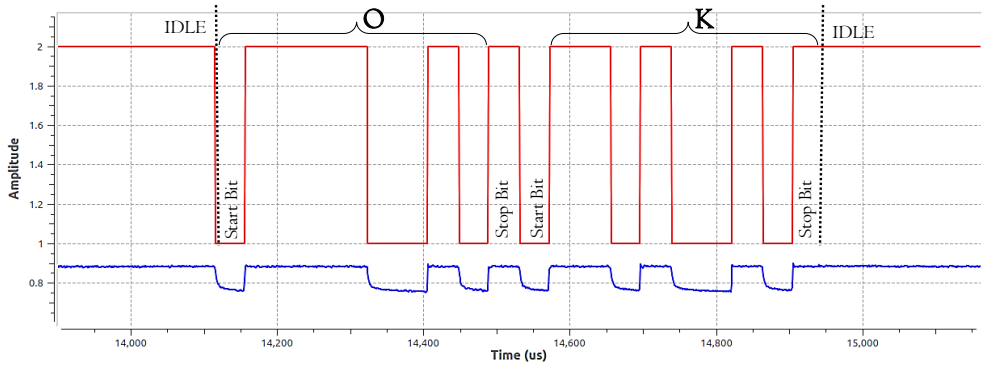

FIGURE 7.3: Backscatter transmission of the serial data for the word "OK" which is equivalent to the hexadecimal representation of "0x4F,0x4B" from a sensor node tag. The lower curve is the ASK modulated carrier at the reader antenna. Serial data bit rate is 2.4 kbps.

signal and then recovering the clock utilizing a Mueller-Müller timing recovery scheme [122].

7.2.3 Propagation Model

Large-Scale Fading Model:

In order to accurately capture the propagation conditions for drone assisted backscatter communication, we employ the path-loss model presented in [12]. The backscatter communication link is dyadic in nature, i.e., it is characterized by the product of forward (DFR-to-SN) and backward (SN-to-DFR) channel gains. We assume both forward and backward channels experience the same path-loss, which is reasonable for the mono-static architecture. The employed path-loss model adequately captures LoS and NLoS contributions for drone-to-ground communication as follows:

$$L_{LoS}(h_d, r) = K_{LoS}\left(r^2 + h_d^2\right), \tag{7.3}$$

$$L_{NLoS}(h_d, r) = K_{NLoS}\big(r^2 + h_d^2\big), \tag{7.4}$$

where h_d is the height of the drone in meters, r is the two dimensional projection separation between the drone and the SN, K_{LoS} and K_{NLoS} are environment and frequency dependent parameters such that $K_i = \zeta_i \left(c/(4\pi f_{MHz})\right)^{-1}$, ζ_i is the excess path-loss for $i \in \{LoS, NLoS\}$ with typical values for urban areas $\zeta_{LoS} = 1$ dB. The probabilities of having a LoS and NLoS link between the DFR and the desired SN are as follows:

$$\mathcal{P}_{LoS}(h_d, r) = \frac{1}{1 + a_1\, \mathrm{e}^{-b_1\eta\, \tan^{-1}\left(\frac{r}{h_d}\right) + b_1\, a_1}}, \tag{7.5a}$$

$$\mathcal{P}_{NLoS}(h_d, r) = 1 - \mathcal{P}_{LoS}(h_d, r), \tag{7.5b}$$

where a_1, b_1, c_1 are environment dependent constants, $c_1 = 180/\pi$ and θ is the elevation angle in degrees.

Small-Scale Dyadic Rayleigh Fading Channel

We consider a mono-static backscattering DFR where both transmit and receive antennas are co-located as shown in Figure 7.2. The DFR transmits an unmodulated RF carrier and the SN tag reflects it back with a reflection coefficient of Γ_a. Both forward ($\mathcal{G}_f$) and backward ($\mathcal{G}_b$) propagation channels suffer from Rayleigh flat fading. However, due to the dyadic nature of the link, the channels have non-zero correlation captured by the parameter $\rho = \mathbb{E}(\mathcal{G}_f, \mathcal{G}_b)$ with $\mathcal{G}_f, \mathcal{G}_b \sim \mathcal{CN}(0, 1)$. The received channel power gain is given by $\mathcal{H}_f = |\mathcal{G}_f|^2$ and $\mathcal{H}_b = |\mathcal{G}_b|^2$ and has the joint distribution as:

$$f_{\mathcal{H}_f, \mathcal{H}_b}(h_f, h_f; \rho) \;=\; \frac{2}{\tilde{\rho}\sigma_f^2\sigma_b^2} \exp\left(-\frac{1}{\tilde{\rho}}\left[\frac{h_f}{\sigma_f^2} + \frac{h_b}{\sigma_b^2}\right]\right) \times \mathcal{I}_o\left(\frac{\rho\sqrt{h_f h_b}}{(1-\rho^2)\sigma_f^2\sigma_b^2}\right),$$

where $\mathcal{I}_o(z) = \frac{1}{\pi}\int_0^{\pi} \exp\left(-z\cos(t)\right) \mathrm{d}t$, is the modified Bessel function of first kind and zero order, $\tilde{\rho} = 1 - \rho^2$ and σ_f^2 and σ_b^2 are the variances of $\mathcal{G}_f$ and $\mathcal{G}_b$ respectively. The PDF of the equivalent dyadic fading channel coefficient $\mathcal{H} = \mathcal{H}_f\mathcal{H}_b$ can be written as

$$f_{\mathcal{H}}(h,\rho) = \frac{1}{2\tilde{\rho}\sigma_f^2\sigma_b^2}\mathcal{I}_o\left(\frac{\rho\sqrt{h}}{\tilde{\rho}\sigma_f\sigma_b}\right)\mathcal{K}_o\left(\frac{\rho\sqrt{h}}{\tilde{\rho}\sigma_f\sigma_b}\right), \tag{7.6}$$

where $\mathcal{K}_o(z) = \int_0^{\infty} \cos(z\sinh(t))\,\mathrm{d}t$, is the modified Bessel function of second kind and zero order. The PDF in (7.6) can be simplified as both forward and backward Rayleigh channels have unit mean, i.e., $\mathbb{E}(\mathcal{H}_f) = \mathbb{E}(\mathcal{H}_b) = 1$:

$$f_{\mathcal{H}}(h,\rho) = \frac{2}{\tilde{\rho}}\mathcal{I}_o\left(\frac{2\rho\sqrt{h}}{\tilde{\rho}}\right)\mathcal{K}_o\left(\frac{2\rho\sqrt{h}}{\tilde{\rho}}\right). \tag{7.7}$$

Obtaining a CDF for (7.7) which is required for the coverage analysis is quite complicated and mathematically intractable. Hence, we develop an alternative performance characterization framework by developing a tight approximation for the PDF in (7.7). In fact, (7.7) is a monotonically decreasing product of two modified Bessel functions in the interval $\mathcal{H} \in (0,\infty)$ as demonstrated in [123]. Moreover, the product decreases exponentially fast. Clearly, this motivates approximation of the PDF by using asymptotic expressions for Bessel functions. The asymptotic Hankels expansion of the Bessel functions $\mathcal{I}_o(z)$ and $\mathcal{K}_o(z)$ are given as:

$$\mathcal{K}_o(z) \approx \frac{\sqrt{\pi}}{2}\exp\left(-z\right), \tag{7.8}$$

$$\mathcal{I}_o(z) \approx \frac{1}{z\sqrt{2\pi}}\exp\left(z\right). \tag{7.9}$$

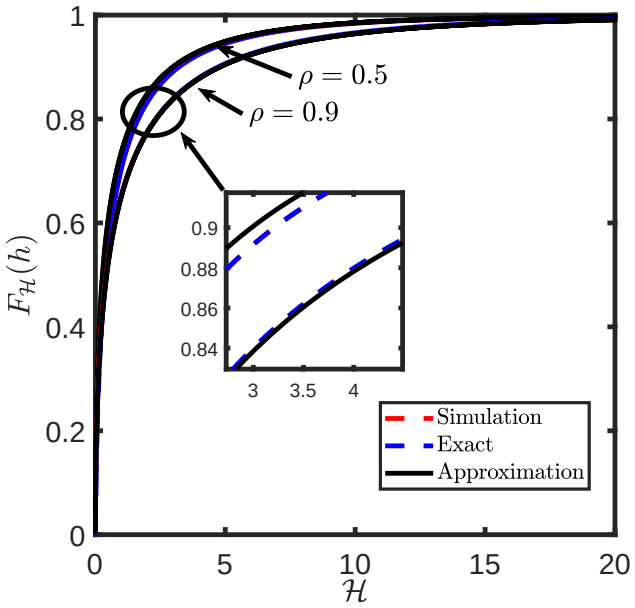

FIGURE 7.4: Cumulative distribution function for the backscatter dyadic fading channel coefficient $\mathcal{H}$.

Substituting the above to obtain $\tilde{f}_{\mathcal{H}}(h)$ and normalizing the result with the factor $c = \int_0^\infty \tilde{f}_{\mathcal{H}}(h)\,\mathrm{d}h$, we can write the approximate PDF and CDF as:

$$\text{PDF:} \quad f_{\mathcal{H}}(h,\rho) \approx \frac{h^{-\frac{1}{2}}}{2\sqrt{\rho}} \exp\left(-\frac{2(1-\rho)\sqrt{h}}{1-\rho^2}\right) \tag{7.10}$$

$$\text{CDF:} \quad F_{\mathcal{H}}(h,\rho) \approx 1 - \exp\left(-\frac{2(1-\rho)\sqrt{h}}{1-\rho^2}\right). \tag{7.11}$$

Figure 7.4 presents the tightness of the derived approximation in (7.11). It is evident that the approximation is very tight especially for high values of the correlation coefficient ρ. Combining large-scale and small-scale fading models the overall propagation channel is given by $\mathcal{H}L(h_d,r)^{-2}$ with $\mathcal{H} = \mathcal{H}_f\mathcal{H}_b$ and $L(h_d,r) = L_{LoS}(h_d,r)\mathcal{P}_{LoS}(h_d,r) + L_{NLoS}(h_d,r)\mathcal{P}_{NLoS}(h_d,r)$.

7.3 Performance Analysis

7.3.1 Link Distance Analysis

In this section, we characterize link distance distributions which are required to quantify the large-scale path-loss given by (7.3). These distributions are employed to quantify coverage probability in section 7.3.2. The PDF for the distance R from the DFR (located at distance v_o from the center of coverage region) to an arbitrary SN tag can be written as in (7.13). Employing the derived PDF with order-statistics enables derivation of the PDF of the distance to the nearest SN from the DFR denoted by R_1 as summarized in the following proposition.

Proposition 7.1

The PDF of the distance R_1 from the DFR (at a distance v_o from the centre of the intended coverage area) to the nearest SN tag can be evaluated as follows:

$$f_{R_1}(r_1|v_o,R_c)=\begin{cases} f^{(1)}_{R_1}(r_1|v_o,R_c)=\frac{2N_s r_1}{R_c^2}\left(1-\frac{r_1^2}{R_c^2}\right)^{N_s-1}, & 0\le r_1\le R_c-v_o \\ f^{(2)}_{R_1}(r_1|v_o,R_c)=\frac{2N_s r_1}{\pi R_c^2}\arccos\left(\frac{r_1^2+v_o^2-R_c^2}{2v_o r_1}\right) & \\ \quad\times\left(1-\left(\frac{r_1^2}{\pi R_c^2}\left(\theta_1^1-\frac{1}{2}\sin\left(2\,\theta_1^1\right)\right)\right.\right. & \\ \quad\left.\left.+\frac{1}{\pi}\left(\theta_2^1-\frac{1}{2}\sin\left(2\,\theta_2^1\right)\right)\right)\right)^{N_s-1}, & R_c-v_o<r_1\le R_c+v_o, \end{cases} \tag{7.12}$$

with $\theta_1^1=\arccos\left(\frac{{r_1}^2-R_c^2+v_o}{2v_o r_1}\right)$ and $\theta_2^1=\arccos\left(\frac{-{r_1}^2+R_c^2+v_o}{2v_o R_c}\right)$.

Proof. Let N_s tags be distributed uniformly on a disk of radius R_c. Then

the derivation of the nearest neighbour distribution amongst the N_s SN tags follows the order statistics using the fact that for general N_s i.i.d random variables $Z_i \in \{Z_1, Z_2, ..., Z_{N_s}\}$ with PDFs $f_{Z_i}(z)$ ordered in ascending order, then the PDF of $Z_1 = \min_i(Z_i)$ can be written as $f_{Z_1}(z) = N\left(1 - F_{Z_i}(z)\right)^{N-1} f_{Z_i}(z)$ [93]. Then, by applying

$$f_R(r|v_o, R_c) = \begin{cases} f_R^{(1)}(r|v_o, R_c) = \frac{2r}{R_c^2}, & 0 \leq r \leq R_c - v_o, \\ f_R^{(2)}(r|v_o, R_c) = \frac{2r}{\pi R_c^2} \arccos\left(\frac{r^2+v_o^2-R_c^2}{2v_o r}\right), & R_c - v_o < r \leq R_c + v_o, \end{cases} \tag{7.13}$$

with the CDF as follows:

$$F_R(r|v_o) = \begin{cases} F_R^{(1)}(r|v_o) = \frac{r^2}{R_c^2}, & 0 \leq r \leq R_c - v_o, \\ F_R^{(2)}(r|v_o) = \frac{r^2}{\pi R_c^2}\left(\theta_1 - \frac{1}{2}\sin(2\theta_1)\right) + \\ \qquad \frac{1}{\pi}\left(\theta_2 - \frac{1}{2}\sin(2\theta_2)\right), & R_c - v_o < r \leq R_c + v_o, \end{cases} \tag{7.14}$$

with $\theta_1 = \arccos\left(\frac{r^2-R_c^2+v_o}{2v_o r}\right)$ and $\theta_2 = \arccos\left(\frac{-r^2+R_c^2+v_o}{2v_o R_c}\right)$, we can write the PDF of the distance R_1 as

$$f_{R_1}(r_1|v_o, R_c) = \begin{cases} f_{R_1}^{(1)}(r_1|v_o, R_c), & 0 \leq r_1 \leq R_c - v_o, \\ f_{R_1}^{(2)}(r_1|v_o, R_c), & R_c - v_o < r_1 \leq R_c + v_o, \end{cases} \tag{7.15}$$

where

$$f_{R_1}^{(1)}(r_1|v_o, R_c) = N_s(1 - F_R^{(1)}(r_1|v_o))^{N_s-1} f_R^{(1)}(r_1|v_o), \tag{7.16}$$

$$f_{R_1}^{(2)}(r_1|v_o, R_c) = N_s(1 - F_R^{(2)}(r|v_o))^{N_s-1} f_R^{(2)}(r_1|v_o). \tag{7.17}$$

□

From the previous proposition we can easily integrate $f_{R_1}(r_1|v_o, R_c)$ in (7.12) to get the CDF of the nearest neighbour distance distribution as

$$F_{R_1}(r_1|v_o, R_c) = \begin{cases} (1 - F_R^{(1)}(r_1|v_o, R_c))^{N_s}, & 0 \leq r \leq R_c - v_o, \\ (1 - F_R^{(2)}(r_1|v_o, R_c))^{N_s}, & R_c - v_o < r \leq R_c + v_o. \end{cases} \tag{7.18}$$

7.3.2 Coverage Probability

The coverage probability is defined as the probability that the SNR will be greater than a certain predefined value β. The average SNR for the uplink DFR can be quantified as:

$$\begin{aligned} \text{SNR} \quad &= \underbrace{\frac{P_t \mathcal{H}_f \mathcal{H}_b \Gamma_a [L_{LoS}(r_1)]^{-2}}{\sigma_N^2} \mathcal{P}_{LoS}(r_1)}_{\text{SNR}_L} \\ &+ \underbrace{\frac{P_t \mathcal{H}_f \mathcal{H}_b \Gamma_a [L_{NLoS}(r_1)]^{-2}}{\sigma_N^2} \mathcal{P}_{NLoS}(r_1)}_{\text{SNR}_{NL}}, \end{aligned} \tag{7.19}$$

where P_t is the reader's transmit power, σ_N^2 is the additive white Gaussian noise (AWGN) power, SNR_L is the SNR when there is a LoS link between the user and the BS and SNR_{NL} is the SNR when there is a NLoS link between the user and the DFR. The coverage probability for any arbitrary mobile user can be evaluated as in the following theorem.

Proposition 7.2 ► (Coverage probability)

The coverage probability for any BPP with N_s SNs in the presence of AWGN can be evaluated as:

$$\begin{aligned} P_c(\beta|v_o) &= \int_0^{R_c-v_0} f_{R_1}^{(1)}(r_1|v_o,R_c)\Big[\left[1-F_{\mathcal{H}}(\zeta_1,\rho)\right]\mathcal{P}_L(r_1) \\ &\qquad + \left[1-F_{\mathcal{H}}(\zeta_1,\rho)\right]\mathcal{P}_{NL}(r_1)\Big]\,\mathrm{d}r_1 \\ &+ \int_{R_c-v_0}^{R_c+v_0} f_{R_1}^{(2)}(r_1|v_o,R_c)\Big[\left[1-F_{\mathcal{H}}(\zeta_2,\rho)\right]\mathcal{P}_L(r_1) \\ &\qquad + \left[1-F_{\mathcal{H}}(\zeta_2,\rho)\right]\mathcal{P}_{NL}(r_1)Big]\,\mathrm{d}r_1, \end{aligned} \tag{7.20}$$

with $\zeta_1 = \beta\sigma_N^2[L_L(r_1)]^2/P_t\Gamma_a$ and $\zeta_2 = \beta\sigma_N^2[L_{NL}(r_1)]^2/P_t\Gamma_a$.

Proof. For a pre-defined threshold β of SNR, then the coverage probability can be defined as

$$\begin{aligned} P_c(\beta|v_o) &= \mathrm{P_r}[\mathrm{SNR}\geq\beta], \\ &= \mathbb{E}_{r_1}\left[1-F_{\mathcal{H}}(\beta\sigma_N^2[L_L(r_1)]^2/P_t\Gamma_a,\rho)\right]\mathcal{P}_L(r_1) \\ &+ \mathbb{E}_{r_1}\left[1-F_{\mathcal{H}}(\beta\sigma_N^2[L_{NL}(r_1)]^2/P_t\Gamma_a,\rho)\right]\mathcal{P}_{NL}(r_1). \end{aligned} \tag{7.21}$$

Hence, by evaluating the averaging operator in (7.21) with the distribution of R_1 in (7.12), we can quantify the coverage probability as shown in (7.20). □

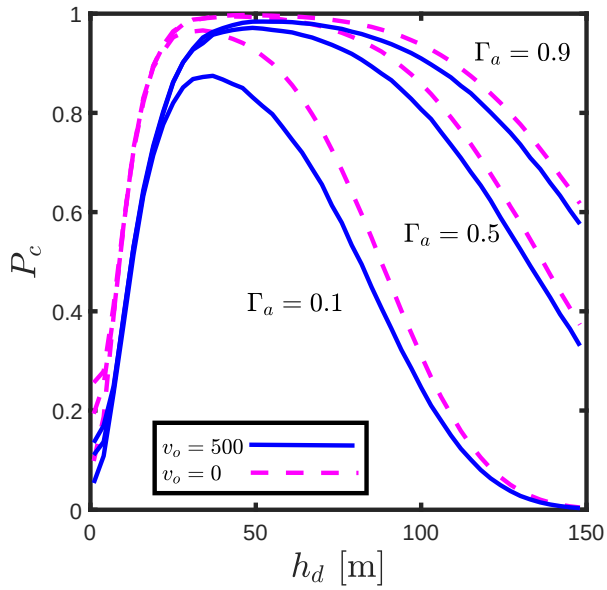

FIGURE 7.5: Coverage probability. $N_s = 200$, $R_c = 500$, $\rho = .5$, $\sigma^2 = -110$ dBm, $\beta = 10$ dBm.

7.4 Results and Discussion

In this section, we validate the developed statistical framework for quantifying the coverage probability. We also briefly explore the impact of different parametric variations on the coverage probability. We assume a rural environment with the parameters $a_1 = 9.6$, $b_1 = 0.28$ for the path-loss model (see Section 2), noise power $\sigma_N^2 = 110$ dBm, $P_t = 0$ dB and $f = 868$ MHz illuminator carrier frequency. Also, as described in the previous sections, we consider wireless, Rayleigh flat-fading correlated channels. The noise power is estimated from the practical implementation of the system as described in Section 7.2.2.

Figure 7.5 shows the coverage probability P_c versus the DFR height h_d for different tag reflection coefficient Γ_a and different reference locations (v_o) of the drone inside the coverage area. The Figure shows that, for certain

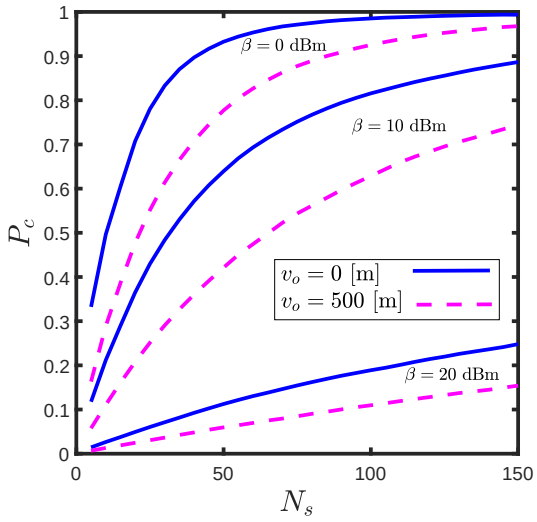

FIGURE 7.6: Coverage probability. $R_c = 500$, $\rho = .5$, $\sigma^2 = -110$ dBm, $\Gamma = 0.9$

deployment parameters, there is always an optimal height of the DFR that maximizes the coverage probability and this optimal height changes with the change in the location of drone, i.e., with the change in v_o. For example, at $v_o = 0$ and $\Gamma_a = 0.9$, the optimal drone height is in the range of $40 - 60$ meters while for $v_o = 500$ and $\Gamma_a = 0.9$, the optimal height is lower in the range of $50 - 60$ meters. An interesting observation that follows Figure 7.5 is that the range of heights which optimize the coverage widens with increase in the reflection coefficient Γ_a. Moreover, the decrease in the coverage probability with the increase in DFR altitude (beyond optimal operational altitude) is much slower for a higher reflection coefficient. Consequently, when the reflection coefficient of the tag is appropriately designed optimal height can be reduced while concurrently the SN coverage probability can be maximized.

Figure 7.6 studies coverage against increasing number of deployed SNs for different values of β. The figure shows that, as we increase the number of the deployed SNs, the coverage probability will increase. This is due to the change of the characteristics of the nearest neighbour SN distance distribution

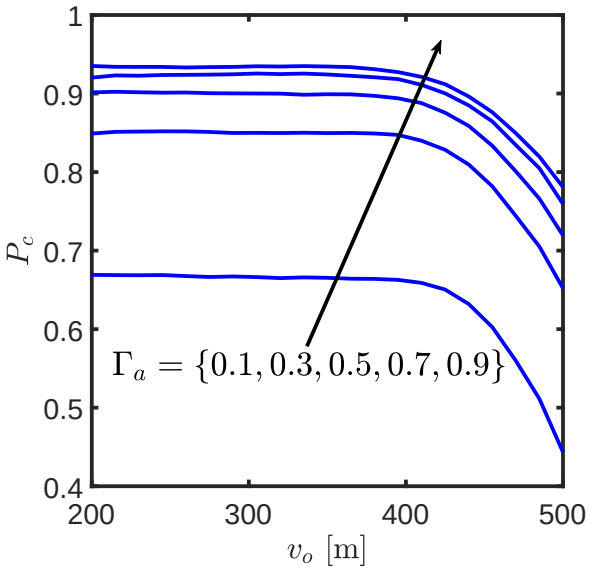

FIGURE 7.7: Coverage probability. $h_d = 50$ [m], $N_s = 50$, $R_c = 500$, $\rho = .5$, $\sigma^2 = -110$ dBm, $\beta = 0$ dBm.

(i.e., the distance to the nearest neighbour SN becomes lower and hence the path-loss decreases). However, this is only true if the SNs do not interfere with each other, i.e., by employing a highly directional antenna at the DFR. In practice, the increasing number of SNs contribute to co-channel interference and therefore reduce coverage probability.

Figure 7.7 shows the coverage probability against the DFR distance v_o from the center of the coverage area. As we described before, the coverage probability decreases as the DFR comes closer to the border of the circular coverage area. This is due to the BPP non-stationarity (i.e., the distance distributions and void probability characteristics are not the same for any arbitrary chosen point). Lastly, Figure 7.8 investigates the effect of jointly changing the height of the DFR and the number of SNs on the coverage probability. The Figure shows that for any chosen number of SNs, there is always a DFR height that maximizes the coverage probability.

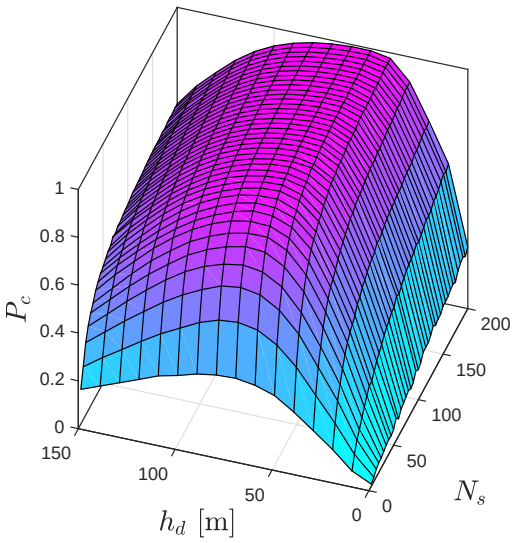

FIGURE 7.8: Coverage probability. $R_c = 500$, $\rho = .5$, $\sigma_N^2 = -110$ dBm, $\beta = 0$ dBm, $\Gamma_a = 0.9$

7.5 Conclusion

In this chapter, we investigated the design space of backscatter IoT SNs which are polled via a drone based SN tag reader. We developed a point-to-point implementation using SDR and a custom designed SN tag. We then developed a comprehensive statistical framework to quantify link level performance of randomly distributed SNs. Our model explicitly incorporates dyadic fading channel whereby forward (Drone-to-SN) and backward (SN-to-Drone) propagation channels can experience non-zero correlation. Performance analysis for a dyadic fading channel is intricate due to the nature of the PDF expressions. We present closed-form tight approximations which simplify the analysis. Our analytical model also incorporates LoS and NLoS components which characterize the path-loss for drone based communication. The developed model is parametrized by the experimental implementation and the impact of differ-

ent parameters on the coverage performance of the SN is investigated. We demonstrated that there exists a fruitful interplay between the SN's reflection coefficient, drone height and the number of SNs which jointly dictate an optimal operation point at which coverage probability is maximized.

Chapter 8

Conclusions and Future Work

Contents

In this chapter, we review the main results of this thesis and highlight the important conclusions. Additionally, we present the possible extensions and future directions of our work.

8.1 Conclusions

In this thesis, we addressed various scenarios where drones can be used to assist a general purpose communication network. We showed how drone empowered networks can be utilized to enable the key features of the smart-cities. By borrowing tools from stochastic geometry, we gave a comprehensive modelling and statistical analysis for the main metrics of the performance of wireless networks. Also, we gave new aspects of the design of high-dense traditional cellular networks as a natural extension of the work that we addressed on

drone assisted cellular networks. We also gave a brief analysis of drone-assisted backscatter communication networks for IoT sensor networks applications. We can conclude the research that we addressed in the thesis in the following three main parts.

8.1.1 Drone Assisting Cellular Networks

This research topic of the thesis comprised of three chapters 3-5. We employed stochastic geometry tools to study the network optimal dimensioning in multiple deployment scenarios for drones assisting public safety cellular networks in post disaster scenarios. In chapter 3, we presented the fundamental optimal dimensioning for single drone small cells for cellular network capacity off-loading. For a more comprehensive addition to the literature, we extended the spatial and statistical modelling parameters that should be undertaken in the topology deployment for drone wireless communication systems. In particular, transmitter antenna gain pattern and multi-path fading channel effects are considered. We showed that for certain cell setup parameters and coverage area, there is an optimal drone altitude that secures the best performance results. To this end, optimization is done by averaging for the studied performance metrics over all the downlink user locations inside the drone coverage area.

In chapter 4, we developed a more comprehensive framework for the design of drone empowered small cellular networks. We modelled the drone empowered small cellular networks by a finite binomial point process where multi-drone cells are used to overcome the network capacity shortfall. That is, we studied the co-existence of drone small cells in a bounded area on the top

of an operational ground cellular network in a post-disaster situation. We defined and studied the design parameters such as optimal altitude and number of drone base stations, etc., as a function of destroyed BSs, propagation conditions, etc. We also presented a comprehensive statistical framework which is developed from stochastic geometry perspectives. We then employed the developed framework to investigate the impact of several parametric variations on the performance of the DSCNs. Without loss of any generality, the performance metric employed is coverage probability of a down-link mobile user. It is demonstrated that by intelligently selecting the number of drones and their corresponding altitudes, ground users coverage can be significantly enhanced. This is obtained without incurring significant performance penalty to the mobile users which continue to be served from operating ground infrastructure.

In chapter 5, we developed a more comprehensive statistical framework to characterize and model the large-scale drone enabled cellular networks for post-disaster recovery networks. We studied a wider and more realistic scenario considering the capacity and back-hauling limitations on drone small cells (DSCs). That is, we studied the scenario where each coverage hole requires a multitude of DSCs to meet the shortfall coverage at the desired quality-of-service (QoS). Also, we extended the model to consider a new model where ground users also tend to cluster in hot-spots in a post-disaster scenario. Hence, we considered clustered deployment of DSCs around the site of the destroyed BS (i.e., user centric deployment). We demonstrated that the joint consideration of partially operating BSs and deployed DSCs yields a unique topology for such public safety networks. Hence, we proposed a clustering mechanism that extended the traditional Matern and Thomas cluster processes to a more general case where cluster size is dependent upon the size of the coverage hole. We then employed the newly developed framework to find

closed-form expressions that is verified by Monte-Carlo simulations to quantify the coverage probability, area spectral efficiency (ASE) and the energy efficiency (EE) for the down-link mobile user. We also explored several design parameters (for both of the adopted cluster processes) that address optimal deployment of the network (i.e., number of drones per cluster, drone altitudes and transmit power ratio between the traditional surviving BSs and the drone BSs). Finally, it is also shown that by optimizing these parameters the coverage probability and the energy efficiency of a ground user can be significantly enhanced in a post-disaster situation.

8.1.2 Optimal Coverage and Rate in Downlink Cellular Networks

In chapter 6, we revisited the design aspects for the traditional cellular networks. Mainly, we presented a detailed analysis of the coverage and spectral efficiency of a downlink cellular network. Hence, rather than relying on the first order statistics of the received signal-to-interference-ratio (SIR) such as coverage probability, we focused on characterizing its meta-distribution. The analysis has incorporated the practical ABG path-loss model which provides us with the flexibility to analyse urban macro (UMa) and urban micro (UMi) deployments. We quantified the meta-distribution to characterize the users' fairness experience using the exact solution of Gil-Pelaez and also Mnatsakanov's theorems for an accurate approximation. Using the evaluated analytical framework, we demonstrated that the selection of underlying degrees-of-freedom such as BS height for optimization of first order statistics such as coverage probability is not optimal in the network-wide sense. Consequently, the SIR meta-distribution must be employed to select appropriate operational points

which will ensure consistent user experiences across the network. Our design framework revealed that the traditional results which advocate lowering of BS heights (or even optimal selection of BS height) do not yield consistent service experience across users. By employing the developed framework we also demonstrate how available spectral resources in terms of time slots/channel partitions can be optimized by considering the meta-distribution of the SIR.

8.1.3 Drone-Assisted Backscatter Communication for IoT Sensor Network

In chapter 7, we developed a comprehensive framework to characterize the performance of a drone-assisted backscatter communication-based Internet of Things (IoT) sensor network. We considered a scenario where the drone transmits an RF carrier that is modulated by IoT sensor node (SN) to transmit its data. The SN implements load modulation which results in amplitude shift keying (ASK) type modulation for the impinging RF carrier. In order to quantify the performance of the considered network, we characterized the coverage probability for the ground based SN node by utilizing the same tools from stochastic geometry. The statistical framework that we developed to quantify the coverage probability explicitly accommodates a dyadic backscatter channel which experiences deeper fades than that of the one-way Rayleigh channel. Our model also incorporated Line of Sight (LoS) and Non-LoS (NLoS) propagation states for accurately modelling large-scale path-loss between drone and SN. We considered spatially distributed SNs which can be modelled using a spatial binomial point process. We practically implement the proposed system using Software Defined Radio (SDR) and a custom designed SN tag. The mea-

surements of parameters such as noise figure, tag reflection coefficient etc., are used to parametrize the developed framework. We demonstrated that there exists a fruitful interplay between the SN's reflection coefficient, drone height and the number of SNs which jointly dictate an optimal operation point at which coverage probability is maximized.

8.2 Future Work

In the previous chapters, we introduced some performance evaluation for drone-assisted wireless networks. As a result, we identified many open issues as future directions.

Cellular Network Thinning Model

In chapters 4 and 5, for the sake of simplifying the analysis, we assumed that the thinning process of the cellular network is applied in the two dimensional space of the operational base stations. Therefore, the DBSs are distributed in the same space of the thinned process that models the original cellular network. However, in post-disaster scenarios, the infrastructure destruction will be in bounded geographical regions and the number of drones needed for the recovery will be countable. Hence, in order for an effective distribution of the drones, an estimation of the location of the users and the number of hot-spots required is necessary. This will lead to an estimation problem of the optimal number of drones to be used and the location of clusters (i.e., hot-spots) where the drones need to be distributed. We also assumed independent thinning of BSs. Actually, this assumption is sufficient for the sake of simplifying the analysis. However, this might be non-realistic for urban areas of the city. In

some post disaster scenarios (e.g., earthquakes or human made destruction), the thinning process might be dependent on the geographical location of the BS. Hence, a comprehensive mathematical modelling of the thinning process can be more accurate and give a better performance insight.

Channel Partitioning and Higher-Order Statistics

In chapter 6, we considered the resource allocation problem in traditional single tier cellular networks in terms of bandwidth partitioning or time-slot sharing and showed how such a problem can be tackled using the meta-distribution. For a future extension, we will study the same performance metrics for a multi-tier, user-centric heterogeneous network. Also, the same problem applies for the design of drone assisted wireless networks and this will add more degrees of freedom to the network design space. Moreover, for better understanding of drone wireless network characteristics, we also need to study the meta distribution of the SIR for drone-assisted cellular networks.

Trajectory Optimization for IoT networks

Throughout the thesis, we assumed that the drones are in fixed positions and hovering on the top of the served users or sensor tags. In the backscatter and IoT applications, where a large number of ultra-low power nodes are distributed, the drone needs to be in proximity with the nodes, and this requires the drone to move in the coverage space. However, with no prior knowledge of the location of the node (i.e., a random spatial distribution of the nodes and blind tag nodes), visiting the location of all the nodes is not applicable due to the drone energy constraints. Hence, we need an optimized drone path plan to maximize the coverage in an energy aware fashion. This requires a more comprehensive framework to incorporate the randomness and the trajectory

of the drones while moving on the coverage space. As we described in chapter 7, the location of the flying drone reader is a random variable. However, this random variable should be replaced with the actual path that the drone takes in the data gathering/collection phase. The path shape, drone speed and the sensor node harvested power coupled with the wake-up time for the backscatter nodes are all extra parameters that affect the overall performance of the wireless backscatter system. Hence, a rigorous analytical framework which incorporates all the previously mentioned parameters is a straight extension to the work that we showed in the thesis.

Drone-to-SN Backscatter Dyadic Fading Channel

In chapter 7, we assumed that the large-scale fading model is the same for the forward and the backward channels (i.e., uplink and downlink channels). This assumption is valid for short distance communication where the LoS link in more likely guaranteed. Also, in some scenarios, the location of the carrier transmit antenna and the reader's receive antenna are not the same, and hence the path-loss will not be the same for the dyadic link. Therefore, incorporating the randomness of the spatial distribution for the scenario where the reader's receive antenna and the carrier illuminator locations are not the same is a natural extension to work. This produces into two different point processes, and the correlation between them will add more mathematical challenges to build the statistical framework. Also, for higher and efficient power harvesting on the sensor tag, the carrier is designed using directional antennas with antenna down-tilting. As we described in chapter 6, the antenna gain pattern is an optimization parameter and directly affects network design. We aim to address this issue as a future extension coupled with the integration of massive MIMO antennas design of the communication system components. Lastly, in

the space of co-channel and large-number of SNs, interference in the uplink channel is predicted and medium access schemes need to be taken into account bearing in mind the ultra low power design philosophy of the backscatter nodes where the node has no prior knowledge about the reader and cannot sense the channel.

Appendix A

Appendix of Chapter 5

In this appendix, the mathematical derivations and proofs of chapter 5 are presented.

A.1 Proof of Lemma 5.1

The Laplace transform of the interference from in-cluster DBSs at a typical DMU can be evaluated for a MCP as

$$\begin{aligned}\mathcal{L}_{I_{\Phi^M_{C_{in}}}}(s|r_1,\sigma_M) &\overset{(a)}{=} \mathbb{E}\Big[\exp\Big(-s\sum_{\mathbf{y}\in\Phi^M_{C_{in}}} P_D\,|g|^2\,\frac{\left(h^2+\|\mathbf{x_0}+\mathbf{y}\|^2\right)^{-1}}{\bar{\kappa}\left(\|\mathbf{x_0}+\mathbf{y}\|\right)}\Big)\Big]\\ &\overset{(b)}{=} \mathbb{E}\Big[\prod_{\mathbf{y}\in\Phi^M_{C_{in}}}\frac{1}{1+sP_D\frac{1}{\bar{\kappa}\left(\|\mathbf{x_0}+\mathbf{y}\|\right)\left(h^2+\|\mathbf{x_0}+\mathbf{y}\|^2\right)}}\Big]\\ &\overset{(c)}{=} \sum_{i=1}^{N_d}\left(\int_{r_1}^{\infty}\frac{1}{1+\frac{sP_D}{\bar{\kappa}(\|\mathbf{x_0}+\mathbf{y}\|)(h^2+\|\mathbf{x_0}+\mathbf{y}\|^2)}}f^M(\mathbf{y})\,\mathrm{d}\mathbf{y}\right)^{i-1}\\ &\quad\times\underbrace{\frac{\bar{N}_d^i\exp(-\bar{N}_d)}{i!\Sigma_{k=1}^{N_d}\frac{\bar{N}_d^k\exp(-\bar{N}_d)}{k!}}}_{\xi(i,N_d)}\end{aligned}$$

$$\overset{(d)}{=} \sum_{i=1}^{N_d} \left(\int_{r_1}^{\infty} \frac{1}{1+\frac{sP_D}{\bar{\kappa}(r_x)(h^2+r_x^2)}} f_{R_x}^{M}(r_x|v_o,\sigma_M)\,\mathrm{d}r_x \right)^{i-1} \times \xi(i,N_d). \tag{A.1}$$

where (a) is obtained by applying the definition of the Laplace transform, (b) is obtained by taking the expectation over the Rayleigh fading channel coefficient $|g|^2$, (c) is obtained by applying the PGFL and conditioning that the number of co-channel operating drones $K = k$ is Poisson distributed. We include the fact that the total number of co-working drones is less than N_d and, (d) is obtained by a simple change of variables $\|\mathbf{x_0}+\mathbf{y}\| \to r_o$ and then by transformation from Cartesian to polar coordinates.

A.2 Proof of Lemma 5.2

The Laplace transform of the interference from out-of-cluster DBSs at a typical DMU can be evaluated for a MCP as

$$\begin{aligned}
\mathcal{L}_{I_{C_{out}^{\Phi_M}}}(s|r_1,\sigma_M) &\overset{(a)}{=} \mathbb{E}\Big[\exp\Big(-s\sum_{\mathbf{x}\in\Phi_D\setminus\mathbf{x_0}}\sum_{\mathbf{y}\in\Phi_{C_\mathbf{x}}^M} P_D\,|g|^2\,\frac{\left(h^2+\|\mathbf{x}+\mathbf{y}\|^2\right)^{-1}}{\bar{\kappa}\left(\|\mathbf{x}+\mathbf{y}\|\right)}\Big)\Big] \\
&\overset{(b)}{=} \mathbb{E}_{\Phi_D}\Big[\prod_{\mathbf{x}\in\Phi_D\setminus\mathbf{x_0}} \mathbb{E}_{\Phi_{C_\mathbf{x}}^M}\Big[\prod_{\mathbf{y}\in\Phi_{C_\mathbf{x}}^M}\frac{1}{1+sP_D\frac{\left(h^2+\|\mathbf{x}+\mathbf{y}\|^2\right)^{-1}}{\bar{\kappa}\left(\|\mathbf{x}+\mathbf{y}\|\right)}}\Big]\Big] \\
&\overset{(c)}{=} \mathbb{E}_{\Phi_D}\Big[\prod_{\mathbf{x}\in\Phi_D\setminus\mathbf{x_0}} \exp\Big(-\frac{N_d}{N_c} \\
&\quad\times\int_0^{\infty}\Big(1-\frac{1}{1+sP_D\frac{1}{\bar{\kappa}(r_o)(h^2+r_o^2)}}\Big) f_{R_o}^{M}(r_o|v,\sigma_M)\,\mathrm{d}r_o\Big)\Big] \\
&\overset{(d)}{=} \exp\Big(-2\pi\lambda_D\int_0^{\infty}\Big(1-\exp\Big(-\frac{N_d}{N_c}\int_0^{\infty} \\
&\quad\times\Big(1-\frac{1}{1+sP_D\frac{1}{\bar{\kappa}(r_o)(h^2+r_o^2)}}\Big) f_{R_o}^{M}(r_o|u,\sigma_M)\,\mathrm{d}r_o\Big)\Big)u\,\mathrm{d}u\Big)
\end{aligned} \tag{A.2}$$

where (a) is obtained by applying the definition of the Laplace transform, (b) is obtained by taking the expectation over the Rayleigh fading channel coefficient $|g|^2$ assuming i.i.d. fading channels, (c) is obtained by applying the PGFL with change of variables $\|\mathbf{x}+\mathbf{y}\| \to r_o$ and then by transformation from Cartesian to polar coordinates, and (d) is obtained by applying the PGFL of the PPP.

A.3 Proof of Lemma 5.3

The Laplace transform of the interference from in-cluster DBSs at a typical DMU can be evaluated for TCP as

$$\begin{aligned}
\mathcal{L}_{I_{\Phi^T_{C_{in}}}}(s|r_1,\sigma_T) &\overset{(a)}{=} \mathbb{E}\Big[\exp\Big(-s\sum_{\mathbf{y}\in\Phi^T_{C_{in}}} P_D\,|g|^2\,\frac{\left(h^2+\|\mathbf{x_0}+\mathbf{y}\|^2\right)^{-1}}{\bar{\kappa}\left(\|\mathbf{x_0}+\mathbf{y}\|\right)}\Big)\Big] \\
&\overset{(b)}{=} \mathbb{E}\Big[\prod_{\mathbf{y}\in\Phi^T_{C_{in}}} \frac{1}{1+sP_D\frac{1}{\bar{\kappa}\left(\|\mathbf{x_0}+\mathbf{y}\|\right)\left(h^2+\|\mathbf{x_0}+\mathbf{y}\|^2\right)}}\Big] \\
&\overset{(c)}{=} \sum_{i=1}^{N_d}\left(\int_{r_1}^{\infty}\frac{1}{1+\frac{sP_D}{\bar{\kappa}(\|\mathbf{x_0}+\mathbf{y}\|)(h^2+\|\mathbf{x_0}+\mathbf{y}\|^2)}}f^T(\mathbf{y})\,\mathrm{d}\mathbf{y}\right)^{i-1} \\
&\quad\times\underbrace{\frac{\bar{N}_d^i\exp(-\bar{N}_d)}{i!\Sigma_{k=1}^{N_d}\frac{\bar{N}_d^k\exp(-\bar{N}_d)}{k!}}}_{\xi(i,N_d)} \\
&\overset{(d)}{=} \sum_{i=1}^{N_d}\left(\int_{r_1}^{\infty}\frac{1}{1+\frac{sP_D}{\bar{\kappa}(r_x)(h^2+r_x^2)}}f^T_{R_x}(r_x|v_o,\sigma_T)\,\mathrm{d}r_x\right)^{i-1} \\
&\quad\times\xi(i,N_d)
\end{aligned} \tag{A.3}$$

where (a) is obtained by applying the definition of the Laplace transform, (b) is obtained by taking the expectation over the Rayleigh fading channel coefficient $|g|^2$ and, (c) is obtained by applying the PGFL and conditioning that the number of co-channel operating drones $K=k$ is Poisson distributed

and, (d) is obtained by a simple change of variables $\|\mathbf{x_0}+\mathbf{y}\| \to r_o$ and then by transformation from Cartesian to polar.

A.4 Proof of Lemma 5.4

The Laplace transform of the interference from out-of-cluster DBSs at a typical DMU can be evaluated for TCP as

$$\begin{aligned}
\mathcal{L}_{I_{\Phi^T_{C_{out}}}}(s|r_1,\sigma_T) &\overset{(a)}{=} \mathbb{E}\Big[\exp\Big(-s\sum_{\mathbf{x}\in\Phi_D\setminus\mathbf{x_0}}\sum_{\mathbf{y}\in\Phi^T_{C_\mathbf{x}}} P_D\,|g|^2\,\frac{\left(h^2+\|\mathbf{x}+\mathbf{y}\|^2\right)^{-1}}{\bar{\kappa}\left(\|\mathbf{x}+\mathbf{y}\|\right)}\Big)\Big] \\
&\overset{(b)}{=} \mathbb{E}_{\Phi_D}\Big[\prod_{\mathbf{x}\in\Phi_D\setminus\mathbf{x_0}} \mathbb{E}_{\Phi^T_{C_\mathbf{x}}}\Big[\prod_{\mathbf{y}\in\Phi^T_{C_\mathbf{x}}}\frac{1}{1+sP_D\frac{\left(h^2+\|\mathbf{x}+\mathbf{y}\|^2\right)^{-1}}{\bar{\kappa}\left(\|\mathbf{x}+\mathbf{y}\|\right)}}\Big]\Big] \\
&\overset{(c)}{=} \mathbb{E}_{\Phi_D}\Big[\prod_{\mathbf{x}\in\Phi_D\setminus\mathbf{x_0}} \exp\Big(-\frac{N_d}{N_c} \\
&\quad\times\int_0^\infty\Big(1-\frac{1}{1+sP_D\frac{1}{\bar{\kappa}(r_o)(h^2+r_o^2)}}\Big)f^T_{R_o}(r_o|v,\sigma_T)\,\mathrm{d}r_o\Big)\Big] \\
&\overset{(d)}{=} \exp\Big(-2\pi\lambda_D\int_0^\infty\Big(1-\exp\Big(-\frac{N_d}{N_c}\int_0^\infty \\
&\quad\times\Big(1-\frac{1}{1+sP_D\frac{1}{\bar{\kappa}(r_o)(h^2+r_o^2)}}\Big)f^T_R(r_o|u,\sigma_T)\,\mathrm{d}r_o\Big)\Big)u\,\mathrm{d}u\Big) \qquad \text{(A.4)}
\end{aligned}$$

where (a) is obtained by applying the definition of the Laplace transform, (b) is obtained by taking the expectation over the Rayleigh fading channel coefficient G assuming i.i.d. fading channels, (c) is obtained by applying the PGFL with change of variables $\|\mathbf{x}+\mathbf{y}\| \to r_o$ and then by transformation from Cartesian to polar coordinates and, (d) is obtained by applying the PGFL of the PPP.

Appendix B

Appendix of Chapter 6

In this appendix, the mathematical derivations and proofs of chapter 6 are presented.

B.1 Proof of Theorem 6.1

The coverage probability is given by

$$\begin{aligned} P_\theta &= \Pr\left[\mathrm{SIR} \geq \theta\right], \\ &= \mathbb{E}_{r_1}\Big[\mathcal{P}_L(h, r_1) \underbrace{\Pr\left[\frac{|g|^2 \; L_L^{-1}(r_1)}{I_\Phi} \geq \theta\right]}_{A(r_1,\theta)} + \mathcal{P}_{NL}(h, r_1) \underbrace{\Pr\left[\frac{|g|^2 \; L_{NL}^{-1}(r_1)}{I_\Phi} \geq \theta\right]}_{B(r_1,\theta)}\Big] \end{aligned} \tag{B.1}$$

where

$$\begin{aligned} A(r_1,\theta) \quad &= \mathbb{E}_{I_{\Phi_L}, I_{\Phi_{NL}}}[\exp(-sI_\Phi)], \\ &= \mathbb{E}_{|g|^2, I_{\Phi_L}, I_{\Phi_{NL}}}[\prod_{\substack{m\in\Phi_{NL} \\ i\in\Phi_L}} \exp\left(-s\left|g\right|^2 (L_L^{-1}(h, r_i) + L_{NL}^{-1}(h, r_m))\right)], \end{aligned}$$

$$\overset{(a)}{=} \mathbb{E}_{I_{\Phi_L},I_{\Phi_{NL}}}[\prod_{\substack{m\in\Phi_{NL}\\ i\in\Phi_L}} \underbrace{\frac{\mathcal{P}_L(r_i)}{1+sL_L^{-1}(h,r)}+\frac{\mathcal{P}_{NL}(r_m)}{1+sL_{NL}^{-1}(h,r_m)}}_{\eta(s,r)}],$$

$$\overset{(b)}{=} \exp\Big(-2\pi\frac{\lambda N_a}{N_s}\int_{r_1}^{\infty} 1-\eta(s,r)\,\mathrm{d}r\Big), \tag{B.2}$$

with (a) is obtained by taking the expectation over the Rayleigh fading channel coefficient $|g|^2$, (b) is obtained by applying the probability generating functional (PGFL) of the PPP, $s=\theta/L_L^{-1}(h,r_1)$ and $B((r_1,\theta)$ can be obtained in the same way as $A(r_1,\theta)$ by substituting s in $A((r_1,\theta)$ by $s=\theta/L_{NL}^{-1}(h,r_1)$. For the rate coverage P_{R_o}, with R_o we only substitute any θ by $2^{\frac{R_oN_s}{W}}-1$.

B.2 Proof of Theorem 6.3

The m^{th} moment $M_m(\theta)$ and $M_m(R_o)$ can be evaluated as

$$\begin{aligned} M_m(.) &= \mathbb{E}[P_i^m],\ \ i\in\{\theta,R_o\}\\ &= \mathbb{E}_{r_1}\left[\mathcal{P}_L(h,r_1)A_m(r_1,\theta)+\mathcal{P}_{NL}(h,r_1)B_m(r_1,\theta)\right], \end{aligned}$$

where

$$\begin{aligned} A_m(r_1,\theta) &= \mathbb{E}_{I_{\Phi_L},I_{\Phi_{NL}}}[\exp(-sI_\Phi)^m],\\ &\overset{(a)}{=} \mathbb{E}_{I_{\Phi_L},I_{\Phi_{NL}}}[\prod_{\substack{k\in\Phi_{NL}\\ i\in\Phi_L}} \underbrace{\frac{\mathcal{P}_L(r_i)}{(1+sL_L^{-1}(h,r))^m}+\frac{\mathcal{P}_{NL}(r_k)}{(1+sL_{NL}^{-1}(h,r_m))^m}}_{\eta_m(s,r)}],\\ &\overset{(b)}{=} \exp\Big(-2\pi\frac{\lambda N_a}{N_s}\int_{r_1}^{\infty} 1-\eta_m(s,r)\,\mathrm{d}r\Big), \end{aligned} \tag{B.3}$$

with (a) is obtained by taking the expectation over the Rayleigh fading channel coefficient $|g|^2$, (b) is obtained by applying the PGFL, $s=\theta/L_L^{-1}(h,r_1)$ and

$B_m(r_1, \theta)$ can be obtained in the same way as $A_m(r_1, \theta)$ by substituting s in $A_m(r_1, \theta)$ by $s = \theta / L_{NL}^{-1}(h, r_1)$ and θ by R_o. For the rate coverage P_{R_o} with R_o, we only substitute any θ by $2^{\frac{R_o N_s}{W}} - 1$.

Bibliography

[1] Ericsson, "The future of mobile subscriptions." https://www.ericsson.com/en/mobility-report/reports/november-2017/mobile-data-traffic-growth-outlook, [Online; accessed 2/02/2019]. (Cited on pages xii, 2, and 3.)

[2] Ericsson, "The future of mobile subscriptions." https://www.ericsson.com/en/mobility-report/future-of-mobile-subscriptions, [Online; accessed 2/02/2019]. (Cited on page 2.)

[3] S. C. Association, "Ee: Average uk smart home will have 50 connected devices by 2023." https://smartcitiesassociation.org/index.php/media-corner/news/169-ee-average-uk-smart-home-will-have-50-connected-devices-by-2023, [Online; accessed 2/02/2019]. (Cited on page 2.)

[4] M. Series, "Imt vision–framework and overall objectives of the future development of imt for 2020 and beyond," *Recommendation ITU*, pp. 2083–0, 2015. (Cited on page 3.)

[5] M. Mozaffari, W. Saad, M. Bennis, and M. Debbah, "Mobile internet of things: Can uavs provide an energy-efficient mobile architecture?," in *2016 IEEE Global Communications Conference (GLOBECOM)*, pp. 1–6, IEEE, 2016. (Cited on page 6.)

[6] A. Al-Hourani, S. Kandeepan, and S. Lardner, "Optimal lap altitude for maximum coverage," *Wireless Communications Letters, IEEE*, vol. 3, no. 6, pp. 569–572, 2014. (Cited on pages 6, 14, 15, 20, 45, 57, 71, 125, 131, and 136.)

[7] W. Khawaja, I. Guvenc, D. W. Matolak, U. Fiebig, and N. Schneckenberger, "A survey of air-to-ground propagation channel modeling for unmanned aerial vehicles," *IEEE Communications Surveys Tutorials*, pp. 1–1, 2019. (Cited on pages 6, 13, 20, and 45.)

[8] X. Lin, J. Andrews, A. Ghosh, and R. Ratasuk, "An overview of 3gpp device-to-device proximity services," *Communications Magazine, IEEE*, vol. 52, no. 4, pp. 40–48, 2014. (Cited on page 6.)

[9] G. Baldini, S. Karanasios, D. Allen, and F. Vergari, "Survey of wireless communication technologies for public safety," *Communications Surveys & Tutorials, IEEE*, vol. 16, no. 2, pp. 619–641, 2014. (Cited on page 6.)

[10] R. Ferrus, O. Sallent, G. Baldini, and L. Goratti, "Lte: the technology driver for future public safety communications," *Communications Magazine, IEEE*, vol. 51, no. 10, pp. 154–161, 2013. (Cited on page 6.)

[11] M. Mozaffari, W. Saad, M. Bennis, and M. Debbah, "Unmanned aerial vehicle with underlaid device-to-device communications: Performance and tradeoffs," *arXiv preprint arXiv:1509.01187*, 2015. (Cited on pages 6 and 8.)

[12] M. Mozaffari, W. Saad, M. Bennis, and M. Debbah, "Drone small cells in the clouds: Design, deployment and performance analysis," *arXiv preprint arXiv:1509.01655*, 2015. (Cited on pages 6, 15, 20, 51, 70, 75, 94, 96, 103, and 162.)

[13] S. Rohde, M. Putzke, and C. Wietfeld, "Ad hoc self-healing of ofdma networks using uav-based relays," *Ad Hoc Networks*, vol. 11, no. 7, pp. 1893–1906, 2013. (Cited on pages 6, 7, 11, 18, and 20.)

[14] S. Chandrasekharan, K. Gomez, A. Al-Hourani, S. Kandeepan, T. Rasheed, L. Goratti, L. Reynaud, D. Grace, I. Bucaille, T. Wirth, *et al.*, "Designing and implementing future aerial communication networks," *arXiv preprint arXiv:1602.05318*, 2016. (Cited on pages 6, 7, 11, and 17.)

[15] X. Li, D. Guo, H. Yin, and G. Wei, "Drone-assisted public safety wireless broadband network," in *Wireless Communications and Networking Conference Workshops (WCNCW), 2015 IEEE*, pp. 323–328, IEEE, 2015. (Cited on pages 6, 7, 8, 18, and 20.)

[16] M. Alzenad, M. Z. Shakir, H. Yanikomeroglu, and M.-S. Alouini, "Fso-based vertical backhaul/fronthaul framework for 5g+ wireless networks," *IEEE Communications Magazine*, vol. 56, no. 1, pp. 218–224, 2018. (Cited on pages 6, 7, 18, 19, and 20.)

[17] I. Bor-Yaliniz and H. Yanikomeroglu, "The new frontier in ran heterogeneity: Multi-tier drone-cells," *arXiv preprint arXiv:1604.00381*, 2016. (Cited on pages 6, 7, 12, 19, and 20.)

[18] K. Gomez, A. Hourani, L. Goratti, R. Riggio, S. Kandeepan, and I. Bucaille, "Capacity evaluation of aerial lte base-stations for public safety communications," in *Networks and Communications (EuCNC), 2015 European Conference on*, pp. 133–138, IEEE, 2015. (Cited on pages 7, 18, and 20.)

[19] R. Yaliniz, A. El-Keyi, and H. Yanikomeroglu, "Efficient 3-d placement of an aerial base station in next generation cellular networks," *arXiv preprint arXiv:1603.00300*, 2016. (Cited on pages 7, 14, 20, and 71.)

[20] Y. Zeng, R. Zhang, and T. J. Lim, "Wireless communications with unmanned aerial vehicles: Opportunities and challenges," *arXiv preprint arXiv:1602.03602*, 2016. (Cited on page 7.)

[21] P. Zhan, K. Yu, and A. L. Swindlehurst, "Wireless relay communications with unmanned aerial vehicles: Performance and optimization," *Aerospace and Electronic Systems, IEEE Transactions on*, vol. 47, no. 3, pp. 2068–2085, 2011. (Cited on page 7.)

[22] A. Merwaday and I. Guvenc, "Uav assisted heterogeneous networks for public safety communications," in *Wireless Communications and Networking Conference Workshops (WCNCW), 2015 IEEE*, pp. 329–334, IEEE, 2015. (Cited on pages 9, 11, 14, 20, and 94.)

[23] A. K. Saha, J. Saha, R. Ray, S. Sircar, S. Dutta, S. P. Chattopadhyay, and H. N. Saha, "Iot-based drone for improvement of crop quality in agricultural field," in *2018 IEEE 8th Annual Computing and Communication Workshop and Conference (CCWC)*, pp. 612–615, IEEE, 2018. (Cited on page 9.)

[24] I. Lee and K. Lee, "The internet of things (iot): Applications, investments, and challenges for enterprises," *Business Horizons*, vol. 58, no. 4, pp. 431–440, 2015. (Cited on page 9.)

[25] G. Ding, Q. Wu, L. Zhang, Y. Lin, T. A. Tsiftsis, and Y.-D. Yao, "An amateur drone surveillance system based on the cognitive internet of things," *IEEE Communications Magazine*, vol. 56, no. 1, pp. 29–35, 2018. (Cited on page 9.)

[26] N. H. Motlagh, M. Bagaa, and T. Taleb, "Uav-based iot platform: A crowd surveillance use case," *IEEE Communications Magazine*, vol. 55, no. 2, pp. 128–134, 2017. (Cited on page 10.)

[27] M. Mozaffari, W. Saad, M. Bennis, and M. Debbah, "Mobile internet of things: Can uavs provide an energy-efficient mobile architecture?," *arXiv preprint arXiv:1607.02766*, 2016. (Cited on pages 10 and 95.)

[28] J. Sae, S. F. Yunas, and J. Lempiainen, "Coverage aspects of temporary lap network," in *2016 12th Annual Conference on Wireless On-demand Network Systems and Services (WONS)*, pp. 1–4, IEEE, 2016. (Cited on page 11.)

[29] R. Amorim, H. Nguyen, P. Mogensen, I. Z. Kovács, J. Wigard, and T. B. Sørensen, "Radio channel modeling for uav communication over cellular networks," *IEEE Wireless Communications Letters*, vol. 6, no. 4, pp. 514–517, 2017. (Cited on page 11.)

[30] Q. Feng, J. McGeehan, E. K. Tameh, and A. R. Nix, "Path loss models for air-to-ground radio channels in urban environments," in *Vehicular Technology Conference, 2006. VTC 2006-Spring. IEEE 63rd*, vol. 6, pp. 2901–2905, IEEE, 2006. (Cited on pages 12, 13, and 20.)

[31] Q. Feng, E. K. Tameh, A. R. Nix, and J. McGeehan, "Wlcp2-06: Modelling the likelihood of line-of-sight for air-to-ground radio propagation in urban environments," in *Global Telecommunications Conference, 2006. GLOBECOM'06. IEEE*, pp. 1–5, IEEE, 2006. (Cited on pages 12, 13, and 20.)

[32] J. Holis and P. Pechac, "Elevation dependent shadowing model for mobile communications via high altitude platforms in built-up areas," *Antennas and Propagation, IEEE Transactions on*, vol. 56, no. 4, pp. 1078–1084, 2008. (Cited on pages 13, 20, and 52.)

[33] A. Al-Hourani, S. Kandeepan, and A. Jamalipour, "Modeling air-to-ground path loss for low altitude platforms in urban environments," in *Global Communications Conference (GLOBECOM), 2014 IEEE*, pp. 2898–2904, IEEE, 2014. (Cited on pages 13, 20, 46, 47, and 52.)

[34] A. Al-Hourani and K. Gomez, "Modeling cellular-to-uav path-loss for suburban environments," *IEEE Wireless Communications Letters*, vol. 7, no. 1, pp. 82–85, 2018. (Cited on pages 13 and 47.)

[35] X. Zhou, J. Guo, S. Durrani, and H. Yanikomeroglu, "Uplink coverage performance of an underlay drone cell for temporary events," in *2018 IEEE International Conference on Communications Workshops (ICC Workshops)*, pp. 1–6, IEEE, 2018. (Cited on page 13.)

[36] M. M. Azari, F. Rosas, A. Chiumento, A. Ligata, and S. Pollin, "Uplink performance analysis of a drone cell in a random field of ground interferers," in *2018 IEEE Wireless Communications and Networking Conference (WCNC)*, pp. 1–6, IEEE, 2018. (Cited on page 13.)

[37] W. Guo, C. Devine, and S. Wang, "Performance analysis of micro unmanned airborne communication relays for cellular networks," in *Communication Systems, Networks & Digital Signal Processing (CSNDSP), 2014 9th International Symposium on*, pp. 658–663, IEEE, 2014. (Cited on pages 14 and 20.)

[38] M. Mozaffari, W. Saad, M. Bennis, and M. Debbah, "Optimal transport theory for power-efficient deployment of unmanned aerial vehicles," *arXiv preprint arXiv:1602.01532*, 2016. (Cited on pages 14, 15, and 20.)

[39] Y. Zeng and R. Zhang, "Energy-efficient uav communication with trajectory optimization," *IEEE Transactions on Wireless Communications*, vol. 16, no. 6, pp. 3747–3760, 2017. (Cited on pages 16 and 20.)

[40] Q. Wu, Y. Zeng, and R. Zhang, "Joint trajectory and communication design for multi-uav enabled wireless networks," *IEEE Transactions on Wireless Communications*, vol. 17, no. 3, pp. 2109–2121, 2018. (Cited on pages 16 and 20.)

[41] M. Mozaffari, W. Saad, M. Bennis, and M. Debbah, "Wireless communication using unmanned aerial vehicles (uavs): Optimal transport theory for hover time optimization," *IEEE Transactions on Wireless Communications*, vol. 16, no. 12, pp. 8052–8066, 2017. (Cited on pages 16, 17, and 20.)

[42] E. Yanmaz, S. Yahyanejad, B. Rinner, H. Hellwagner, and C. Bettstetter, "Drone networks: Communications, coordination, and sensing," *Ad Hoc Networks*, vol. 68, pp. 1–15, 2018. (Cited on pages 17 and 20.)

[43] E. Yanmaz, M. Quaritsch, S. Yahyanejad, B. Rinner, H. Hellwagner, and C. Bettstetter, "Communication and coordination for drone networks," in *Ad Hoc Networks*, pp. 79–91, Springer, 2017. (Cited on pages 17 and 20.)

[44] M. Garraffa, M. Bekhti, L. Létocart, N. Achir, and K. Boussetta, "Drones path planning for wsn data gathering: a column generation heuristic approach," in *2018 IEEE Wireless Communications and Networking Conference (WCNC)*, pp. 1–6, IEEE, 2018. (Cited on pages 17 and 20.)

[45] C. Cambra, S. Sendra, J. Lloret, and L. Parra, "Ad hoc network for emergency rescue system based on unmanned aerial vehicles," *Network Protocols and Algorithms*, vol. 7, no. 4, pp. 72–89, 2016. (Cited on pages 18 and 20.)

[46] Z. Xiao, P. Xia, and X.-G. Xia, "Enabling uav cellular with millimeter-wave communication: Potentials and approaches," *IEEE Communications Magazine*, vol. 54, no. 5, pp. 66–73, 2016. (Cited on pages 18, 19, and 20.)

[47] A. Malik and P. Singh, "Free space optics: current applications and future challenges," *International Journal of Optics*, vol. 2015, 2015. (Cited on pages 19 and 20.)

[48] S. Sekander, H. Tabassum, and E. Hossain, "Multi-tier drone architecture for 5g/b5g cellular networks: Challenges, trends, and prospects," *IEEE Communications Magazine*, vol. 56, no. 3, pp. 96–103, 2018. (Cited on pages 19 and 20.)

[49] E. Kalantari, M. Z. Shakir, H. Yanikomeroglu, and A. Yongacoglu, "Backhaul-aware robust 3d drone placement in 5g+ wireless networks," *arXiv preprint arXiv:1702.08395*, 2017. (Cited on page 20.)

[50] A. Omri, M. O. Hasna, M. Z. Shakir, and M. Shaqfeh, "3-d placement schemes of multiple uavs in nfp-based wireless networks," in *2018 5th International Conference on Information and Communication Technologies for Disaster Management (ICT-DM)*, pp. 1–5, IEEE, 2018. (Cited on page 20.)

[51] A. M. Hayajneh, S. A. R. Zaidi, D. C. McLernon, and M. Ghogho, "Optimal dimensioning and performance analysis of drone-based wireless communications," in *2016 IEEE Globecom Workshops (GC Wkshps)*, pp. 1–6, Dec 2016. (Cited on page 26.)

[52] A. M. Hayajneh, S. A. R. Zaidi, D. McLernon, and M. Ghogho, "Drone empowered small cellular disaster recovery networks for resilient smart cities," in *2016 First International Workshop on Toward A City-Wide Pervasive EnviRonment (SECON Workshops) (CoWPER'16)*, (London, United Kingdom), June 2016. (Cited on pages 26, 98, and 158.)

[53] A. M. Hayajneh, S. A. R. Zaidi, D. C. McLernon, and M. Ghogho, "Performance analysis of uav enabled disaster recovery network: A stochastic geometric framework based on matern cluster processes," in *Third Intelligent Signal Processing Conference Proceedings (ISP 2017)*, Institution of Engineering and Technology, 2017. (Cited on pages 27, 98, and 125.)

[54] A. M. Hayajneh, S. A. R. Zaidi, D. C. McLernon, M. Di Renzo, and M. Ghogho, "Performance analysis of uav enabled disaster recovery networks: A stochastic geometric framework based on cluster processes," *IEEE Access*, vol. 6, pp. 26215–26230, 2018. (Cited on pages 27 and 158.)

[55] A. M. Hayajneh, S. A. R. Zaidi, D. C. Mclernon, M. Z. Win, A. Imran, and M. Ghogho, "Optimal coverage and rate in downlink cellular networks: A sir meta-distribution based approach," in *2018 IEEE Global Communications Conference (GLOBECOM)*, pp. 1–7, Dec 2018. (Cited on page 28.)

[56] A. M. Hayajneh, S. A. R. Zaidi, M. Hafeez, D. C. Mclernon, and M. Z. Win, "Coverage analysis of drone-assisted backscatter communication for iot sensor network," in *1st International Workshop on Wireless sensors and Drones in Internet of Things (Wi-DroIT)*, pp. 1–7, May 2019. (Cited on page 29.)

[57] H. ElSawy, E. Hossain, and M. Haenggi, "Stochastic geometry for modeling, analysis, and design of multi-tier and cognitive cellular wireless networks: A survey," *Communications Surveys & Tutorials, IEEE*, vol. 15, no. 3, pp. 996–1019, 2013. (Cited on page 32.)

[58] H. ElSawy and E. Hossain, "Two-tier hetnets with cognitive femtocells: Downlink performance modeling and analysis in a multichannel envi-

ronment," *Mobile Computing, IEEE Transactions on*, vol. 13, no. 3, pp. 649–663, 2014. (Cited on page 32.)

[59] S. Srinivasa and M. Haenggi, "Modeling interference in finite uniformly random networks," in *International Workshop on Information Theory for Sensor Networks (WITS07)*, pp. 1–12, 2007. (Cited on pages 33, 34, 74, and 82.)

[60] M. Haenggi and R. K. Ganti, *Interference in large wireless networks*. Now Publishers Inc, 2009. (Cited on pages 33, 45, and 85.)

[61] S. N. Chiu, D. Stoyan, W. S. Kendall, and J. Mecke, *Stochastic geometry and its applications*. John Wiley & Sons, 2013. (Cited on pages 34, 36, 79, 99, 134, and 160.)

[62] M. Haenggi, *Stochastic geometry for wireless networks*. Cambridge University Press, 2012. (Cited on pages 39, 96, 100, 112, and 130.)

[63] S. Srinivasa and M. Haenggi, "Distance distributions in finite uniformly random networks: Theory and applications," *IEEE Transactions on Vehicular Technology*, vol. 59, no. 2, pp. 940–949, 2010. (Cited on pages 40, 78, 94, and 97.)

[64] D. Moltchanov, "Distance distributions in random networks," *Ad Hoc Networks*, vol. 10, no. 6, pp. 1146–1166, 2012. (Cited on page 40.)

[65] A. Jeffrey and D. Zwillinger, *Table of integrals, series, and products*. Academic Press, 2007. (Cited on pages 40 and 86.)

[66] S. A. R. Zaidi, D. C. McLernon, and M. Ghogho, "Breaking the area spectral efficiency wall in cognitive underlay networks," *Selected Areas in Communications, IEEE Journal on*, vol. 32, no. 11, pp. 2205–2221, 2014. (Cited on pages 45 and 85.)

[67] J. G. Andrews, "Seven ways that hetnets are a cellular paradigm shift," *Communications Magazine, IEEE*, vol. 51, no. 3, pp. 136–144, 2013. (Cited on page 45.)

[68] 3GPP, "Further advancements for e-utra physical layer aspects," tech. rep., 3GPP TR 36.814, 2010. (Cited on pages 45, 52, 56, 77, 104, and 131.)

[69] 3GPP, "Digital cellular telecommunications system (phase 2+); radio network planning aspects," tech. rep., 3GPP TR 43.030, 2010. (Cited on pages 45, 77, and 104.)

[70] A. A. Khuwaja, Y. Chen, N. Zhao, M.-S. Alouini, and P. Dobbins, "A survey of channel modeling for uav communications," *IEEE Communications Surveys & Tutorials*, vol. 20, no. 4, pp. 2804–2821, 2018. (Cited on page 45.)

[71] A. Ranjan, B. Panigrahi, H. K. Rath, P. Misra, A. Simha, and H. Sahu, "A study on pathloss model for uav based urban disaster and emergency communication systems," in *2018 Twenty Fourth National Conference on Communications (NCC)*, pp. 1–6, IEEE, 2018. (Cited on page 48.)

[72] I. Bucaille, S. Hethuin, T. Rasheed, A. Munari, R. Hermenier, and S. Allsopp, "Rapidly deployable network for tactical applications: Aerial base station with opportunistic links for unattended and temporary events absolute example," in *Military Communications Conference, MILCOM IEEE*, pp. 1116–1120, IEEE, 2013. (Cited on pages 51, 70, 94, and 96.)

[73] P. Zhan, K. Yu, *et al.*, "Wireless relay communications with unmanned aerial vehicles: Performance and optimization," *Aerospace and Electronic Systems, IEEE Transactions on*, vol. 47, no. 3, pp. 2068–2085, 2011. (Cited on pages 51 and 70.)

[74] W. Guo, C. Devine, and S. Wang, "Performance analysis of micro unmanned airborne communication relays for cellular networks," in *Communication Systems, Networks & Digital Signal Processing (CSNDSP), 2014 9th International Symposium on*, pp. 658–663, IEEE, 2014. (Cited on pages 51, 70, 94, and 96.)

[75] S. H. Alsamhi and N. Rajput, "An intelligent hap for broadband wireless communications: Developments, qos and applications," *International Journal of Electronics and Electrical Engineering*, vol. 3, no. 2, 2015. (Cited on pages 51 and 70.)

[76] Q. Feng, E. K. Tameh, A. R. Nix, and J. McGeehan, "Modelling the likelihood of line-of-sight for air-to-ground radio propagation in urban environments," in *Global Telecommunications Conference, 2006. GLOBECOM'06. IEEE*, pp. 1–5, IEEE, 2006. (Cited on page 52.)

[77] A. Thornburg, T. Bai, and R. W. Heath Jr, "Performance analysis of mmwave ad hoc networks," *arXiv preprint arXiv:1412.0765*, 2014. (Cited on pages 52 and 56.)

[78] M. Gharibi, R. Boutaba, and S. L. Waslander, "Internet of drones," *arXiv preprint arXiv:1601.01289*, 2016. (Cited on pages 52, 70, 94, and 96.)

[79] A. Goldsmith, *Wireless Communications*. Cambridge University Press, 1st edn ed., 2005. (Cited on page 55.)

[80] J. Proakis and M. Salehi, *Digital Communications*. McGraw-Hill International Edition, McGraw-Hill Higher Education, 5th ed., 2008. (Cited on page 60.)

[81] M. Simon and M. Alouini, *Digital Communication over Fading Channels*. Wiley Series in Telecommunications and Signal Processing, Wiley, 2005. (Cited on page 60.)

[82] D. Stoyan, W. S. Kendall, J. Mecke, and L. Ruschendorf, *Stochastic geometry and its applications*, vol. 2. Wiley New York, 1987. (Cited on page 73.)

[83] H. Inaltekin, M. Chiang, H. V. Poor, and S. B. Wicker, "On unbounded path-loss models: effects of singularity on wireless network performance," *Selected Areas in Communications, IEEE Journal on*, vol. 27, no. 7, pp. 1078–1092, 2009. (Cited on page 77.)

[84] O. Georgiou, S. Wang, M. Z. Bocus, C. P. Dettmann, and J. P. Coon, "Location, location, location: Border effects in interference limited ad hoc networks," in *13th International Symposium on Modeling and Optimization in Mobile, Ad Hoc, and Wireless Networks (WiOpt)*, pp. 568–575, IEEE, 2015. (Cited on page 81.)

[85] S. Saha, A. Sheldekar, A. Mukherjee, S. Nandi, *et al.*, "Post disaster management using delay tolerant network," in *Recent Trends in Wireless and Mobile Networks*, pp. 170–184, Springer, 2011. (Cited on page 94.)

[86] R. Hernandez-Aquino, S. A. R. Zaidi, M. Ghogho, D. McLernon, and A. Swami, "Stochastic geometric modeling and analysis of non-uniform two-tier networks: A stienens model-based approach," *IEEE Transactions on Wireless Communications*, vol. 16, no. 6, pp. 3476–3491, 2017. (Cited on pages 94 and 97.)

[87] M. Afshang and H. S. Dhillon, "Poisson cluster process based analysis of hetnets with correlated user and base station locations," *arXiv preprint arXiv:1612.07285*, 2016. (Cited on pages 96, 98, 112, and 113.)

[88] C. Saha, M. Afshang, and H. S. Dhillon, "Enriched k-tier hetnet model to enable the analysis of user-centric small cell deployments," *IEEE Transactions on Wireless Communications*, vol. 16, no. 3, pp. 1593–1608, 2017. (Cited on pages 96 and 102.)

[89] C. Saha, M. Afshang, and H. S. Dhillon, "Poisson cluster process: Bridging the gap between ppp and 3gpp hetnet models," *arXiv preprint arXiv:1702.05706*, 2017. (Cited on page 96.)

[90] M. Haenggi, "User point processes in cellular networks," *IEEE Wireless Communications Letters*, 2017. (Cited on page 96.)

[91] H. ElSawy, E. Hossain, and M. Haenggi, "Stochastic geometry for modeling, analysis, and design of multi-tier and cognitive cellular wireless networks: A survey," *IEEE Communications Surveys & Tutorials*, vol. 15, no. 3, pp. 996–1019, 2013. (Cited on page 96.)

[92] Z. Khalid and S. Durrani, "Distance distributions in regular polygons," *IEEE Transactions on Vehicular Technology*, vol. 62, no. 5, pp. 2363–2368, 2013. (Cited on page 108.)

[93] M. Ahsanullah and V. B. Nevzorov, *Order statistics: examples and exercises*. Nova Publishers, 2005. (Cited on pages 110 and 167.)

[94] Y. S. Soh, T. Q. Quek, M. Kountouris, and H. Shin, "Energy efficient heterogeneous cellular networks," *IEEE Journal on Selected Areas in Communications*, vol. 31, no. 5, pp. 840–850, 2013. (Cited on page 122.)

[95] M. M. Azari, Y. Murillo, O. Amin, F. Rosas, M.-S. Alouini, and S. Pollin, "Coverage maximization for a poisson field of drone cells," *arXiv preprint arXiv:1708.06598*, 2017. (Cited on page 125.)

[96] I. Atzeni, J. Arnau, and M. Kountouris, "Downlink cellular network analysis with los/nlos propagation and elevated base stations," *IEEE Transactions on Wireless Communications*, vol. 17, no. 1, pp. 142–156, 2018. (Cited on pages 126, 131, and 132.)

[97] J. G. Andrews, F. Baccelli, and R. K. Ganti, "A tractable approach to coverage and rate in cellular networks," *IEEE Transactions on communications*, vol. 59, no. 11, pp. 3122–3134, 2011. (Cited on pages 130 and 131.)

[98] Y. Wang, M. Haenggi, and Z. Tan, "Sir meta distribution of k-tier downlink heterogeneous cellular networks with cell range expansion," *arXiv preprint arXiv:1803.00182*, 2018. (Cited on page 130.)

[99] H. ElSawy, A. Sultan-Salem, M.-S. Alouini, and M. Z. Win, "Modeling and analysis of cellular networks using stochastic geometry: A tutorial," *IEEE Communications Surveys & Tutorials*, vol. 19, no. 1, pp. 167–203, 2017. (Cited on pages 130, 131, and 158.)

[100] S. S. Kalamkar and M. Haenggi, "The spatial outage capacity of wireless networks," *arXiv preprint arXiv:1708.05870*, 2017. (Cited on page 130.)

[101] M. Ding, P. Wang, D. López-Pérez, G. Mao, and Z. Lin, "Performance impact of los and nlos transmissions in dense cellular networks," *IEEE Transactions on Wireless Communications*, vol. 15, no. 3, pp. 2365–2380, 2016. (Cited on pages 130 and 131.)

[102] M. Haenggi, "The meta distribution of the sir in poisson bipolar and cellular networks," *IEEE Transactions on Wireless Communications*, vol. 15, no. 4, pp. 2577–2589, 2016. (Cited on pages 130, 132, 133, and 141.)

[103] M. Ding and D. L. Pérez, "Please lower small cell antenna heights in 5g," in *Global Communications Conference (GLOBECOM), 2016 IEEE*, pp. 1–6, IEEE, 2016. (Cited on pages 130 and 131.)

[104] Y. Wang, M. Haenggi, and Z. Tan, "The meta distribution of the sir for cellular networks with power control," *IEEE Transactions on Communications*, 2017. (Cited on page 130.)

[105] A. M. Hayajneh, S. A. R. Zaidi, D. C. McLernon, and M. Ghogho, "Performance analysis of uav enabled disaster recovery network: A stochastic geometric framework based on matern cluster processes," in *Third Intelligent Signal Processing Conference Proceedings (ISP 2017)*, Institution of Engineering and Technology, 2017. (Cited on page 130.)

[106] N. Deng and M. Haenggi, "A fine-grained analysis of millimeter-wave device-to-device networks," *IEEE Transactions on Communications*, vol. 65, no. 11, pp. 4940–4954, 2017. (Cited on pages 130 and 150.)

[107] M. Z. Win, P. C. Pinto, A. Giorgetti, M. Chiani, and L. A. Shepp, "Error performance of ultrawideband systems in a poisson field of narrowband interferers," in *Spread Spectrum Techniques and Applications, 2006 IEEE Ninth International Symposium on*, pp. 410–416, IEEE, 2006. (Cited on page 130.)

[108] X. Zhang and J. G. Andrews, "Downlink cellular network analysis with multi-slope path loss models," *arXiv preprint arXiv:1408.0549*, 2014. (Cited on pages 131 and 132.)

[109] S. Sun, T. S. Rappaport, S. Rangan, T. A. Thomas, A. Ghosh, I. Z. Kovacs, I. Rodriguez, O. Koymen, A. Partyka, and J. Jarvelainen, "Propagation path loss models for 5g urban micro-and macro-cellular scenarios," in *Vehicular Technology Conference (VTC Spring), 2016 IEEE 83rd*, pp. 1–6, IEEE, 2016. (Cited on page 135.)

[110] S. M. Yu and S.-L. Kim, "Downlink capacity and base station density in cellular networks," in *Modeling & Optimization in Mobile, Ad Hoc & Wireless Networks (WiOpt), 2013 11th International Symposium on*, pp. 119–124, IEEE, 2013. (Cited on page 137.)

[111] J. Gil-Pelaez, "Note on the inversion theorem," *Biometrika*, vol. 38, no. 3-4, pp. 481–482, 1951. (Cited on page 142.)

[112] R. M. Mnatsakanov and A. S. Hakobyan, "Recovery of distributions via moments," *Lecture Notes-Monograph Series*, pp. 252–265, 2009. (Cited on page 143.)

[113] "State of the iot 2018: Number of iot devices now at 7b market accelerating." https://iot-analytics.com/state-of-the-iot-updat

e-q1-q2-2018-number-of-iot-devices-now-7b/, [Online; accessed 17/03/2019]. (Cited on pages 155 and 156.)

[114] B. Clerckx, R. Zhang, R. Schober, D. W. K. Ng, D. I. Kim, and H. V. Poor, "Fundamentals of wireless information and power transfer: From rf energy harvester models to signal and system designs," *IEEE Journal on Selected Areas in Communications*, vol. 37, no. 1, pp. 4–33, 2019. (Cited on page 155.)

[115] V. Liu, A. Parks, V. Talla, S. Gollakota, D. Wetherall, and J. R. Smith, "Ambient backscatter: wireless communication out of thin air," in *ACM SIGCOMM Computer Communication Review*, vol. 43, pp. 39–50, ACM, 2013. (Cited on page 155.)

[116] A. Bletsas, P. N. Alevizos, and G. Vougioukas, "The art of signal processing in backscatter radio for μw (or less) internet of things: Intelligent signal processing and backscatter radio enabling batteryless connectivity," *IEEE Signal Processing Magazine*, vol. 35, no. 5, pp. 28–40, 2018. (Cited on pages 155 and 161.)

[117] E. Kampianakis, J. Kimionis, K. Tountas, C. Konstantopoulos, E. Koutroulis, and A. Bletsas, "Wireless environmental sensor networking with analog scatter radio and timer principles," *IEEE Sensors Journal*, vol. 14, no. 10, pp. 3365–3376, 2014. (Cited on pages 155 and 156.)

[118] C. Xu, L. Yang, and P. Zhang, "Practical backscatter communication systems for battery-free internet of things: A tutorial and survey of recent research," *IEEE Signal Processing Magazine*, vol. 35, no. 5, pp. 16–27, 2018. (Cited on page 155.)

[119] E. Kampianakis, J. Kimionis, K. Tountas, C. Konstantopoulos, E. Koutroulis, and A. Bletsas, "Backscatter sensor network for extended ranges and low cost with frequency modulators: Application on wireless humidity sensing," in *SENSORS, 2013 IEEE*, pp. 1–4, IEEE, 2013. (Cited on page 156.)

[120] S. N. Daskalakis, A. Collado, A. Georgiadis, and M. M. Tentzeris, "Backscatter morse leaf sensor for agricultural wireless sensor networks," in *2017 IEEE SENSORS*, pp. 1–3, IEEE, 2017. (Cited on page 156.)

[121] S.-N. Daskalakis, J. Kimionis, A. Collado, M. M. Tentzeris, and A. Georgiadis, "Ambient fm backscattering for smart agricultural monitoring," in *2017 IEEE MTT-S International Microwave Symposium (IMS)*, pp. 1339–1341, IEEE, 2017. (Cited on page 156.)

[122] K. Mueller and M. Muller, "Timing recovery in digital synchronous data receivers," *IEEE transactions on communications*, vol. 24, no. 5, pp. 516–531, 1976. (Cited on page 162.)

[123] Á. Baricz, "On a product of modified bessel functions," *Proceedings of the American Mathematical Society*, vol. 137, no. 1, pp. 189–193, 2009. (Cited on page 164.)